UNIVERSITY OF CALIFORNIA,
IRVINE

TeV Energy Spectra of the Crab Nebula, Mrk 421 and the Cygnus Region of the Milky Way

DISSERTATION

Submitted in partial satisfaction of the requirements
for the degree of

DOCTOR OF PHILOSOPHY

in Physics

by
Branden Thomas Allen

Dissertation Committee:
Professor Gaurang B. Yodh, Chair
Professor Steven Barwick
Professor David Kirkby

2007

The dissertation of Branden Thomas Allen is approved and is acceptable in quality and form for publication on microfilm and in digital format:

Commitee Chair

University of California, Irvine
2007

Contents

List of Figures

List of Tables

Acknowledgments

I am greatly indebted to the many people in my life who, in one way or another, have inspired me to persevere in the face of great hardship. Too numerous to name many will unfortunately remain anonymous. I want to thank the entire Milagro collaboration for their guidance, advice, and assistance in the completion of this work; In particular I am indebted to my thesis advisor, Gaurang Yodh, for his generous support over the last five years, as well as the many useful and occasionally animated conversations. Tony Shoup, with whom I have had the distinct privilege to work with on and off over the last nine years, has shown dedication to his students and the Milagro project that is nothing less than inspirational. I owe much to Dr. Barry Kogan and the late Dr. John Machen who, though their timely intervention, have allowed me to lead the normal and productive life I enjoy today. I must also thank my mother and father whose support, encouragement, and advice have proven invaluable over the years. Finally I must express my deepest gratitude to my wife, Ryoko, for her patience, understanding, generosity, and companionship.

Curriculum Vitae

Branden Thomas Allen
4129 Frederick Reines Hall
Department of Physics and Astronomy
University of California, Irvine
Irvine, CA 92697-4575

Education

2007 Ph.D. Physics	University of California, Irvine
2005 M.S. Physics	University of California, Irvine
2001 B.S. Physics	University of California, Irvine
1999-2000 UCEAP Exchange Program	Georg-August Universität, Göttingen, Germany

Professional Experience

9/2003-Present	Graduate Research Assistant Milagro	University of California, Irvine Advisor: Gaurang Yodh
9/2002-9/2003	Teaching Assistant	University of California, Irvine
7/2001-8/2002	Accelerator Systems Operator	Stanford Linear Accelerator Center
9/2000-6/2001	Undergraduate Research Assistant ATLAS Experiment	University of California, Irvine
5/1999-8/1999	Undergraduate Research Assistant D0 Experiment	University of California, Irvine
6/1998-5/1999	Undergraduate Research Assistant Milagro	University of California, Irvine

Abstract of the Dissertation

TeV Energy Spectra of the Crab Nebula, Mrk 421
and the Cygnus Region of the Milky Way
by
Branden Thomas Allen
Doctor of Philosophy in Physics
University of California, Irvine 2007
Committee Chair: Gaurang B. Yodh

The production mechanism of very high energy gamma ray emission from energetic astrophysical sources is of central importance in the study of the origin of cosmic rays and acceleration of particles to high energies. The focus of this thesis is the determination of the energy spectra of very high energy gamma rays from 1 to 100 TeV from galactic and extra-galactic sources observed by the Milagro γ-ray observatory.

The Milagro telescope is an air shower detector located at 2630 m altitude, with a 95% duty cycle and 2 steradian view of the overhead sky. During the course of its operation both steady emission from the Crab nebula and the Cygnus region of our galaxy have been observed as well as emission from the extra-galactic sources, Markarian 421 and Markarian 501.

An algorithm for the event-by-event determination of the energy of primary γ-rays based upon observed variables for each event has been developed and applied for the determination of the energy spectra of very high energy gamma rays from

the Crab plerion, the newly discovered TeV source in the Cygnus region of our galaxy, MGRO J2019+37, and the extra-galactic source, Blazar Markarian 421. In addition the spectrum of the diffuse emission from the Cygnus region has been measured. Each has been examined for possible high energy cutoffs in their energy spectra and compared with published results from Atmospheric Cherenkov Telescope experiments and theoretical expectations.

Chapter I

Detection Methods of γ-ray Astronomy

During the last century amazing advances in Astronomy have been made. Previously the only accessible regions of the EM spectrum available for study consisted of visible light, with observations at other wavelengths having only becoming possible over the last century. The discovery of radio waves in the 19th century and invention of radio transmitters and receivers in the early 20th century provided the means for the first non-optical observation of the universe. Serendipitously, at first, we began to detect radio sources of astrophysical origin resulting in the discovery of a plethora of new objects including radio galaxies and pulsars. The trend of using new technologies in order to explore other sections of the EM spectrum continues with the observation of γ-rays at TeV energies as the most recent addition to regions accessible for the observation of astrophysical phenomenon.

Though attempts to observe high energy γ-rays have been made over the past 50 years, γ-ray astronomy has only come to fruition during the last 20 years for a number of important reasons, chief among them: the relatively low flux of sources at TeV energies, the opacity of the Earth's atmosphere to energetic photons and the presence of a large background due to the presence of cosmic rays. Currently the

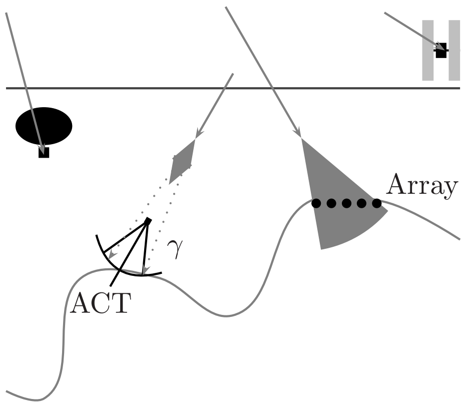

Figure I: Direct and indirect detection methods for cosmic rays and γ-rays.

methods for the detection of γ-ray sources of astrophysical origin may be divided into two categories: direct detection experiments, consisting of artificial satellites, and indirect detection methods which are ground based experiments consisting primarily of air Cherenkov telescopes (ACT's). More recently arrays of particle detectors have been developed for this purpose as well.

I Brief History of γ-ray Astronomy

Astronomy is a subject with rich historical roots. Supernova, comets and other astrophysical phenomenon were recorded by Chinese and Roman astronomers almost 2000 years ago. Known as guest stars by the ancient Chinese astronomers, the first probable recording of a supernova is found in an entry of the *Houhanshu* (there remains some controversy over a definitive identification of the source) which dates back to December 7, 185 [115]. Since then many advances have been made which have allowed us to investigate these objects in greater detail.

With the introduction of the telescope in the late 14th century a number of inventors began devoting their time to its manufacture and improvement, most notable among them was Galileo Galilei. Pointing his telescope skyward, Galileo thrust mankind into the modern age of astronomy and opened up the first band of the electromagnetic spectrum to precise astronomical study. Since those first tentative steps into the unknown, advances in technology have made observations at wavelengths both below and above that of visible light possible, greatly expanding our view of the universe.

By the late 19th and early 20th century our understanding of electromagnetic interactions began to fuel a revolution in technology and society that pervades the world to this day. The discovery of and interpretation of light as an electromagnetic wave has done much to improve our understanding of the nature of our universe and has also provided the means to search the sky in different wavelengths. The first non-optical observation of astronomical sources was preformed in 1931 by Karl Jansky. He serendipitously discovered radio emission of cosmic origin while searching for sources of interference that would effect new transatlantic communication systems operating with wavelengths of 10-20 m [107]. The quest to open new regions of the EM spectrum to precise astronomical observation had begun and has revealed many different classes objects that would otherwise be unobservable. Methods for the observation of molecular and atomic clouds of gas, the discovery of radio galaxies are but a few such innovations and discoveries that have occurred over the last 100 years. One such discovery, which made more recently in the field of radio astronomy during the 1960's, was the first observation of a pulsar with the discovery of CP 1919 by Hewish and Bell [67], a subject to which we will return later.

Around the same time access to space made possible the first direct observation of γ-rays with the launch of Explorer XI (see figure II). Though only about 20 γ-rays with energies greater than 50 MeV were detected this was but the first attempt to extend observations into the highest energy frontiers. Although γ-ray astronomy has become a separate branch of astronomy, the search for astrophysical sources of γ-rays is truly an outgrowth of an older and ongoing investigation concerning the origin of cosmic rays.

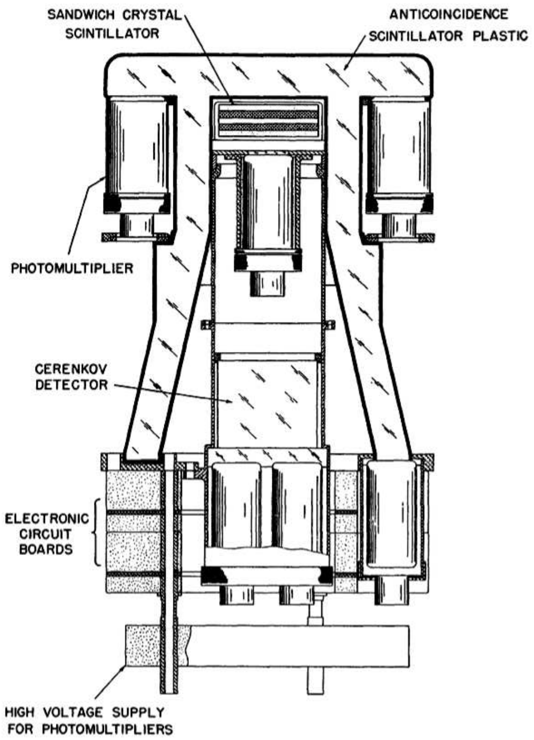

Figure II: Schematic of the γ-ray telescope aboard Explorer XI (reproduced from [77]).

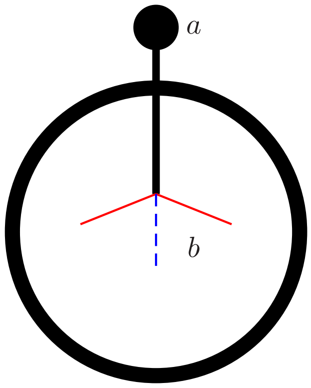

Figure III: Schematic of a gold-leaf electroscope, similar to those used by Victor Hess in his famous balloon flights. Two gold-leaf foils are electrically isolated from the outside system, with the exception of a conductor at a. When a charge is applied the conductor the collection of charge will cause the gold foils (b) to separate (shown in red). Grounding the electroscope will discharge the potential causing the foils to fall back together (shown in blue).

i Cosmic Rays

The study of cosmic rays was initiated early last century when it was observed that isolated systems (such as electroscopes shown in figure III) would gradually lose charge due the passage of ionizing radiation through the apparatus. At the time it was thought that the source of radiation originated from within the earth, though this hypothesis was soon shown to be false [89]. The breakthrough came in the summer of 1912 when Victor Hess made a series of high altitude (between 1 km and 5 km) balloon flights and determined that the rate of ionization increases exponentially with altitude, proving definitively that the source of radiation is of cosmic origin. Dubbed cosmic rays by Millikan in 1925, the search for their cause continues to this day and has given rise to many different fields of physics.

Twenty years later Carl D. Anderson began using new experimental techniques for more the precise study of cosmic rays and arguably initiated the study of particle physics with his discoveries. In place of electroscopes, useful for the measurement of ionization rates but not of the composition of cosmic rays, he employed a Wilson chamber or cloud chamber. These consist of a vessel containing a supercooled water or alcohol vapor immersed in a magnetic field. When a charged, energetic particle

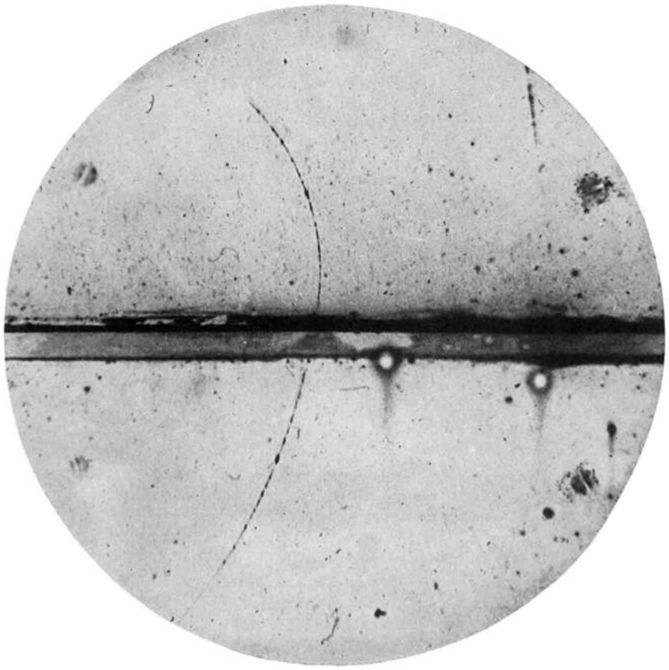

Figure IV: The first photograph of a positron detected by Carl Anderson. The Curving line is the track of a positron entering with a potential of 6.3×10^7 volt, passing through a 6 mm lead plate and emerging with a potential of 2.3×10^7 volt (reproduced from [21])

passes thorough the vessel the vapor is ionized along the particle's path causing the vapor to condense, leaving a clear signature of the particle's passage. Making a series of balloon flights and afterward examining the resulting particle trajectories a peculiar particle was observed to have the same properties of the electron with one notable difference; it possessed positive charge (e^+). Previous to this discovery it was believed that the constituents of matter were comprised entirely of negatively charged electrons and positively charged protons [89]. Originally dubbed the positive electron [21], the study of cosmic rays yielded the first of what would become a zoo of particles, and an intense field of study. Only a few years after this discovery Anderson and Seth Neddermeyer identified a component of the cosmic rays that was strongly penetrating [93], which would later be christened the muon ($\mu^{\pm}$). The discovery of these particles provided new insight into the structure and behavior of the smallest constituents of matter and launched us headlong into the study of the microcosm.

At the time the study of cosmic rays provided the only means of investigating high energy phenomenon as cyclotrons and particle accelerators had yet to be invented. Following the work of Anderson the search for high energy phenomenon though cosmic rays continued, yielding the next important advance in 1947 with the discovery of the $\pi^{\pm}$ and π^{0} [78] providing the particle theorized by Hideki Yukawa in 1937 to be responsible for nuclear interactions through the Yukawa potential given by

$$V(\phi) = \alpha^2 \frac{e^{-mr}}{r} \tag{1}$$

where α is the coupling constant and m is the mass of the particle. Though it was later realized that the $\pi^{0,\pm}$ is not responsible for these reactions Yukawa was awarded the 1948 Nobel prize in physics for "the prediction of the existence of mesons on the basis of theoretical work on nuclear forces". From this point forward particle became a field dominated by cyclotrons and particle accelerators, the two fields diverged, and search for the origin of the cosmic rays continued parallel to the investigations into particle physics.

ii The Search for the Origin of Cosmic Rays

In the course of the observation of cosmic rays many unexpected discoveries had been made by the middle of last century, however the origin of these energetic particles has yet to this day to be fully explained. The cosmic ray spectrum, as measured by various experiments, extends across the entire range of possible energies up to and possibly beyond the GZK cutoff of 10^{20} eV which should occur as result of proton interaction with the cosmic microwave background photons that permeate the universe [59].

One possible candidate that has been the subject of intense observation and speculation are supernova. Observed over the last two millennia, supernova were found to be the final act of a star's life provided its mass exceeds the Chandrasekhar

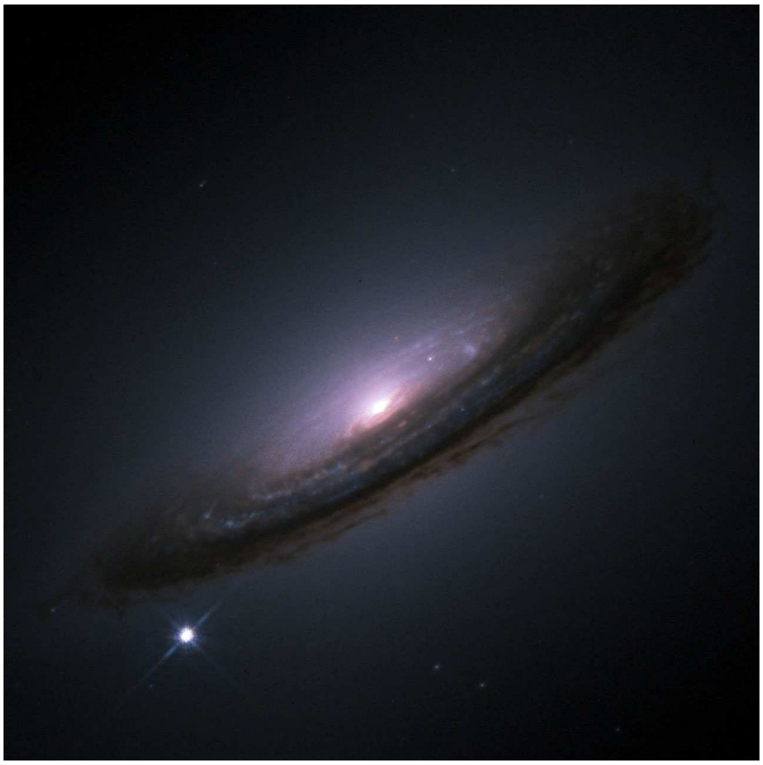

Figure V: Supernova 1994D observed in Galaxy NGC 4526 [92]

border mass, which is approximately 1.4 $M_{\odot}$. Within our galaxy it is estimated that such an event occurs about once every 20 to 50 years, the most recent of which was SN 1987a which occurred within the Large Magellanic Cloud on February 24, 1987. Once a star with a mass exceeding 1.4 $M_{\odot}$ has exhausted its fuel supply the material that was held outward by the radiation pressure due to the nuclear reactions within begins to fall inward increasing pressure on the core. This pressure eventually exceeds the pressure of the relativistic degenerate Fermi gas at the core and causes the electrons and protons of the core atoms to react via inverse β decay forming a neutron core. The equations of state for neutron matter are extremely stiff meaning that the core becomes nearly incompressible and as a result the energy of the inward falling material is reflected outward resulting in catastrophic explosion. For a brief moment the luminosity of the star exceeds that of an entire galaxy (for example see figure V), and then decays exponentially as the blast wave moves outward and the remnant begins to cool. The remnants of these violent events typically persist afterward as pulsars (rapidly rotating magnetized neutron stars) or stellar mass black holes surrounded by the material expelled in the explosion.

From 10^4 to 10^5 years after the initial explosion, material from the progenitor is expelled, potentially providing a component of the cosmic ray background. As the envelope of material expands outward into the interstellar gas a collision-less shock forms where ionized gas and plasma may be accelerated to high energies through a process known as Fermi acceleration. Recent observations of supernova remnants have also shown that such shocks persist within the inner layers of the remnant and also provide a region where particles with a sufficiently long residence time may be accelerated to ultra-relativistic energies.

The Fermi acceleration mechanism has become synonymous with the field of cosmic rays and γ-ray astronomy. It was first proposed in 1949 as a mechanism of particle acceleration in interstellar space though particle collisions with magnetic fields. A particle which collides with a magnetized cloud would undergo elastic scattering within the cloud. After a few collisions the mean velocity of the particle would match that of the cloud, and the particle would eventually escape as a newly accelerated cosmic ray [52]. This theory had the advantage that the resulting particle spectrum of the cosmic rays would obey a power law, as has been observed in cosmic ray experiments. Since then our understanding of the interstellar medium and galactic magnetic fields has improved substantially, and it has been recognized that this type of acceleration mechanism takes place within shocked regions of a plasma. Referring to figure VI an idealized case of this acceleration mechanism occurs as a particle crosses a shock boundary, elastically scatters and escapes the region. The particle may later be overtaken by the shock, scatter and return to the shock repeating this process many times, with the particle receiving a net gain of energy. Eventually the particle escapes to become part of the cosmic ray background.

There also exist sources of cosmic rays, albeit relatively small, that exist within our solar system which are produced by the same mechanism. Our sun constantly ejects material in the form of a diffuse plasma known as the solar wind. This plasma

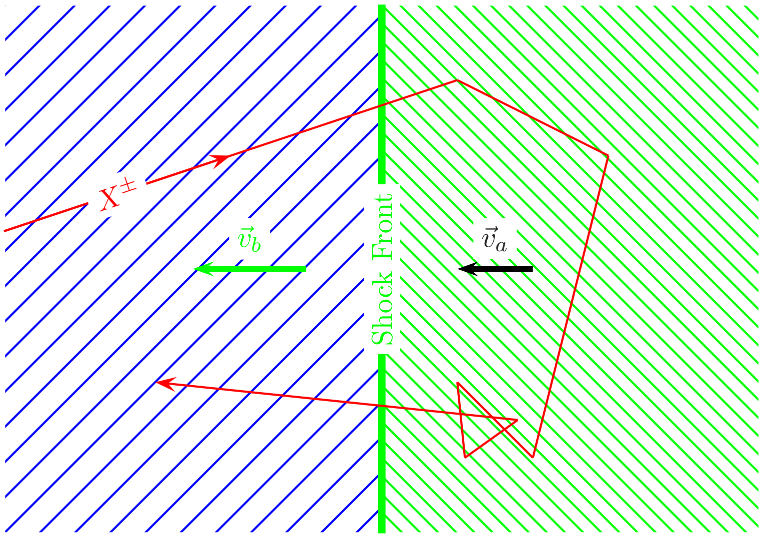

Figure VI: A schematic of Fermi Acceleration at a shock front moving with a velocity $\vec{v}_b$. $\vec{v}_a$ is the velocity of the plasma downstream of the shock front and the red line represents a charged particle incident on the shock front, which scatters and later escapes.

collides with the magnetic field of the earth and other planets and a collision-less bow shock is formed, similar to the wake which is caused by a speeding boat. At this shock the same Fermi acceleration mechanism occurs, providing a region where particles within the plasma may be accelerated. In the same way the sun is also a source of a minute fraction of the cosmic rays. As our solar system hurtles through space the magnetic field of our sun plows through the interstellar medium producing a similar bow shock. Wherever these shocks are formed, it has been found that particle acceleration takes place.

Though supernova and supernova remnants certainly are contributors to the cosmic rays observed on earth, a full description of their origin is still lacking. The primary difficulty in determining sources of the cosmic rays is the fact that cosmic rays do not point back to their sources due to the presence of interstellar magnetic fields. As a result, a single cosmic ray travels a random path though the galaxy until observed on the earth. In order to search for cosmic accelerators one must depend largely upon the observation of γ-ray and neutrino emissions which are immune to this problem, but intimately associated with the presence of cosmic rays.

iii γ-ray Astronomy

At the sources of cosmic ray acceleration there are a number of processes which also contribute to high energy photon and neutrino emission, such as inverse Compton (IC) scattering and proton interaction with the surrounding medium and ambient photons which, thorough a number of different channels, gives rise to neutrino and γ-ray emission. For this reason γ-ray astronomy and, some time in the near future, neutrino astronomy provide the means to search for potential cosmic ray acceleration sites. Unfortunately the study of astrophysical γ-ray sources is made extremely difficult due to the opacity of the atmosphere to high energy photons and the relatively low number of photon emitted by sources of all types at these energies.

As a result the first γ-ray experiments were space borne in order to avoid the negative effects of the atmosphere. The first experiments were launched beginning in the 1960's when access to space first became available. Additional interest in the development of space based γ-ray detectors was also fueled by the cold war. During this time concern about the environmental impact of nuclear weapons tests, which had been conducted by both superpowers during the 1950's, pressed the introduction of a treaty to partially ban such testing. This culminated with the signing of a partial test ban treaty, under which all parties agreed to end above ground, under water, and space based testing of nuclear weapons.

Under the political climate of the 1960's trust that the treaty would be honored was found in a fleet of satellites that were specifically designed to detect the prompt X-ray, γ-ray, and neutron emission of a nuclear test. Termed project Vela, this group of satellites would never observe a nuclear test but were the first to observe the most extreme of astrophysical phenomena. During the period between July 1969 and July 1972 sixteen short bursts of high energy photons, each lasting between 0.1 s and 30 s with energies between 0.2 MeV and 1.5 MeV, were observed with the Vela satellites [76]. These events are now known as γ-ray bursts (GRB).

In addition to these unintentional efforts, the first incarnation of a ground based technique for the detection of γ-rays was under development in the form of air Cerenkov telescopes (ACT). This technique relies on the search for the Cerenkov light that accompanies an extensive air shower (EAS); the result of cosmic or γ-ray's interaction with the atmosphere. Initially introduced for the study of high energy cosmic rays, the use of ACT's has seen a revolution since the first detection of the crab nebula in 1972 at the 3.1σ level [51]. This first attempt to detect γ-rays with a ground based detector was carried out between 1969 and 1972 using a single phototube of diameter 12.5 cm at the focus of a 10 m reflector. In total 12393 minutes of observing time were dedicated to the search of γ-ray emission from the crab nebula [112]. It was 17 years later, in 1989, that a definitive 9σ detection of the crab nebula at TeV energies using this technique became possible. This was due to the introduction of a 37 pixel PMT camera and a new γ-hadron separation technique based upon shower images which made possible the rejection of 98% of the background events [113].

These experiments are the earliest examples of direct detection (space based), and indirect detection (ground based) instruments which have provided the bulk of our knowledge of γ-ray astronomy in the energy range from a few MeV up to and above 100 TeV.

II Direct Measurement Techniques

Direct detection of γ-rays may only be achieved in space owing the opacity of the atmosphere to high energy photons. Since the launch of Explorer XI and the system of Vela satellites there have been a number of space based experiments launched for the study of astrophysical γ-ray sources. The advantage of these experiments lies in the fact that photon energies and particle identification are made by direct measurement, where all ground based techniques rely on observation of a particle's interaction with the atmosphere.

The first satellite launched, whose primary purpose was the detection and

Probe	Launch Date	End Date	Energy Range	Sources Detected
Explorer XI			$\sim$ 100 MeV	20 Photons
VELA	5-12-1969	6-19-1979	3 keV - 750 keV	13 GRB's
SAS-2	11-19-1972	6-8-1973	20 MeV - 1 GeV	Galactic Diffuse
COS-B	8-9-1975	4-25-1982	2 keV - 5 GeV	
EGRET	4-5-1991	4-6-2000	30 keV - 30 GeV	
GLAST	11-15-2007	?	?	$\sim 10^4$?

Table I: Summary of space-based γ-ray observatories [1]

study of γ-ray sources, was SAS-2 (small astronomy satellite 2). The primary instrument consisted of a 32-level wire spark chamber that had an effective area of approximately 540 cm^2. Located below the primary spark chamber was a second spark chamber for the purpose of energy reconstruction. In addition to this SAS-2 also was outfitted with a anti-coincidence scintillator counter in order to reject background. This basic design, with improvements and upgrades, would be used for future satellite based γ-ray observatories. Despite a power failure aboard the spacecraft which prematurely ended the mission, SAS-2 successfully detected the galactic plane at MeV energies, and found correlations with galactic structures observed at different wavelengths [61]. Perhaps the greatest contribution of SAS-2 was the demonstration that such experiments, given sufficient operating time, could successfully observe a wide variety of heretofore unknown sources.

This mission was followed shortly by the launch of COS-B, which fulfilled much of the promise of the lost SAS-2 mission and in addition extended the accessible energy range up to 5 GeV. COS-B was similar in design to the SAS-2 satellite; the primary instrument was composed of a 16 level spark chamber with an anti-coincidence detector and had a peak effective area of 50 cm^2 at an energy of approximately 30 MeV [2]. With this mission 25 sources in all were observed, 4 of which were identified as the Crab and Vela supernova remnants, quasar 3C 273, and ρ Orph, at energies greater than 100 MeV (see figure VIII). The remaining sources remained unidentified [108]. The difficulty in the identification of counterparts for the COS-B sources was partially due to the poor angular resolution of the

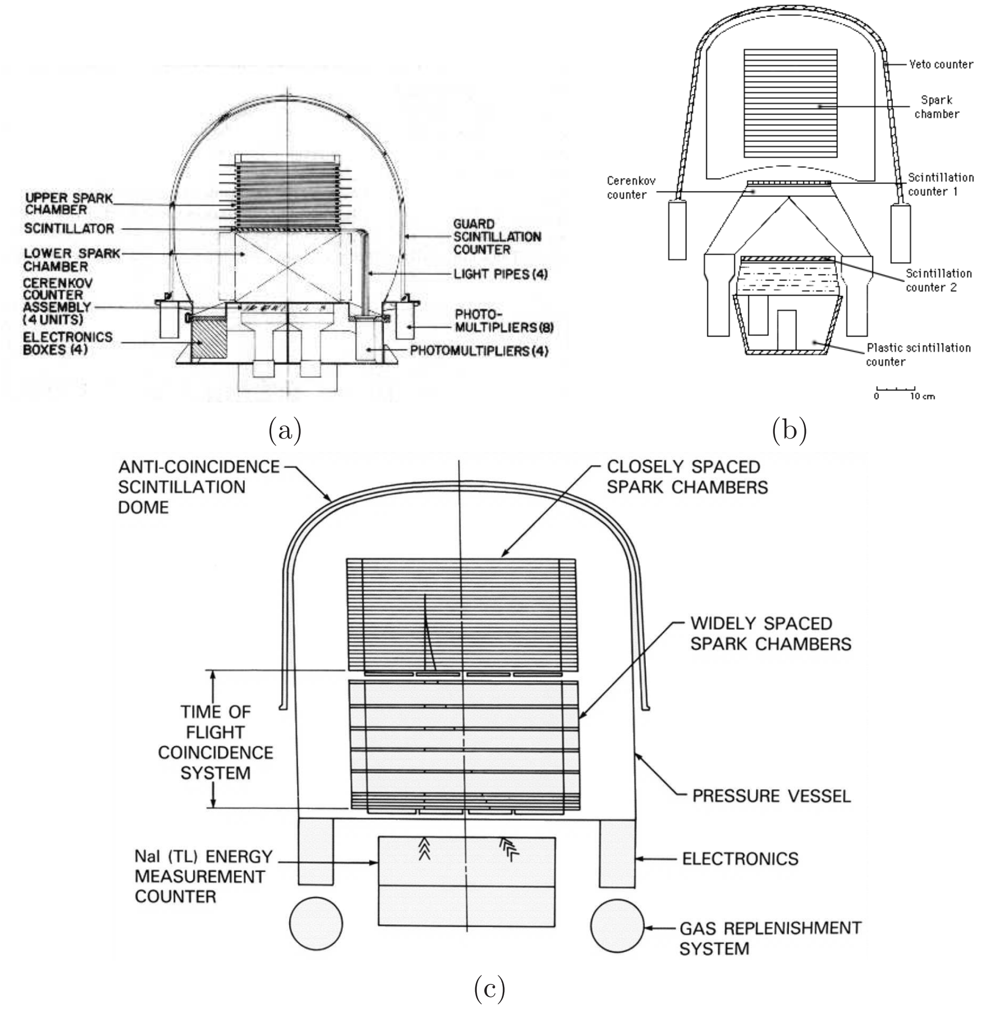

Figure VII: Schematics for (a) SAS-2, (b) COS-B [1], (c) and the EGRET [50] γ-ray telescopes.

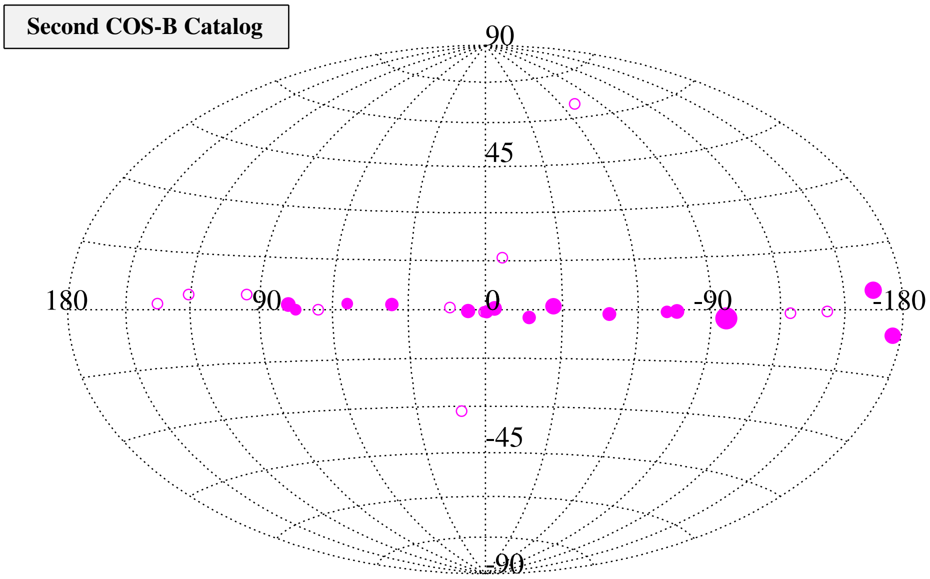

Figure VIII: Results from the 2nd COS-B catalog. The filled circles represent sources detected with measured fluxes greater than or equal to 1.3×10^{-6} cm^{-2}s^{-1}, and the open circles represent sources detected below this threshold. The size of each marker above this threshold is proportional to $\log_{10}$(flux).

instrument which had a minimum value of 1°, at high energies.

The next major mission dedicated to γ-ray astronomy was the energetic gamma ray experiment telescope (EGRET) aboard the Compton gamma ray observatory (CGRO) (see figure X), which in addition carried the burst and transient source experiment (BATSE), the Compton telescope (Comptel), and the oriented scintillation spectrometer experiment (OSSE). CGRO is to date one of the most successful missions in gamma ray astronomy and at the time of its launch was the heaviest science payload placed in orbit. The detector was greatly improved over those previously launched; with an effective area above 200 MeV of 2000 cm^2 and angular resolution between 0.1° and 0.4° as well as a field of view of approximately 40° [73] EGRET was able to detect a total of 271 sources above an energy of 100 MeV. Of these 66 have been identified with high confidence and 27 with low confidence as blazars, 5 pulsars, 1 probable radio galaxy detection (Centaurus A), the Large Magellanic Cloud, and one very bright solar flare which occurred in 1991 (see figure

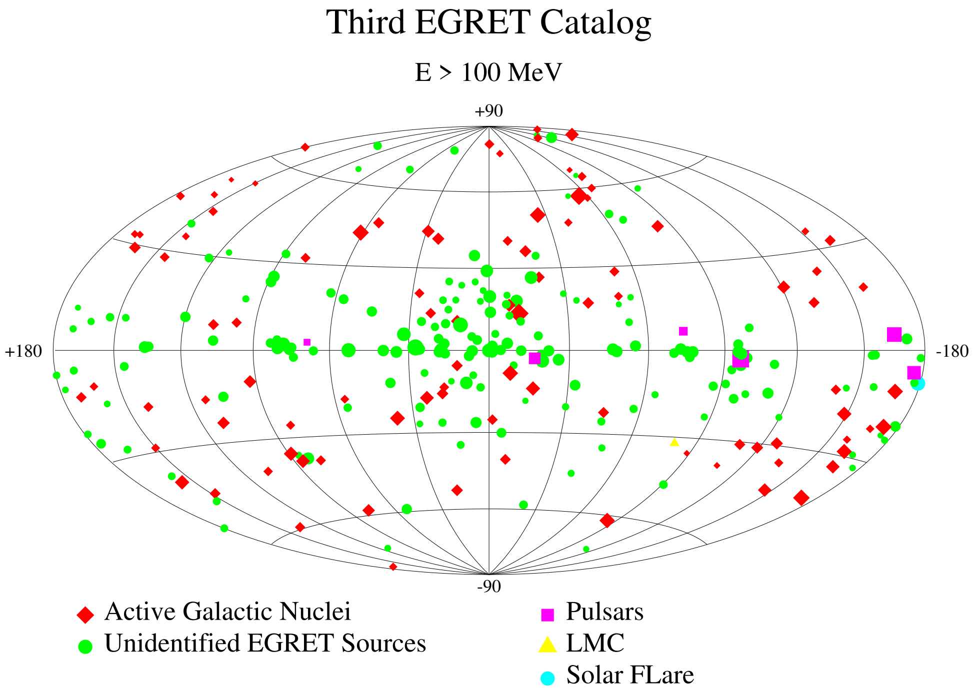

Figure IX: Results from the 3$^{\mathrm{rd}}$ EGRET catalog from [5].

IX). In addition to this the galactic diffuse emission, as well as extragalactic diffuse emission were identified [5]. The introduction of EGRET represented about an order of magnitude improvement for all detector characteristics and in the number of sources detected. The unidentified sources are those which do not have an obvious counterpart at other wavelengths, and in some circumstances may be a collection of high energy sources. Currently the nature of these unidentified sources is an active area of research, as is a full description of the nature and cause of the extragalactic γ-ray background [104]. Recently some of these sources have been tentatively associated with VHE sources recently detected in the HESS galactic plane survey [13], as well as some of the new Milagro sources, recently resolved using a new γ-hadron separation technique.

Set to launch on November 15, 2007 the gamma ray large area space telescope (GLAST) represents an improvement of at least two orders of magnitude in sensitivity over the EGRET experiment. The GLAST detector has also changed

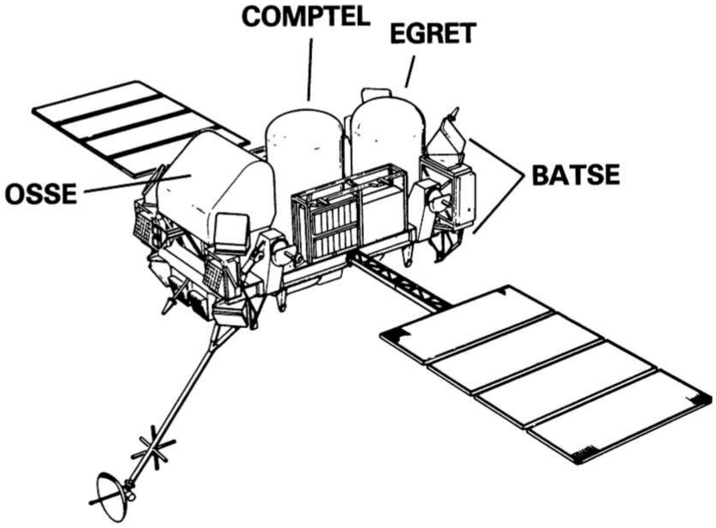

Figure X: The Compton Gamma-Ray Observatory (CGRO) [73]

significantly compared to its predecessors. Previous missions relied upon the use of a spark chamber for the measurement of particle tracks through the detector which limited their lifetimes as the spark chambers must be recharged with gas from time to time. The new silicon tracker, which will replace the spark chamber, will improve particle tracking and remove the need to carry an additional gas supply. The Large Array Telescope (LAT) is composed of a number of modules known as Tracker/Converters (TKR) which are divided into layers of a converter material and 18 single sided silicon-strip detectors. Each detector has a total of 9×10^5 channels and the total thickness of the tracker is equivalent to 1.5 radiation lengths. The Calorimeter (CAL) is composed of CsI(TI) bars arranged below the TKR towers and has an thickness equivalent to 8.4 radiation lengths. The anti-coincidence detector (ACD) is very similar to those of previous experiments, and is composed of an array of plastic scintillator tiles which surround the entire apparatus. With these advances GLAST will have an angular resolution of $0.15°$ above 10 GeV as well as an effective area greater than 8000 cm^2 and a field of view of approximately 2 steradian. With these advances in detector hardware and design GLAST is expected to operate with 40 times the sensitivity of the EGRET experiment [88].

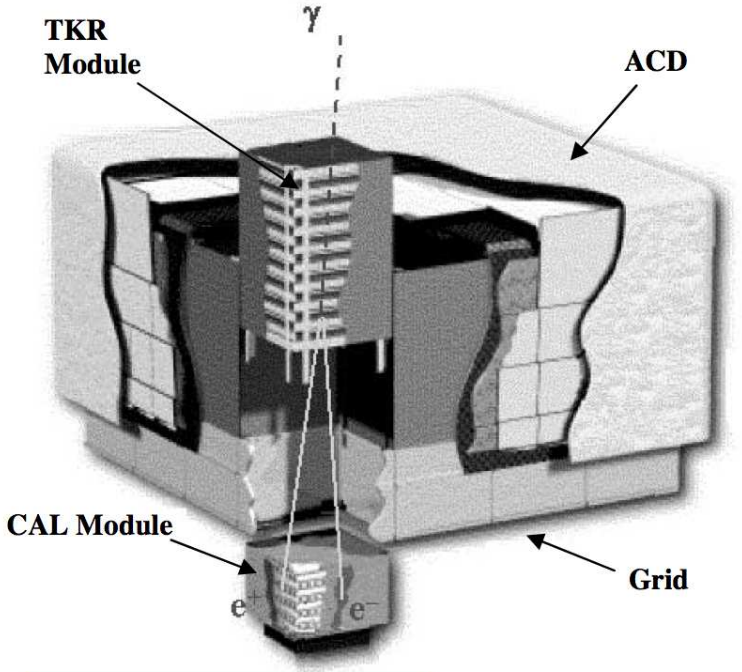

Figure XI: Schematic of GLAST. A single TKR module for the measurement of particle tracks is shown with a single γ-ray entering from above. Below the CAL modules, used for energy determination of the incident γ-ray's energy is also shown. The entire apparatus is surrounded by an anti-coincidence shield. [88]

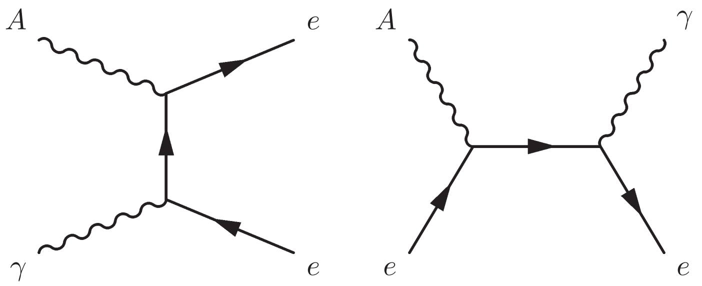

Figure XII: Principle particle interaction in a γ-ray induced EAS. Pair production and bremsstrahlung process occur when interacting with the nuclear EM field (here symbolized as A) of the atmospheric nuclei.

Though these techniques have a great advantage in γ-hadron separation though direct particle identification, the effective areas of such detectors are limited by their physical size and ultimately by the payload limits of available launch vehicles necessary for the insertion of a detector into orbit. For the study of γ-ray sources at energies in excess of 1 TeV, ground based methods which are free from this limitation are required. However due to their reliance on the observation of extensive air showers for the detection of γ-ray sources the advantages of direct observation are lost. In spite of this these detectors have the additional advantage that they have an essentially limitless size (and effective area) provided that the land and political will are available.

III Extensive Air Showers

The field of ground based γ-ray astronomy is relatively young owing the difficulty of background rejection and reconstruction of a primary particle's characteristics after interaction with the atmosphere. The observations made by these experiments consist of observations of the properties of individual EAS's which fall within the detector's field of view. As a result a detailed understanding of the behavior of an EAS is necessary in order to accurately interpret the data from any of the ground-based γ-ray observatories. For the purposes of γ-ray astronomy EAS's are generally separated into two categories electromagnetic EAS's, which are initiated by a γ-ray primary, and hadronic EAS's which are initiated by a cosmic ray proton or heavy nucleus. Knowledge of the properties of these showers are essential for the correct reconstruction of the primary event, and in particular the discrimination between γ-ray and cosmic ray induced showers. This is a primary objective for any ground based γ-ray observatory.

i Brief Introduction to Extensive Air Showers and their Observation

During the 1940's and 1950's the determination of the properties of air showers was an active area of research. During this time Heitler introduced a simplified "toy" model of an air shower which gives a qualitative overview of the properties of an air shower. If one assumes that a γ-ray will undergo pair production at exactly one radiation length (λ), and that the electron or positron will produce a γ-ray though bremsstrahlung. The total number of particles is then given by the number of splitting that have occurred which is,

$$n(x) = 2^{\frac{x}{\lambda}} \tag{2}$$

where x is the atmospheric depth traversed. This leads to a simple relation for the energy per particle $\epsilon(x) = 2^{-\frac{x}{\lambda}} E_0$ as a function of atmospheric depth. If we assume that there exists a critical energy (E_c) at which these processes will no longer take place and the shower particles will simply be absorbed into the atmosphere, we find that the maximum number of particles and maximum depth that a shower with an initial total energy E_0 will penetrate is simply given by,

$$n(x_{max}) = \frac{E_0}{E_c} \rightarrow x_{max} = \frac{\lambda \ln\left(\frac{E_c}{E_0}\right)}{\ln(2)} \tag{3}$$

[65] The important characteristics that are illustrated in this toy model, are that the number of particles in the air shower increase until a maximum depth is reached, and that the energy per particle decays approximately exponentially, while the number of particles increase approximately exponentially as a function of the radiation lengths traversed. This model may also be applied to hadronic showers by using the corresponding interaction length for hadrons.

In addition to the high energy interactions described in this simple model as well as the more complex models developed for a full description of the shower properties these particle showers (see for example [99]) there exists an additional low energy component that arises as a result of passage of the charged cascade particles through the atmosphere: Cherenkov radiation. It is well known that a charged particle traveling in excess of the speed of light in a medium will induce a coherent ionization of the medium which ultimately results in the release of a cone of radiation. A good analogy is the effect of a speeding boat upon the surface of a lake which leaves behind a wake; in this case however the wake manifests itself in the form of light. Take for example the case of a single γ-ray entering the atmosphere which interacts via pair production giving rise to a relativistic electron and positron. The pair travel through the atmosphere emitting Cherenkov photons and producing additional energetic photons via bremsstrahlung which give rise to additional electron-positron pairs. As the particle population grows (approximately exponentially) so does the Cherenkov light pool which may be observed on the ground and used to track the progress of the shower. Eventually the shower maximum is reached and individual particles begin reaching the critical energy for bremsstrahlung and pair production as the energy per particle decreases with each successive generation. Eventually HE interactions cease entirely as does the production of Cherenkov photons and the remaining shower particles are absorbed into the atmosphere.

Cosmic ray induced air showers behave in a similar fashion except additional interactions are available to them. For instance often a hadron will interact producing a pion, which upon its decay initiates its own sub shower. In general this changes the distribution of particles and Cherenkov light allowing for the discrimination of background cosmic ray events from true γ-ray events. This realization, which will be briefly covered later in this chapter, lead to a revolution in ground based γ-ray astronomy.

ii Numerical Simulations of Extensive Air Showers

In order to fully characterize the properties of EAS's the use of Monte Carlo simulations becomes necessary. This is also true for the full characterization of any ground based γ-ray observatory or cosmic ray experiment. Currently there are a number of software packages that have been developed for this purpose. Here the focus will be the CORSIKA (Cosmic Ray Simulations for Kascade) package which is in use for the simulation of many of the IACT's, Milagro, and a number of other arrays which are used for the study of high energy cosmic rays.

The CORSIKA package recognizes and simulates 50 elementary particles, and may also be used to simulate nuclei with atomic weights up to $A = 56$. The atmospheric model consists of 78.1% N_2, 21.0% O_2, and 0.9% Ar ignoring other trace gases present in the Earth's atmosphere. A primary particle is modeled entering the atmosphere and is propagated through time steps of length δt. During this time interval the probabilities of interaction, scattering, and decay are taken from a variety of analytical formulae and experimental data, and tested using the RANMAR random number generator. In this way a single shower is propagated to the ground in steps, using the results of the previous step to compute the next [64]. From this many EAS's may be simulated and detector response tested in relation to various parameters such as primary particle energy and primary particle identification. Provided as an illustration of the simulation technique and the different characteristics of extensive air showers initiated by different primary particles, four example Corsika simulations for a single γ-ray, proton, helium, and iron primary are presented in figure XIII.

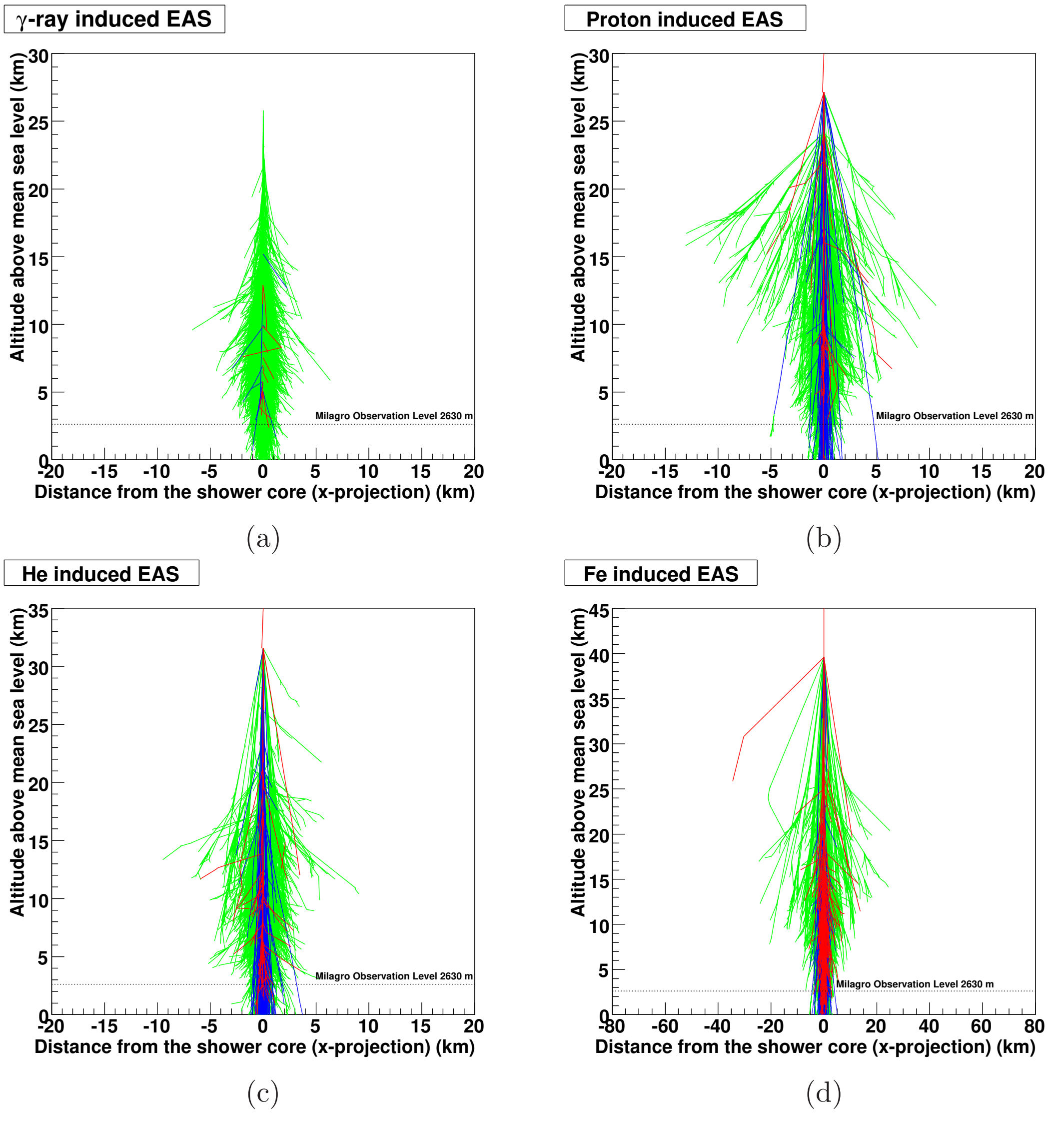

Figure XIII: A EAS simulated using the CORSIKA package for a 3 TeV primary (a) γ-ray, (b) proton, (c) helium, and (d) iron cosmic ray. The green lines represent the tracks of the electromagnetic components of the air shower, the blue are $\mu^{\pm}$ tracks, and the red are hadron tracks.

IV Imaging Air Cherenkov Telescopes

As expressed previously for the study of γ-rays at energies above 1 TeV it is necessary to use ground based detectors, due to the limited effective area of space based detectors. For a ground based IACT the detection of a particle is dependent upon interaction with the Earth's atmosphere, which results in a Cherenkov air shower. At energies above 100 GeV the extent of a particle shower can be on the order of kilometers, which translates into a large effective area for ground based detectors in general. For the new generation of IACT's such as HEGRA and HESS the effective area ranges from 30 m^2 up to 100000 m^2 depending upon the energy of the incident particle.

Air Cherenkov telescopes were introduced in their current form in 1986 with the successful introduction of the multi-pixel PMT camera by the Whipple collaboration, which made possible a new form of background rejection. More recently these telescopes have been combined into arrays of 4 or more IACT's which work in concert to identify and study TeV sources and represent the most well known and successful experiments in TeV γ-ray astronomy to date.

A single IACT consists of two basic parts: The first is a large segmented reflector and the second is a multi-pixel camera composed of single PMT pixels. As described earlier the charged particles of an EAS will emit Cherenkov light as it propagates through the atmosphere, which may be detected using photomultiplier tubes. The reflector of the IACT is designed to reflect Cherenkov light toward the camera, so that an "image" of the light distribution may be recorded and from this the characteristics of the EAS and the primary particle may be reconstructed. The original multi-pixel camera contained a total of 37 pixels [113], while the most recent cameras in use for Veritas telescopes have a total of 499 pixels [70]. The HESS cameras contain a total of 960 pixels [9].

It is only relatively recently the ACT's have successfully observed high energy γ-ray sources. After nearly 30 years of operation without a significant source de-

Experiment	Operation Dates	Description	Sources Detected
Whipple	1987 → Present	10 m reflector, 37 Pixel Camera [113]	Crab Nebula [113], Mrk 421 [97]
Veritas	2004 → Present	4 IACT's, 15 m reflector, 350 pixel camera	Crab Nebula [70], (Under Construction)
Cangaroo-I [91]	1992 → 1999	1 IACT's with 3.8 m reflectors and 256 pixel camera	Crab Nebula, Mrk 421, RXJ 0852.0-4622, SN 1006, PSR 1706-44, Galactic Plane, PKS 2155-304, Cen A [94]
Cangaroo-II [91]	1999 → 2004	Cangaroo-I + 1 IACT 7 m reflector 512 pixel camera	
Cangaroo-III [91]	2004 → Present	4 IACT's with 10 m reflectors and 552 pixel cameras	
HEGRA [42]	1992 → 2004	5 IACT's with 8.5 m^2 reflectors	Crab Nebula, Mrk 421, Mrk 501
HESS	2001 → Present	4 IACT's with 12 m reflectors and 960 pixel cameras [9]	35 Sources [3]: pulsar wind nebula, AGN's, galactic center, galactic center diffuse [12], and microquasars (see figure XV).
Magic [81]	2001 → Present	17 m reflector	20 extragalactic [49]

Table II: A partial list of important IACT observatories and their accomplishments

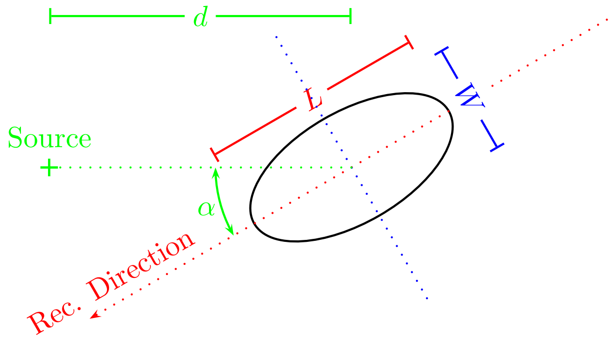

Figure XIV: A simple schematic of the Hillas parameters used for background rejection in IACT's.

tection a major advance for this technique was made with the introduction of the 5 Hillas parameters for background rejection. Through simulations of air showers, similar to the CORSIKA package briefly discussed, it was determined that a shower initiated by a primary γ-ray will leave an image that fits well to an ellipse. It was also found that showers initiated by a primary cosmic ray produce an image that differs from this substantially due to the creation of sub showers initiated by the $\pi^{0,\pm}$'s of hadronic showers which deposit light outside outside of the ellipse formed by the main shower. The parameters are defined as the RMS spread of Cherenkov light in the direction parallel to the major and semi-major axis of the ellipse (labeled L and W in figure XIV). The additional parameters are defined by a new axis stretching between the center of the field of view (source) and the centroid of the image shown as a dotted green line in figure XIV. The distance from the source to the centroid of the image (d), the RMS width of the image along this axis and the distance of the source to the major axis of the image ($d\sin(\alpha)$) are the final three parameters [69]. Taking cuts on these parameter optimized using Monte Carlo simulations and the original 37 pixel camera available for the Whipple observatory it was found that approximately 98% of the background events could be rejected while 15% of the γ-ray signal would be preserved making possible the first definitive observation of the Crab Nebula above 1 TeV [113]. Three years later this advance also made possible

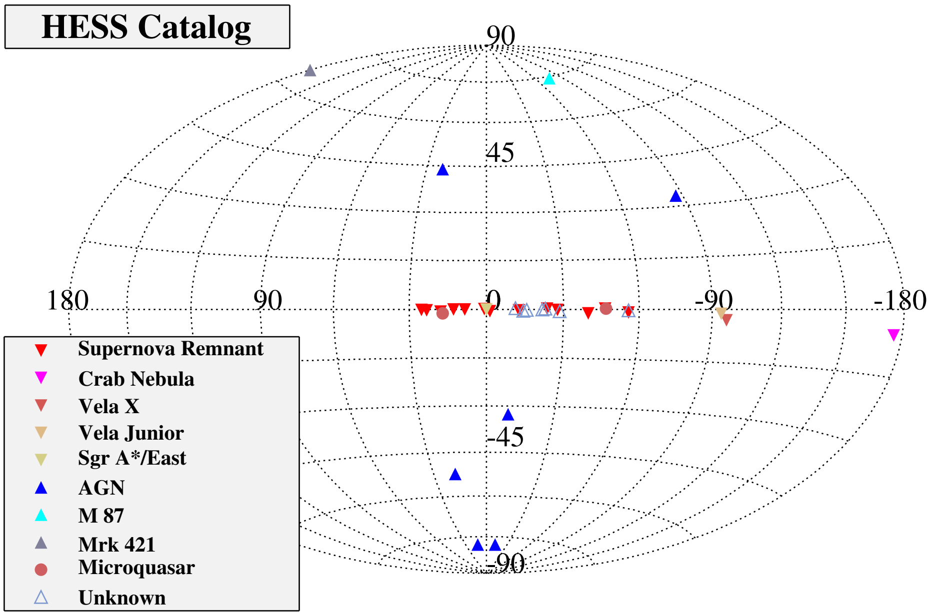

Figure XV: The HESS source catalog reconstructed from [3].

the first observation of an extragalactic TeV source (the active galactic nucleus Mrk 421) [97].

Since these early successes a number of other IACT's and IACT arrays have been built (see table II and figure XVIII) improving with each successive generation. These experiments still use the Hillas parameters for background rejection now keeping approximately 40% of the γ-ray events while eliminating more than 99% of the hadronic showers [42]. These instruments have made precision studies of galactic and extragalactic point sources at TeV energies within the last decade possible. Using an array of 4 IACT's the HESS collaboration have uncovered nearly 35 new TeV γ-ray sources of every conceivable variety (see figure XV and table II). The study of diffuse emission from the galactic plane at TeV energies with HESS has also proven possible with large exposure times, despite the limited field of view for these instruments [12].

In spite of the seemingly unbounded progress in the development of IACT's there do remain some limitations: IACT's are unable to operate during the daytime or even on nights where the moon is present. As a result the duty cycle for an

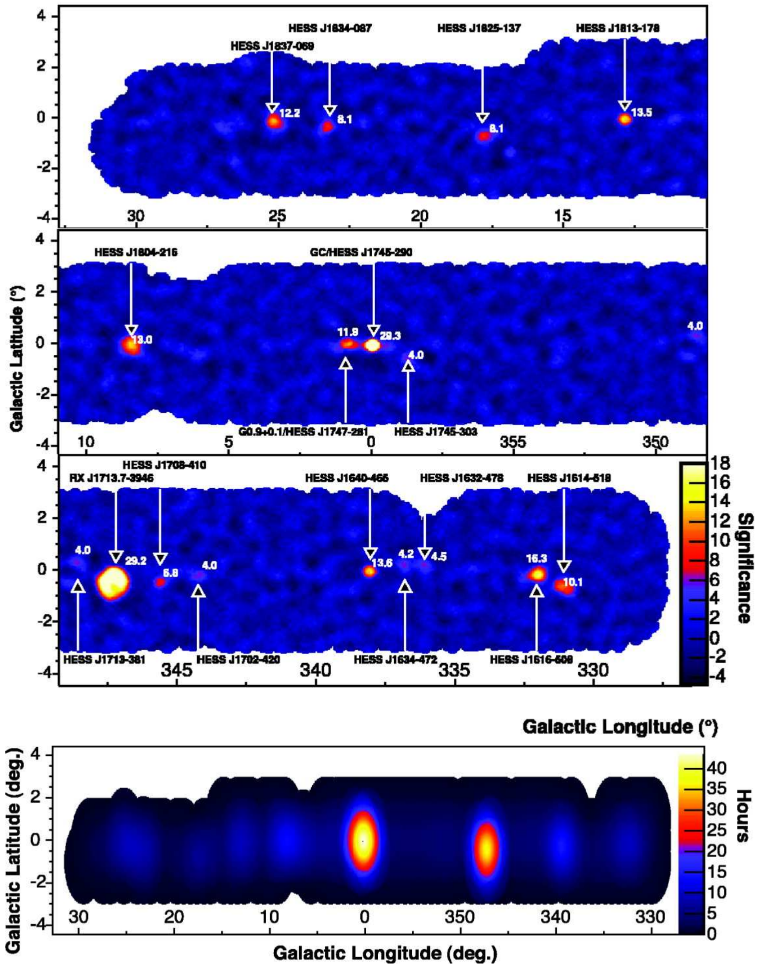

Figure XVI: The HESS galactic plane survey significance and exposure map [13].

IACT observatory is approximately 5%. An IACT's field of view is also limited to approximately 5° making these detectors ill suited for extensive sky surveys and for the monitoring of the sky for TeV transients such as GRB's. Included to illustrate this point is figure XVI from the HESS galactic plane survey [13]. The majority of the exposure time was dedicated to the study of the galactic center, while 5 to 10 hour periods were dedicated to survey the galactic plane in the vicinity of that galactic center. The small field of view also limits the ability of these instruments to detect diffuse γ-ray emission. For these types of studies there is currently an alternative type of TeV γ-ray observatory available: arrays.

V Arrays

The second option for the ground based observation of TeV γ-rays is the use of a large array of particle detectors for the direct detection of the shower particles of an extensive air shower. Arrays have significant advantages over ACT's in that they have a full view of the overhead sky and are not limited to operation during the night. Because of these advantages arrays are ideal survey instruments and all sky monitors, however the development of array-type observatories is still in its infancy. One of the most recent arrays, Milagro, has a sensitivity that is comparable to that of the 1986 version of the Whipple observatory.

The history of arrays for use as γ-ray observatories is short, and begins with the commissioning of the CYGNUS array in April of 1986 [31] which was the first ground based array constructed explicitly for the purpose of searching for 100 TeV γ-ray sources. In its first phase CYGNUS consisted of 108, and was later expanded to 200, scintillation counters dispersed over a 20000 m^2 area near Los Alamos, N.M. In addition a number of buried muon detectors were utilized in order to distinguish hadronic EAS's from γ-ray EAS's. As with the development of the IACT's the major obstacle for an array is the large background due to the presence of the cosmic rays. Though CYGNUS was unable to detect γ-ray point sources the quest to improve

Experiment	Operation Dates	Description	Sources
Tibet γAS	January 1990 [16] $\rightarrow$ Present	789 Scintillation Counters (36900 m^2) as of 2003 [4]	Crab Nebula [17], Mrk 421 [20], Mrk 501 [18]
CYGNUS [31]	April 1986 $\rightarrow$ 1996	108 $\rightarrow$ 200 Scintillation Counters (20000 m^2)	
Milagrito [24]	February 1997 $\rightarrow$ May 1998	228 PMT's (1 layer) submerged at 6 m in a pond	Mrk 501
Milagro	February 1999 $\rightarrow$ March 2002	450 PMT's submerged at 1.5 m, 273 PMT's at 6 m	Crab Nebula [26], Mrk 421 [27], Cygnus Hot Spot, Diffuse Emission from the Cygnus Region [8] and the Galactic Plane [28]
Milagro (Outrigger Array)	March 2002 $\rightarrow$ Present	Milagro + 175 "outrigger" tanks with a single PMT each	

Table III: A summary of ground based arrays for the observation of TeV γ-ray sources completed to date.

this technique proceeded.

The next, and longest running of the ground based arrays, is the Tibet γAS array located at an altitude of 4300 m at Yangbajing in Tibet. Tibet γAS has been modified substantially since it was commissioned in 1990 and has seen two major upgrades. The first incarnation of this array consisted of only 49 scintillation detectors and was unable to detect γ-ray point sources as of 1992 [16]. In 1996 the Tibet array was upgraded and renamed Tibet-II which contained a total of 185 scintillators on a 15 m grid. In addition a high density array of 109 scintillation detectors were placed within this array on a 7.5 m grid. With these additions the Tibet γAS became the first array experiment to detect the crab nebula (at the 5.5σ level) at energies above 1 TeV [17]. This upgrade also made possible the observation of the AGN Mrk 501 in a flaring state in 1997 [18]. The most recent upgrade occurred in 1999 with the expansion of the high density array bringing the total number of scintillation counters to 433 [19]. Since then an ongoing search for additional γ-ray point sources continues. Additionally the Tibet-III array as well as most array based γ-ray observatories have also been used to study cosmic rays, and preform

Figure XVII: The Tibet III array. [4]

cosmic-ray anisotropy studies [71].

The difficulty in the searching for TeV γ-ray sources using the Tibet array lies in the lack of an effective γ-hadron separation technique. For the purpose of discriminating between γ-rays and hadron induced EAS's, the concept of a water Cherenkov array was developed. In Milagro the effectiveness of this technique coupled with an appropriate γ-hadron separation variable was demonstrated with the detection of the crab nebula at the 6.4σ level in 2003 [26]. Since then improvements in Milagro reconstruction algorithms and γ-hadron separation techniques have made possible the observation of numerous sources including Mrk 421 [27], the Cygnus region hot spot (MGRO J2019+37), diffuse emission from the Cygnus region [8] and the galactic plane [28] demonstrating the potential of array based γ-ray astronomy for the survey and monitoring of the overhead sky.

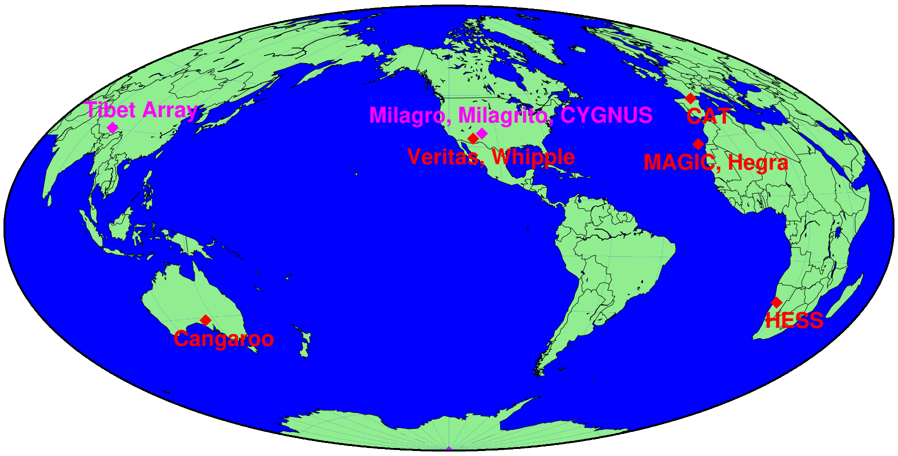

Figure XVIII: Locations of current and past ground based γ-ray observatories. The red dots represent IACT's or an array of IACT's. The purple dots represent array based observatories.

Chapter II

The Milagro γ-Ray Observatory

The Milagro detector is located at an altitude of 2630 m in the Jemez mountains, NM, USA and consists of a central 60 m $\times$ 80 m pond with an 8 m depth containing a total of 723 photomultiplier tubes submerged in purified water. The Milagro pond is surrounded by a 200 m $\times$ 200 m array of 175 outrigger tanks each containing a single inverted photomultiplier submerged in water. The pond is covered by a light-tight cover, and each outrigger is itself light-tight making the Milagro detector capable of operation twenty-four hours a day independent of atmospheric or lighting conditions. As a result Milagro has a high duty cycle (approximately 95%) and a wide field of view (approximately 2 sr) making it an ideal discovery instrument for high energy TeV sources and transients.

I Pond Layout

The detector pond is located at the center of the outrigger array and consists of two layers of 13 inch Hamamatsu photomultiplier tubes (PMT's), one submerged at a depth of 1.4 m and the other at 6.0 m. Each photomultiplier is anchored in a grid pattern spaced approximately 2.7 m apart in both the μ- and air-shower layers (see figure II). The PMT's in the pond are divided into a number of "patches", each consisting of 16 PMT's with a common power supply and a common analog channel

Figure I: Two views of the Milagro pond with approximately 10 of the closest outrigger tanks. In the photo on the left the pumping station (building to the left) and the electronics house (to the right) are visible. In the photo on the right the lightning protection system, a network of wires suspended above the pond by small telephone poles, is also visible.

for the readout of pulse data for each PMT. Each photomultiplier tube is self-contained within a PVC housing in order to protect the electronics from exposure to water and to prevent shorting out the high voltage system. Each PVC housing is outfitted with a baffle; a shield attached to the upper portion of the housing to reduce the effect of Cherenkov light reflected from other areas in the pond, and to reduce trigging as a result of muons traversing the pond horizontally. The pond water is constantly circulated through a water filtration system in order to remove particles suspended in the water, critical for the accurate measurement and reconstruction of individual EAS's. Past measurements of the pond water attenuation length for light with a wavelength of 325 nm, the peak of the Cherenkov light spectrum in Milagro, are 13.8 ± 0.6 m as of 2002 [41]. Though more recent measurements give 19.0 ± 1.0 m as of 2004 [101] and is likely is due to upgrades made to the water filtration system and the removal of some of the baffles, which as later became apparent, corroded after long duration exposure to the water. This was a major factor impacting the attenuation length of the water from 2002 up to 2005. This problem was corrected in the most recent repair, carried out in September 2005, by the replacement of all baffles with a new plastic baffle that is impervious to the corrosive effects of the

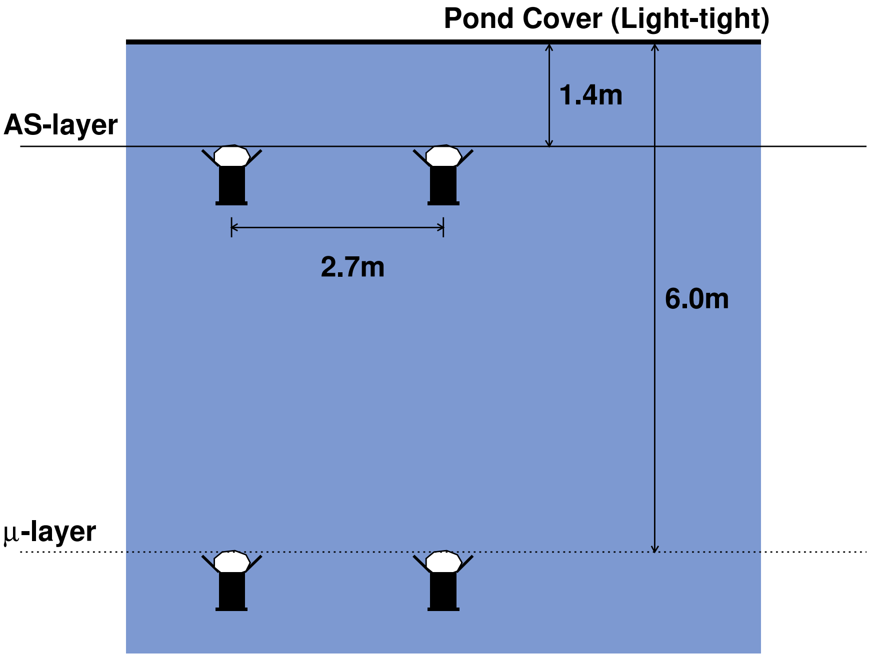

Figure II: Schematic of the Milagro pond. Each PMT (shown in white) is encased in a PVC housing (shown in black) with a baffle attached at the top of the housing extending above the top of the PMT.

water.

Due to the unusual conditions under which the PMT's in Milagro are utilized, there is a small attrition rate due to leaks in the PVC housing but primarily as a result of faulty, corroding connectors which served as the link between the PMT, the power supply and electronics system. In spite of this the rate of attrition is quite small, amounting to approximately 5 PMT's per month. In order to maintain the detector a biannual repair is carried out to restore all PMT's to working order insuring that no more than 10% of the PMT's are inoperable so as to maintain long-term detector stability. Additionally the most recent repair also saw the retirement of the faulty connectors and the adoption of a direct connection which has reduced the failure rate by 60%.

Despite the difficulties associated with maintaining a detector containing submerged PMT's the use of water has significant advantages. Due to the higher index of refraction of water the Cherenkov light production threshold is lowered to 3.7% of its value in air which leads to a substantial increase in the detectable Cherenkov light pool within the detector. The two layer design of the Milagro pond also provides a method of background rejection when searching for sources of astrophysical γ-ray emission. As can be seen from the numerical simulations presented in the previous chapter, cosmic ray induced EAS's contain a large muon component which provides a means of discrimination and background rejection. The distance from the top of the atmosphere to Milagro's altitude is equivalent to approximately 5 radiation lengths for the EM component of the EAS, depending upon atmospheric conditions, while the distance from the air shower layer of the pond to the muon layer is equal to approximately 10 radiation lengths. This has the effect of forcing a rapid evolution of the EAS within the detector causing the EAS particles to interact more frequently. Meanwhile any muons present within the EAS easily penetrate the pond and reach the bottom layer with little interaction. The muons leave a unique signature in the μ-layer of the Milagro detector upon which the X_2 hadron rejection parameter (described in detail later) is based. Here again the reduction in the

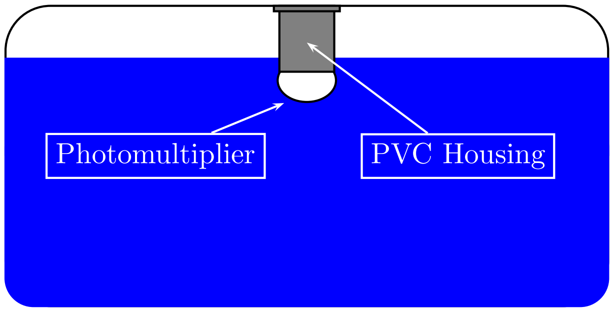

Figure III: Diagram of a single outrigger

Cherekov light production threshold is critical for the detection of low energy $\mu^{\pm}$ which would not produce Cherenkov light.

The Milagro pond provides a mechanism for the detection of $\mu^{\pm}$ which provides an effective γ-hadron method, however the limited size of the pond makes the complete characterization of an EAS difficult. For this reason the outrigger array was installed for the purpose of probing the EAS outside of the Milagro pond.

II Outrigger Array

The outrigger array consists of 173 photomultiplier tubes, each contained in separate cylindrical tanks approximately 1 m high with a 0.75 m radius. Each outrigger tank is lined with Tyvek to provide maximum reflectivity of UV photons thereby maximizing the efficiency of the individual outriggers. The outriggers are distributed unevenly about the periphery of the main pond up to a distance of approximately 200 m. As in the pond, outriggers are grouped into patches of 16 PMT's with a common HV supply and analog channel. The physical size of the pond itself is much smaller than the full extent of an EAS, which at energies in excess of 1 TeV, may produce particles kilometers distant from the shower core making the precise characterization of an EAS utilizing the Milagro pond alone difficult. In order to accurately reconstruct the core distance of a single EAS from the center of the Milagro detector for events where the core lands outside of the Milagro pond, reconstruction using the outrigger array is required. As will be discussed in greater detail in the following chapter this requirement makes the use of the outrigger array essential to the proper reconstruction of energies. The implementation of a reconstruction utilizing the outrigger array has also enabled the improvement of the angular resolution by approximately a factor of two, easing the definitive identification of detected sources.

III Electronics

The electronics systems of Milagro are responsible for the accurate collection of raw date and the reconstruction of that data for storage to disk. In order to save disk space only the reconstructed data for the entire sky, as well as a small subset of raw data for selected sources, have been retained during the operation of Milagro. These operations are therefore essential to the successful operation of the Milagro observatory. Due to the nature of the Milagro electronics and detector, data collection requires little intervention on the part of the operator and is completely automated, excluding various maintenance tasks and intervention required for unexpected equipment failures.

i Front End Electronics

Each patch in the Milagro detector is connected to its own HV supply and custom built VME front end board. The front end electronics are responsible for the readout and buffering of the data acquired from individual PMT's. These consist of HV pulses to be passed to the trigger card and, if triggering conditions are met, to the on-site computer system for reconstruction and storage. In Milagro time to digital converters (TDC's) are used in place of analogue to digital converters (ADC's) in order to minimize cost and reduce detector deadtime. A time over threshold

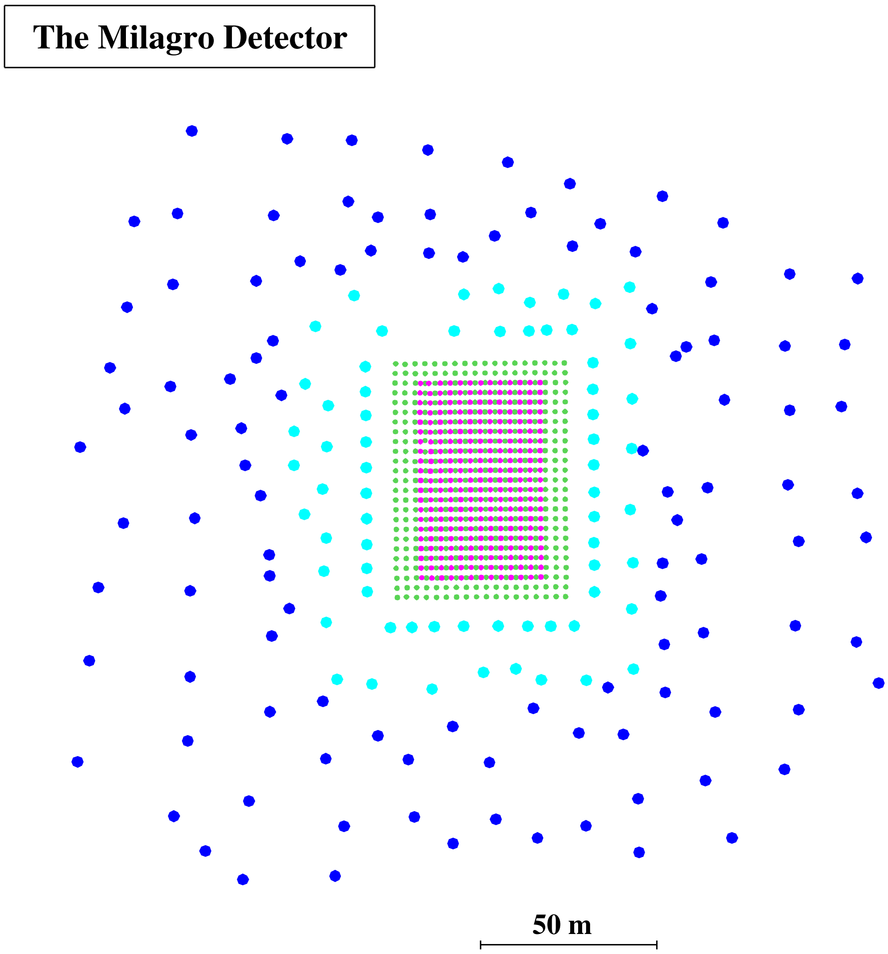

Figure IV: Diagram of the outrigger array surrounding the main Milagro pond with the inner outriggers shown in light blue and the outer outriggers are displayed in dark blue. The AS-layer PMT's are displayed in green and the μ-layer PMT's are displayed in magenta.

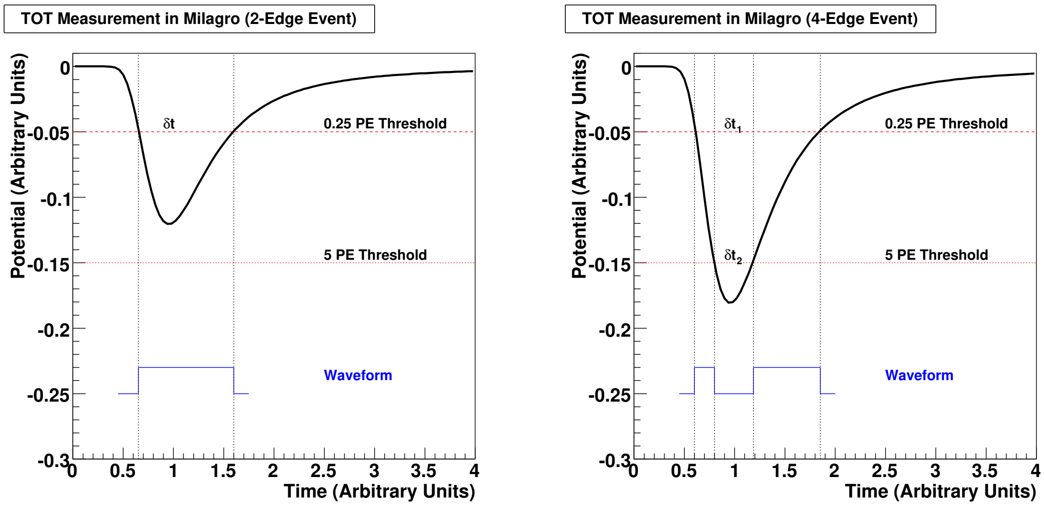

Figure V: The schematic of a 4-Edge and 2-Edge event for a single PMT in Milagro, with the waveform produced by such an event.

(TOT) method was developed in order to measure the charged displaced from each PMT without the use of ADC's. For each PMT two thresholds are set, one at approximately the 0.25 photoelectron (PE) and 5 PE level. For each PMT the time over each threshold is measured and the total number of PE's calculated from this measurement. Each crossing of the threshold generates a change in state, or an edge, which may be read by a TDC. If the event passes the triggering conditions these are then read by the Milagro computer system and sent on for reconstruction and storage. As a side note in order to correct for time offsets, mainly due to the differences in cable length, and to determine the TOT-PE relation for each PMT a laser calibration system has been installed at the Milagro site.

ii Trigger

From 2002 until its failure in late 2005 triggering for Milagro was controlled through a custom built programmable trigger card. The trigger card analyzes the analog sum from the front end boards with a time resolution of 15.5 ns, until the analog sum exceeds 120 mV, equivalent to 20 PMT's registering a photon in the air shower layer. Once this threshold is exceeded a snapshot of the analog sum, stored over 312.5 ns,

Trigger Code	Peak Voltage (mV)	Maximum Risetime (ns)	Skip Count
1	450	-	-
2	315	87.5	-
3	125	50.0	-
4	125	-	1000

Table I: Trigger conditions for the Milagro programmable trigger card (2002-2005).

is analyzed in order to determine if the trigger conditions for the risetime, defined as the time for the analog sum to rise from 12.5% up to 88.5% of its peak value, as well as the number of tubes hit in the air shower layer meet one of the trigger conditions specified in table I. In the event that the trigger condition is not met the trigger card is effectively dead for 1.5 μs, otherwise the event is recorded and the trigger card remains dead for an additional 10-20 μs [34].

Both before and after the breakdown of the Milagro trigger card, the trigger rate of the Milagro detector has remained stable between 1.7 and 1.8 kHz, with the exception of diurnal and seasonal fluctuations. Seasonal effects include the collection of snow, ice, and water on and beneath the light-tight pond cover as well as changes in atmospheric conditions, but produce no more than a 10% deviation in the overall trigger rate of the Milagro detector.

iii Online Reconstruction

Following the activation of the trigger card the raw event data is recorded temporarily to a dual ported memory module in the VME crate. The memory module is then read out by the data acquisition computer via a PCI-VME bridge that serves as a link between the detector hardware and the on-site computer network. These events are then sent to a computer known as a worker, where the events are decoded, calibrated, and reconstructed. After these tasks are completed the events are then passed back to the main data acquisition computer where they are sorted by time and stored in the appropriate files (see figure VI). These files are written to a RAID array attached to the on-site computer system, which has a capacity of 1.7 TB. There also exists an automated tape archive system, where raw data for

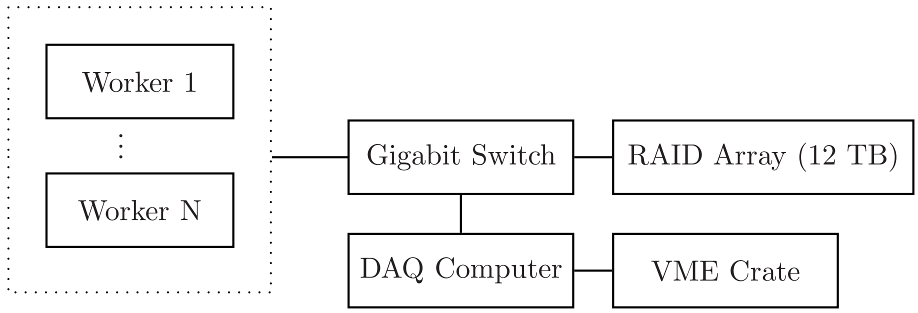

Figure VI: Schematic of the on-site Milagro computer system. [35]

various sources as well as some reconstructed data has been stored in the past. Due to the lack of available disk space the raw event data for the entire sky is typically stored for a maximum of two months before deletion. At Milagro's mean trigger rate the storage of the raw data requires approximately 250 MB of disk space per day making the retention of the complete data set prohibitively expensive.

This requirement makes the oversight and monitoring of the online reconstruction routines paramount to the successful collection and analysis of the Milagro data. These duties are carried out by a collaboration member on shift, so as to maintain the integrity of the Milagro data.

IV Event Reconstruction

Event reconstruction is carried out online and the primary analysis is preformed using this reconstructed data set. In addition there exist raw data sets which are stored permanently for three sources which have been identified by Milagro: the Crab Nebula, Mrk 421, and the Cygnus region of the Milky Way. The ultimate goal of the reconstruction process is to determine the core position, zenith angle, and the value of the various γ-hadron separation variables from the raw pulse and timing information collected for a single event. Other important quantities, notably energy, may be calculated from the reconstructed data and are therefore absent from the online reconstruction process.

i Core Reconstruction

For data taken following the installation of the outrigger array, there exist two separate methods of core reconstruction. The first of these is the outrigger center of mass core reconstruction (ORCOM). This reconstruction algorithm determines the core distance from the center of the Milagro detector through a center of "mass" calculation given by

$$r_{\mathrm{core}} = \frac{\sum_{i=1}^{N_{\mathrm{hit}}} w_i r_i N_i}{\sum_{i=1}^{N_{\mathrm{hit}}} w_i N_i} \tag{1}$$

where r_i is the position of i-th photomultiplier tube and N_i the square root of the number of photoelectrons measured in the i-th photomultiplier. Optimization of this method for detector geometry is achieved through the introduction of the weight w_i determined from Monte Carlo simulations of the detector. The predecessor of this algorithm was simply labeled COM or center of mass core reconstruction, and only utilized information from pond photomultiplier tubes for the reconstruction of the core position. Due to the different triggering efficiencies of the outrigger array and the pond photomultipliers the ORCOM algorithm chooses one layer for core determination, by first determining if the core lies on or off the pond. A good indicator of this is the ratio $N_{\mathrm{OR}}/N_{\mathrm{AS}}$ with N_{AS} as the number of photomultiplier tubes triggered in the air shower layer and N_{OR} the number of photomultiplier tubes triggered in the outrigger array, where a value greater than 0.05 indicates that a shower core has landed off of the pond. In this event the core position is computed using only outrigger photomultipliers, otherwise the core position is determined though utilization of the AS layer alone, reducing simply to the COM core determination method [46].

The second method of core determination is known as the Gaussian core fitter. Here the spatial distribution of the photoelectrons is fit to a 2-D Gaussian through a χ^2 minimization process and the center of the Gaussian taken as the fit core position of the shower. For this reconstruction method only the air shower layer and outrigger array are used, the μ-layer, as will be discussed later, is used primarily for γ-hadron rejection.

The performance of both of these methods is similar, with the ORCOM core determination algorithm yielding a median core fit error of 25 m and the Gaussian core determination algorithm yielding a median core fit error of 24 m. The original COM algorithm has comparable performance for on pond events, it is however unable to determine the position of cores for events outside of the Milagro pond [46].

After the completion of the core reconstruction the angle reconstruction algorithm may proceed.

ii Angular Reconstruction

In order to determine the origin of a γ-ray or cosmic ray primary for a single event detected with Milagro an angular reconstruction algorithm has been formulated. The extensive air shower front is approximated by a plane wave moving through the atmosphere with a propagation velocity v_0. From the timing information and location of each photomultiplier triggered for the event, the normal direction of the shower plane can be determined by defining a χ^2 function given by

$$\chi^2 = \sum_{i=1}^{N_{\rm hit}} w_i(\delta t_i^2 - |\vec{r}_i|^2) \tag{2}$$

where w_i are the weights applied to correct for the curvature of the shower plane based on the reconstructed distance from the core, $\vec{r}_i$ is the vector from the PMT with the median trigger time to the i-th triggered PMT. Minimization of this function with respect to the arrival time leads to a system of linear equations with a single known parameter $|\vec{v}_0|$ given by the velocity of light in air, giving zenith and azimuth angle fit for each event.

Since the introduction of the outrigger array in Milagro this algorithm has been used utilizing all the PMT's available in Milagro, and using only the PMT's in

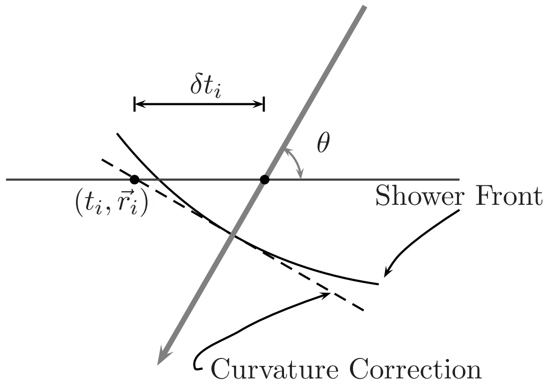

Figure VII: Schematic of the Milagro angular reconstruction algorithm.

the air shower layer with the outriggers for the determination of event directions. It was determined that the inclusion of the μ-layer PMT's for angular reconstruction neither improved nor degraded the angular resolution and have been since removed from the fit in order to improve the efficiency of the reconstruction algorithms. Using this technique the angular resolution of Milagro is approximately 0.7° (see figure VIII) with the application of quality cuts, which will be discussed in detail later.

V γ-Hadron Separation

As discussed previously the implementation of an effective γ-hadron rejection algorithm is of great importance to any ground based γ-ray observatory. Milagro implements a two layer design expressly for this purpose. The air shower layer and outrigger array are primarily utilized in order to reconstruct the event directions and core positions of EAS's while the μ-layer was built with the express purpose of searching for strongly penetrating particles present in the EAS, more specifically $\mu^{\pm}$.

As was shown using example EAS's simulated with CORSIKA, a hadronic air shower contains a substantial $\mu^{\pm}$ component which allows Milagro to discriminate

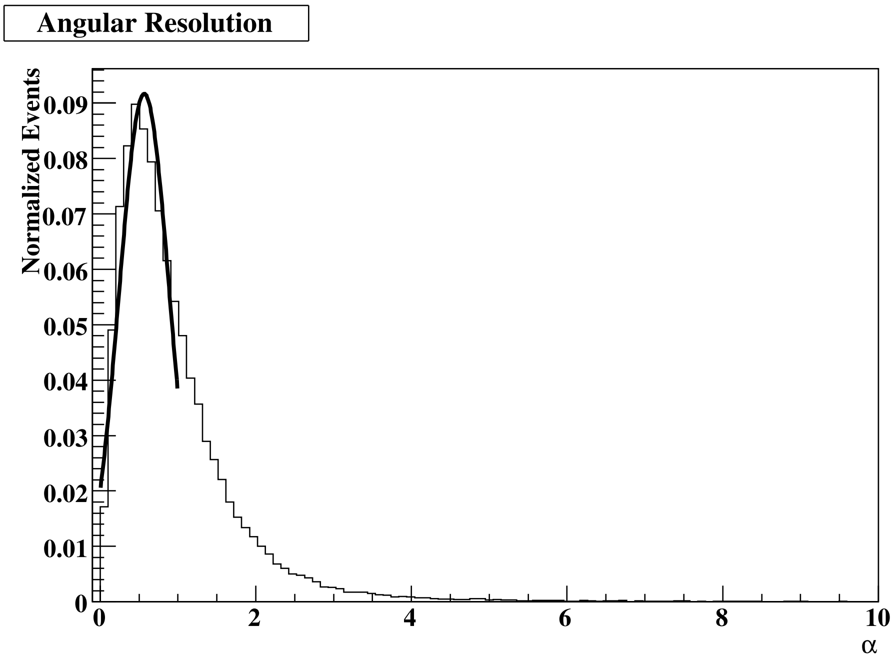

Figure VIII: The distribution of the space angle difference (α) between the reconstructed angle (ψ_{fit}) and the true angle (ψ) of γ-ray primaries for energies between 0.1 and 100 TeV, fit to a 2D-Gaussian.

between the two types of showers. Though Cherenkov light from γ-ray induced EAS's is able to trigger PMT's in the bottom layer the distribution of Cherenkov light is noticeably different from that of a $\mu^{\pm}$ which passes through the Milagro detector. As the $e^{\pm}$ and γ from an electromagnetic cascade propagate through the Milagro pond they interact many times which results in a distribution of Cherenkov light in the bottom layer that is deposited uniformly over the bottom of the pond. A $\mu^{\pm}$ on the other hand propagates through the pond with little interaction and deposits a Cherenkov light pattern that is concentrated and localized (see figure IX).

In order to exploit this observation the X_2 parameter, defined as

$$X_2 = \frac{P_{\mu,max}}{N_\mu} \tag{3}$$

where N_μ are the number of PMT's triggered for a single event in the μ-layer, and

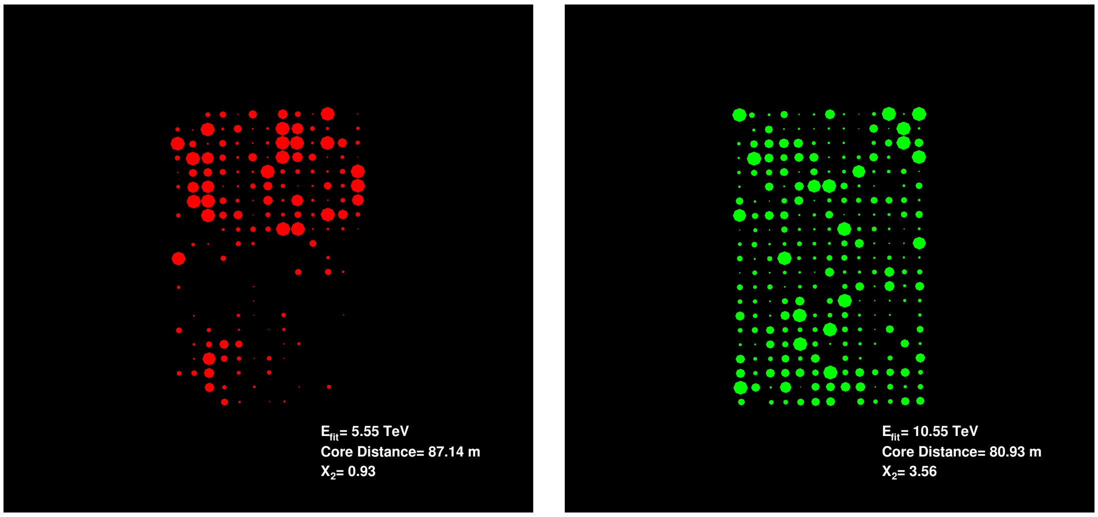

(a) (b)

Figure IX: The pulse heights recorded in the μ-layer for a single simulated (a) p^+ and (b) γ-ray event. The radius of each circle is proportional to $log_{10}(P)$ where P is the number of PE's detected by a single photomultiplier.

$P_{\mu,max}$ represents the maximum number of photoelectrons (PE's) recorded by a single PMT in the μ-layer, was introduced. For a single event where the number of PE's registered in each tube is approximately equal, X_2 approaches 0. For events where there is an uneven distribution of PE's (clumpy) the value of X_2 will increase substantially.

Using Monte Carlo simulations of the Milagro response to γ-ray and cosmic ray induced showers the effectiveness of X_2 as a γ-hadron separation parameter has been tested, and a predicted distribution of X_2 for both types of EAS's deduced. It has been found that the X_2 distribution calculated during the online reconstruction of Milagro agrees well with the distribution calculated for the cosmic ray induced EAS's. Using the predicted efficiencies of γ-ray (ϵ_γ) and cosmic ray's (ϵ_p) a quality factor, defined as

$$Q(X_2) = \frac{\epsilon_\gamma}{\sqrt{\epsilon_p}} \tag{4}$$

may be calculated as a function of the X_2 cut taken (see figure X). The optimum X_2 cut of 2.5 for a source search over the entire energy range is determined by the maximum Q-Factor with the greatest ϵ_γ.

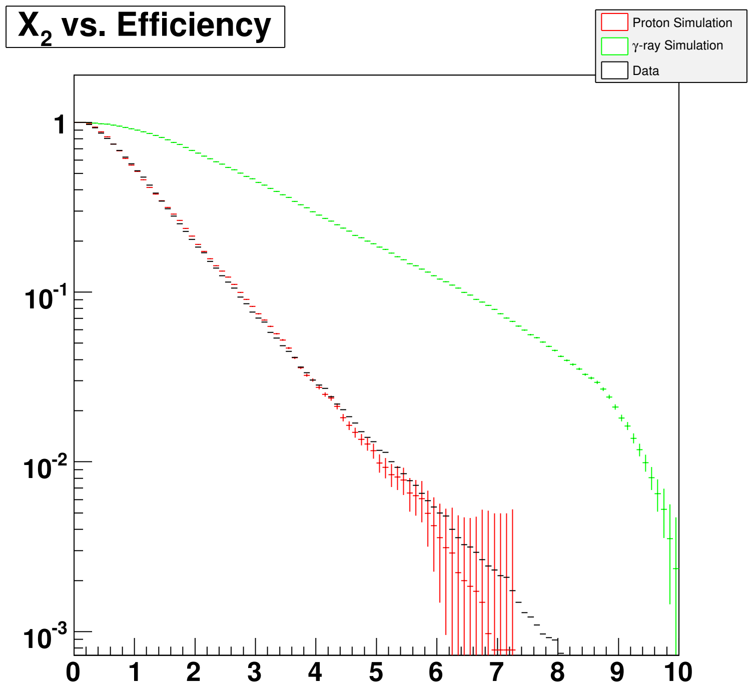

Figure X: Efficiency as a function of X_2 cut for simulated protons and γ-rays, compared to the efficiency calculated from the reconstructed data set.

The effectiveness of this γ-hadron technique was first demonstrated through observations of the Crab nebula and examination of the result before and after the application of an X_2 cut using a data set spanning the dates from June 18, 1999 until September 13, 2002. Without an X_2 cut the significance of detection for the Crab Nebula was 1.9σ, where after the application of the X_2, the background level was reduced by approximately 90% and the resulting significance of the crab detection rose to 6.4σ [26].

A new γ-hadron separation variable for Milagro has also been introduced which improves the quality factor by approximately 33% over X_2 is the A_4 variable defined as

$$A_4 = (n_{\mathrm{AS}} + n_{\mathrm{OR}}) \frac{N_{\mathrm{fit}}}{P_{\mu,\mathrm{max}}} \tag{5}$$

where n_{AS} and n_{OR} are the fraction of the PMT's triggered in the air shower layer and outriggers, N_{fit} are the number of PMT's used in the angle reconstruction and

$P_{\mu,\max}$ are the maximum number of PE's detected by a single tube in the μ-layer for a single event. For a data set spanning 1.54 years a detection of the Crab nebula at the 10.55σ level has been possible [7]. The main drawback is that this variable is strongly correlated with the energy estimation parameter making the determination of spectra while using the A_4 parameter difficult.

VI Simulation and Effective Area

One point that has been exhaustively emphasized throughout the previous chapter is that ground based γ-ray observatories are completely dependent upon the observation of EAS's. Another that has not yet been emphasized a great deal is that the determination of the detector response to these EAS's as well as the interpretation of data is completely dependent upon simulated events. This is due to the lack of a space based source of man-made γ-rays and cosmic rays with energies in excess of 1 TeV with which IACT's and array based detectors such as Milagro could otherwise be calibrated. We therefore rely entirely upon such simulations, based upon the CORSIKA and GEANT4.2 software packages, in order to reconstruct the detector's response as a function of the primary particle's energy, angle of incidence, etc. From this, quantities such as the detector's effective area as a function of zenith angle and primary particle energy, as well as energy resolution as a function of the primary particle energy may be determined.

A short summary of how the package works is as follows: a shower with a random energy, core distance from the center of the Milagro pond, and incident angle is simulated using the CORSIKA package introduced in the previous chapter. The shower's propagation through the atmosphere is simulated until reaching Milagro's altitude, where the results of the CORSIKA simulation, consisting of lists of particles and positions, are input into the GEANT detector simulation package. From this point GEANT simulates the passage of the input particles and generates a simulated detector response.

Although dependent upon the use of simulations there are ways to test their accuracy. The first verification method is the comparison of the X_2 distribution for simulated proton events with the X_2 distribution computed for the raw data. Since the cosmic ray flux is orders of magnitude greater than that of the most luminous γ-ray source the uncut raw data will be dominated by cosmic ray events. Earlier we showed that the X_2 distribution is in complete agreement with the expected distribution for the simulated data. The distributions for other detector quantities have been compared with the Monte Carlo simulation as well and found to be in good agreement with the expected distributions.

Having tested the Monte Carlo for deviations and finding none of consequence, one may proceed with the determination of the detector parameters such as the effective area of the Milagro detector for example. This may be determined through a simple Monte Carlo integration by

$$A_{\text{eff}}(E,\theta) = \pi r_T^2 \frac{N_{\text{pass}}(E,\theta)}{N_{\text{total}}(E,\theta)} \tag{6}$$

where N_{pass} and N_{total} are the total number of simulated events detected and "thrown" at a zenith angle between θ and $\theta + d\theta$ and energy between E and $E + dE$, with r_T as the maximum core distance for the simulated data set. Effective areas are on the order of 1 m for energies below 100 GeV and increase exponentially up to energies of approximately 10 TeV. Above 10 TeV the effective area remains approximately constant at 30000 m^2 (see figure XI).

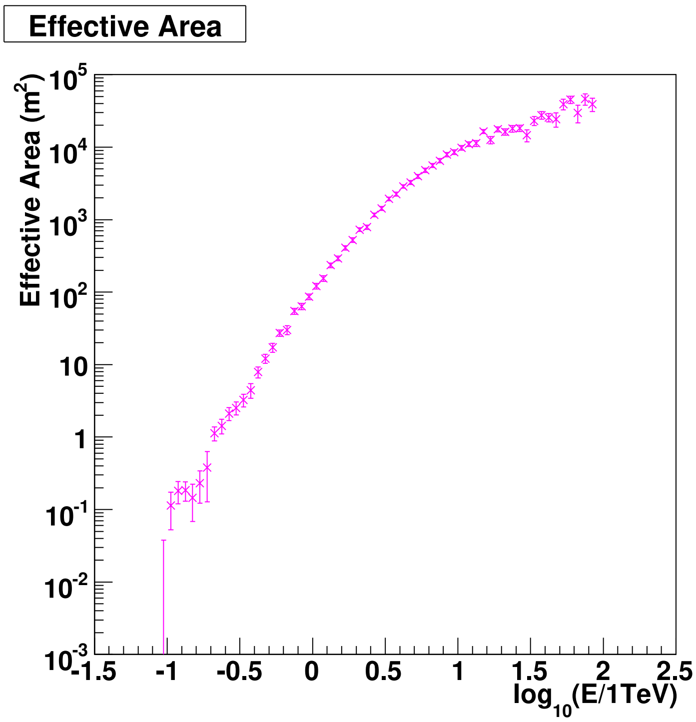

Figure XI: The Milagro effective area as a function of energy, averaged over zenith angle ($\langle A_{eff}(E) \rangle$). After standard quality cuts are taken.

Chapter III

The Search for TeV γ-ray Sources with Milagro

Milagro has seen a great deal of success as a survey instrument and has been able to definitively demonstrate the efficacy of the Water Cherenkov technique. The first successful implementation of a γ-hadron separation variable for a ground based array with the introduction of X_2 and later A_4 has enabled the detection of many of the brightest objects emitting TeV γ-rays in the northern hemisphere. Despite these advances the Milagro data set, as well as the data sets of other ground based γ-ray observatories, remain dominated by background events. This reality necessitates the implementation of a background estimation and subtraction routine which takes into account the possibility that excesses may arise though background fluctuations. The methodology of the Milagro source detection and search routines is outlined here. These routines are carried out using the reconstructed Milagro data set, and rely upon the values computed during the reconstruction process outlined in the previous chapter.

I Background Estimation and the Determination of Source Significance

The Milagro detector background estimation is carried out using the direct integration method. This method can be best visualized by considering a telescope with a small field of view; ideal for the observation of point sources. If one wishes to measure the flux from a source the telescope must track the object as the earth rotates in order to remain fixed upon one point in the celestial sphere. For the estimation of diffuse background photons due to scattering in the atmosphere and other sources, such as zodiacal light, the telescope's movement should be stopped and the number of photons outside of the source field of view counted as the celestial sphere rotates from the observers point of view. In order to preempt the possibility of contamination of the background estimate by photons originating from the source, the number of photons originating from the source direction should be excluded.

For Milagro, which has a ≈ 2 steradian view of the overhead sky, the data is sorted into square bins with a width of $0.1°$ and this process emulated. The number of "on source" events N is calculated by integrating all the events that are reconstructed within a single bin which is centered on a single point in the celestial sphere (ψ_{ij} in figure I). The number of "off source" events N_b is measured by the integration of the events which fall within a bin that does not track the movement of the celestial sphere (ψ'_{ij}). In the context of our analogy this process is equivalent to fixing separate telescopes on many different points of the sky for background estimation, and using another group of telescopes to track single sources in the celestial sphere.

A more precise description of this process is that the background located in a particular bin on the celestial sphere (ψ_{ij}) is estimated assuming an isotropic cosmic ray background by preforming a Monte Carlo integration over the following integral

$$N_b(\vartheta, \varphi) = \int \int dt' d\Omega \left\{ \epsilon(\vartheta, \varphi, t') \left. \frac{dn}{dt d\Omega} \right|_{t'} A(\theta(t'), t') \right\}, \quad (1)$$

where (ϑ, φ) are the celestial coordinates: (declination, right ascension), and (θ, ϕ) are the local (zenith angle, phi); $A(\theta, t) \simeq A(\theta)$ is the effective area of the detector as a function of the zenith angle and time. The effective area is nearly independent of time and will only change in the event of PMT failure or change in atmospheric conditions, and is thus approximately constant over the integration time ($T = 10^5$ s for this analysis). For each bin centered at $\psi_{ij} = (\vartheta_i, \varphi_j)$ there exists a corresponding local coordinate bin $\psi'_{ij} = (\theta_i, \phi_j)$, with ϕ_j as the azimuthal angle of the bin. The local coordinate bin is defined such that the positions of both bins coincide at the time $t = \frac{T}{2}$. The background estimate is obtained by counting the number of events that are detected within the local coordinate bin during the integration time. Simultaneously the number of events registered within the celestial coordinate bin are taken as the number of on source events. At the end of the integration interval the background events and source events detected for all bins visible to Milagro during the integration period are stored and the matrices ψ_{ij} and ψ'_{ij} reset. Once again ψ'_{ij} is redefined such that the positions coincide halfway through the new integration interval $\psi_{ij} = \psi'_{ij}\left(\frac{T_{new}}{2}\right)$.

The problem of contamination of the background estimate though point and diffuse sources of γ-rays is solved in the same way as described in our telescope analogy. The regions of the sky known to contain sources are stored during the computation of a background estimate. Once one of these regions enters the field of view for a single source bin ψ'_{ij} the integration of background events in this bin is halted, excluding all sources from the determination of the background. Regions currently excluded from background estimate include a $3° \times 3°$ bin around the Crab Nebula and Mrk 421, as well as the Cygnus region, where TeV diffuse emission has been detected; this area is defined in galactic coordinates as $65° \leq l \leq 85°$ and $-2° \leq e \leq 2°$.

The determination of source significance is a problem that has been revisited many times in the short history of γ-ray astronomy. As the cosmic ray flux is approximately 5 orders of magnitude greater than the flux of the most powerful

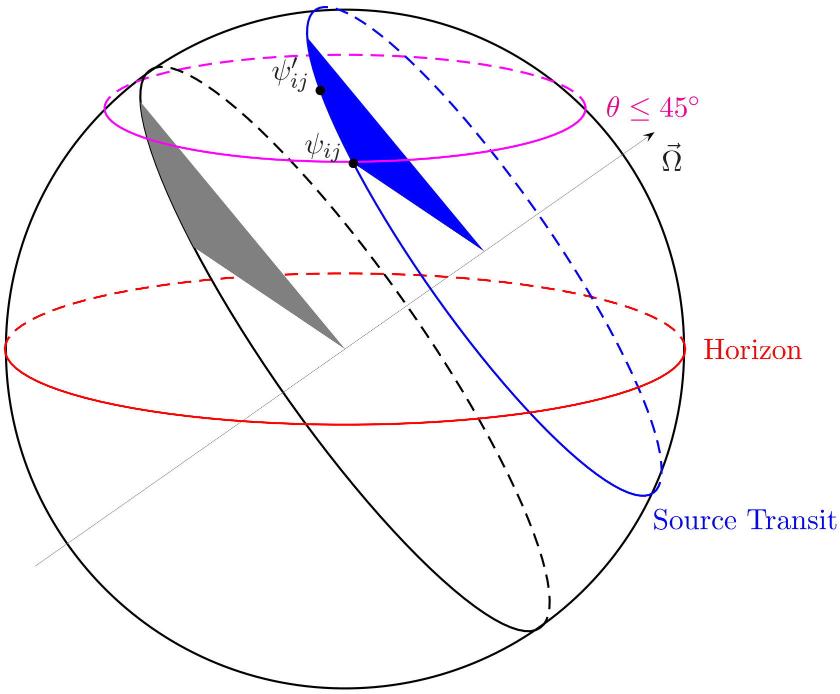

Figure I: A schematic of the celestial sphere for an observer located at a latitude of 35° N with the transit path of a single source at $\vartheta = 25°$ (given in blue). A time δt is equivalent to a total rotation angle of $\Omega\delta t$, where Ω= 1/24 hr^{-1} represented by the shaded areas for the source transit at $\vartheta = 0°$ and $\vartheta = 25°$. For the transit at 25° an integration bin ψ_{ij} and its corresponding local coordinates bin ψ'_{ij} are shown. The horizon and the zenith angle cut of $\theta \leq 45°$ imposed on Milagro data analysis is also shown.

γ-ray source, great care must be taken in order to insure that a source has truly been observed. From the 1960's up into the 1970's a great number of observed γ-ray sources had been claimed, however due to the use of incorrect statistical methods these detections were shown to be premature [39]. For a single bin the number of excess events observed are computed through

$$\widetilde{N}_b = \alpha N_b \tag{2}$$

$$\langle N_S \rangle = N - \widetilde{N}_b = N - \alpha N_b \tag{3}$$

with $\langle N_s \rangle$ as the expectation value of the number of excess events and α as the ratio of the background integration and observation times for the source. Since the measurement of N_b and N are the results of independent measurements the variance of the signal estimate (σ_s) may be determined through

$$\sigma_s = \sqrt{\sigma^2 + \sigma_b^2} = \sqrt{N^2 + \alpha^2 N_b^2} \tag{4}$$

where σ is the variance of the measured "on source" events and σ_b is the variance of the background estimate ($\langle N_b \rangle$), which reduces to equation (4). This calculation for the variance of the signal deviates from the expected significance distribution for $\alpha \neq 1$ [80]. Following the argument presented in [80] a more accurate approach is the evaluation of the detection significance using a maximum likelihood method. The null hypothesis for this computation is that all events measured in a single bin are the result of cosmic rays leaving

$$\langle N_s \rangle = 0 \tag{5}$$

$$\langle N_b \rangle = \frac{N + N_b}{t + t_b} t = \frac{\alpha(N + N_b)}{1 + \alpha} \tag{6}$$

with t as the "on" source observation time and t_b the "off" source observation time. The natural alternative to this hypothesis is simply $\langle N_s \rangle \neq 0$. Assuming that the likelihood of both hypotheses follows a Poisson distribution the likelihood ratio becomes

$$\lambda = \left\{ \frac{\alpha}{1+\alpha} \left(\frac{N+N_b}{N} \right) \right\}^{N} \left\{ \frac{1}{1+\alpha} \left(\frac{N+N_b}{N_b} \right) \right\}^{N_b} \tag{7}$$

where $-2\ln(\lambda) \sim \chi^2$ with one degree of freedom. The expression of the significance follows

$$S = \sqrt{-2\ln(\lambda)} = \sqrt{2 \left\{ N \ln \left[\frac{1+\alpha}{\alpha} \left(\frac{N}{N+N_b} \right) \right] + N \ln \left[(1+\alpha) \left(\frac{N_b}{N+N_b} \right) \right] \right\}} \tag{8}$$

and is generally referred to as "Li-Ma" after the original discoverers. In the original Milagro analysis an oversampled skymap was generated for each ψ_{ij}, where estimates of $\langle N_s \rangle$ and $\langle N_b \rangle$ would be determined through a smoothing routine, where the excess and background counts of each $0.1°$ bin would be summed in a single square bin of an optimal bin size (see section VII) greater than $0.1°$ and a corresponding significance S_{ij} computed from (8). In this way the determination of significant excesses could be made and the positions of various sources may be determined.

II Weighted Analysis

The Milagro weighted analysis is an extension of the Li-Ma method for the determination of detection significances, which was introduced as a more accurate error analysis method on the basis the signal to background ratio may be altered with the application of different cuts. In this way the maximum likelihood method may be used for the determination of source significances but in a more accurate manner. Following the arguments of [103] the main modification takes place when we consider the change in efficiency as a function of the γ-hadron separation cut. For each separate γ-hadron cut the expected efficiency for both cosmic and γ-rays is different, leading to a new estimate for the expectation value $\langle N_s \rangle$ depending upon the efficiencies within these bins giving

$$\langle N_s \rangle_i = S\epsilon_i \tag{9}$$

with ϵ_i as the efficiency for the i-th bin and S the signal strength.

For the determination of excess significance the following approximations are introduced: the likelihood for the null hypothesis and alternative are assumed obey a Gaussian on the basis that the event statistics in Milagro are sufficient to allow for an approximation of the Poisson distribution. The data are divided into independent bins based upon the γ-hadron separation cuts and the events occurring within that bin are assigned the weight ϵ_i. The likelihood for the null hypothesis, as in the Li-Ma method, reduces to a consistency test with the expected distribution of the background events, simply becoming

$$P_1 = Ae^{\sum_i \frac{(N_i - B)^2}{2B}} \tag{10}$$

where the sum is carried out over all bins with N_i the number of measured on source events and B as the number of measured background events. The second likelihood function may be determined in the same manner, however the weighted signal must now be subtracted giving

$$P_2 = Ae^{\sum_i \frac{(N_i - B - S\epsilon_i)^2}{2(B+S\epsilon_i)}} \xrightarrow{B \gg S\epsilon_i} P_2 = Ae^{\sum_i \frac{(N_i - B - S\epsilon_i)^2}{2B}} \tag{11}$$

where there exists one degree of freedom S. Assuming that the number of background events is much larger than the number of signal events we obtain the simplification in equation (11). Next we minimize $\ln(P_2)$ giving

$$S = \frac{\sum_i (n_i - B)}{\sum_i \epsilon_i^2} \tag{12}$$

which my be substituted into the likelihood ratio. After the substitution the likelihood ratio reduces to

$$\lambda = \frac{\left\{\sum_i \epsilon_i (n_i - B)\right\}^2}{B \sum_i \epsilon_i^2} \tag{13}$$

which finally gives the relation for our significance as

$$Z = \sqrt{\lambda} = \frac{\sum_i \epsilon_i (n_i - B)}{\sqrt{B \sum_i \epsilon_i^2}} \tag{14}$$

note that the only the relative weights are important as the implementation of a rescaling factor for all of the weights will leave the value of Z unchanged. The weight implemented is the signal to background ratio in each bin, as determined from the Monte Carlo simulation.

In principle this technique may be applied to any method which discriminates between cosmic ray and γ-ray events, however the weighting schemes that have proven most effective are those based on N_{fit}-X_2 bins and A_4. As will be discussed in the next chapter, the strong correlation of the energy estimation parameter with the A_4 variable makes an unbiased determination of energy spectra impossible, therefore all weight used in this analysis are based upon N_{fit}-X_2.

i N_{fit}-X_2 Weighting Procedure

The N_{fit}-X_2 weighting procedure is carried out by assigning to each event a weight that is equal to the expected signal to background ratio within discrete N_{fit}-X_2 bin as calculated from the Monte Carlo data. A schematic of the current weighting scheme is located in figure II. For each event N_{fit} and X_2 are independently determined and the event's place within the N_{fit}-X_2 space determined, at which time a weight is assigned to the event which is then added to the source and background measurements at the appropriate coordinates.

For a map containing events across the entire energy spectrum this procedure is sufficient for the improved determination of excess events originating for a par-

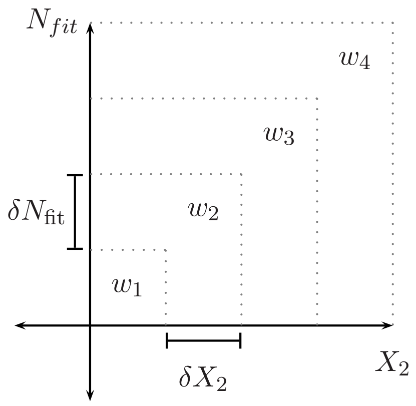

Figure II: Schematic of the discrete $N_{\rm fit}$-X_2 weighting procedure.

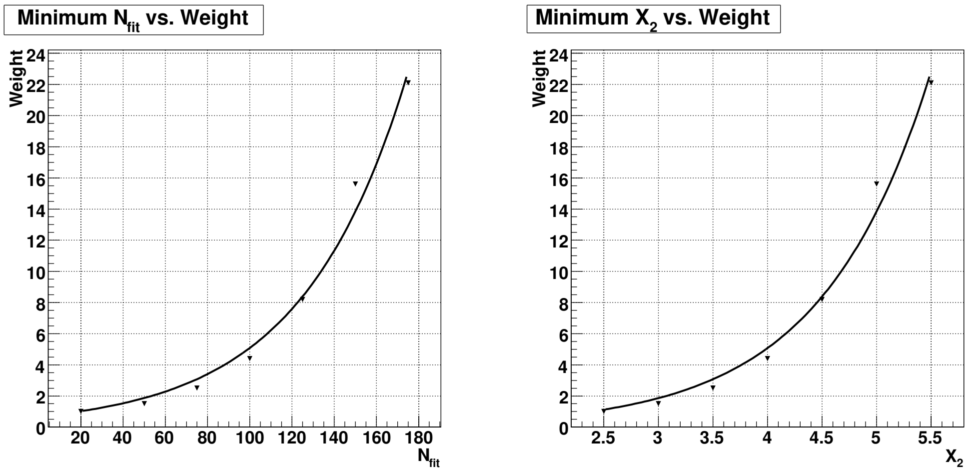

(a) (b)

Figure III: The (a) $N_{\rm fit}$ and (b) X_2 weight function used in the continuous weighting procedure. Each point is the value of the weight utilized for the assignment of discrete weights as a function of the lower X_2 and $N_{\rm fit}$ boundary.

ticular source. However, as will be described later in more detail, the optimum X_2 cut on the data increases with the fit energy. For high energy bins this reduces the number of available weights from a total of 6 at the lowest energies to a scalar map at energies fit in excess of 10 TeV. In order to correct for this a continuous weighting scheme has been implemented by letting $\delta N_{\rm fit}$ and δX_2 go to zero, replacing the discrete bins by two functions. The new weighting algorithm functions in the following manner: using the values of X_2 and $N_{\rm fit}$ determined from the reconstruction, weights are computed thorough the functions shown in figure III based only upon each parameter. The lowest weight from the two is assigned to the event which is then added to the background and source measurements in the usual way. For events which exceed the maximum weights of the original analysis a weight is assigned based upon extrapolation of the weight function.

For a test of the weighted analysis and the null hypothesis, one may look directly to the Milagro significance maps (next section). Here an oversampled sky map is produced and an excess with a corresponding significance computed. Provided that the null hypothesis is valid, the distribution of significance across the entire sky should obey a Gaussian distribution with a width of 1 after a subtraction of the known sources has been preformed. This has been shown to be true for all energy cuts in the Milagro analysis.

III Quality Cuts

For the reconstructed data analysis in Milagro a number of cuts on the data are taken in order to maximize source signals and to eliminate bad events. Proper cuts on the Milagro data may be roughly separated into two distinct categories: those designed for the resolution of a source signal, and those applied for improved reconstruction. Here the motivation and justification of the cuts are explained in detail, where optimization of the cuts for spectral analysis is described in more detail in the following chapter.

i Run Exclusion

For Milagro the data are divided into runs, which consists of a maximum of 1 day of data. These runs are further divided into a approximately 300 sub runs, approximately 5 to 6 minutes of data, which are created to enhance the portability of the data files. The majority of runs are executed without incident, there are however small subsets of the data that have become corrupted or damaged in some way and must be removed from the analysis.

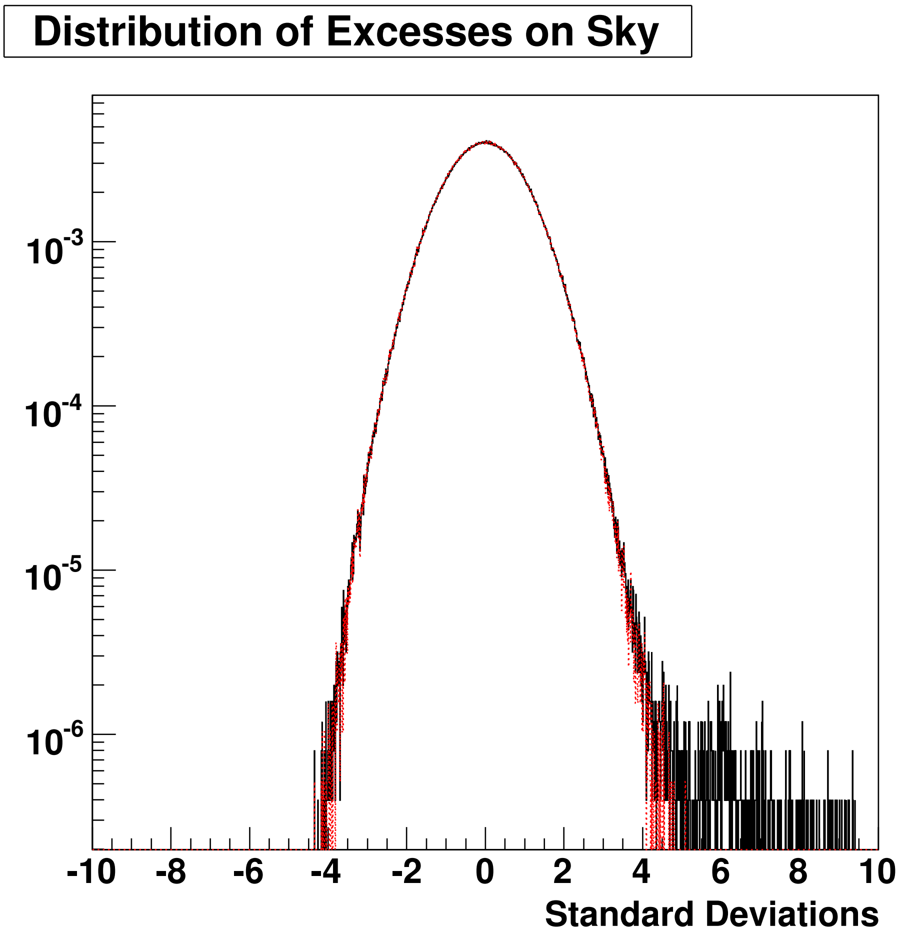

Figure IV: The significance distribution computed for all points using the $N_{\rm fit} - X_2$ weight analysis in the visible sky. In red is the significance distribution excluding the Cygnus region, Crab Nebula, and Mrk 421, which obeys a Gaussian with a width of 1.

The first subset are the data which have been taken for the testing of the various components of the detector, or the taking of calibration data. Typically this involves a change to the trigger as well as other detector components which change the detector state from that expected in the simulations. Changes in the trigger efficiency and other reconstruction parameters of the data, which are not simulated, make the accurate interpretation of these data impossible. As is such these runs are removed from the analysis.

The second subset of data are those which contain a small number of sub runs. These data become suspect, as a normal run typically contains a minimum of 100 sub runs. There exist two conditions under which a new run is initiated: the time 0 UT is reached, or the data acquisition is halted by someone, usually for the purpose of replacing hardware, repairing components or testing the detector, or automatically due to a component failure. Periods of detector instability are characterized by short runs, therefore these short runs are suspect. For caution runs containing less than 10 sub runs have been excluded from this analysis as well.

These anomalous data sets consist of less than 1% of the available data and their removal, aside from insuring that contamination of "good" events does not occur, has virtually no impact on the analysis of the data. Had the quality of these events been sufficient for inclusion in this analysis, their added presence would not effect the end result in a significant manner.

ii Outriggers

Since the conception of Milagro, the observatory itself has gone through many different changes. The original incarnation of the detector contained a single layer of 228 photomultiplier tubes submerged in the current Milagro pond. Later the pond was reconfigured to its present state without the outrigger array, and finally in 2002 the full outrigger array was completed leaving Milagro in its present state.

Due to the changes in the early versions of the detector, as well as the addition and change of the various reconstruction techniques for the determination of core positions and zenith angle, it becomes necessary to consider the effect of these changes for the proper interpretation of the data. The primary effect that this addition has had is the increase in the dynamic range of possible fit core positions by more than a factor of three. Additionally the mean core error for reconstruction algorithms utilizing the outrigger array have a mean error in core position, which is approximately 20 m, where the mean error for previous algorithms is a factor of two greater for events located on the pond. For events which are located outside of the Milagro pond, but within the outrigger array (approximately 100 m from the center of the pond) the mean core error increases slightly to $\approx$ 24 m. For reconstructions not including the outrigger array the core is placed on the pond, and the error is only bounded by the true distance of the shower core from the pond [46].

The essential differences become apparent in figure V, where the core distributions from reconstructed data using three different core reconstruction algorithms are shown. The dynamic ranges for the Gaussian and ORCOM core determination methods are clearly far superior to that of the old COM method (the circle seen surrounding the pond are directions estimated for cores determined to have occurred outside of the pond). As will be discussed in the following chapter, the accurate reconstruction of cores over a wide range is essential for the proper reconstruction of energies; the core distance must be used to scale the detector response to a single EAS. The inability to accurately determine core distances for showers at a distance greater than 30 m makes energy estimation impossible, therefore for the accurate reconstruction of spectra data not including outriggers in their core reconstruction are removed from the analysis.

This is the most severe constraint for the spectral analysis and constitutes more than half of the available Milagro data set.

iii X_2 γ-hadron Rejection Cut

Milagro's successful observation of TeV γ-ray sources has been the result of the implementation of an effective hadron rejection parameter, the first of which is the

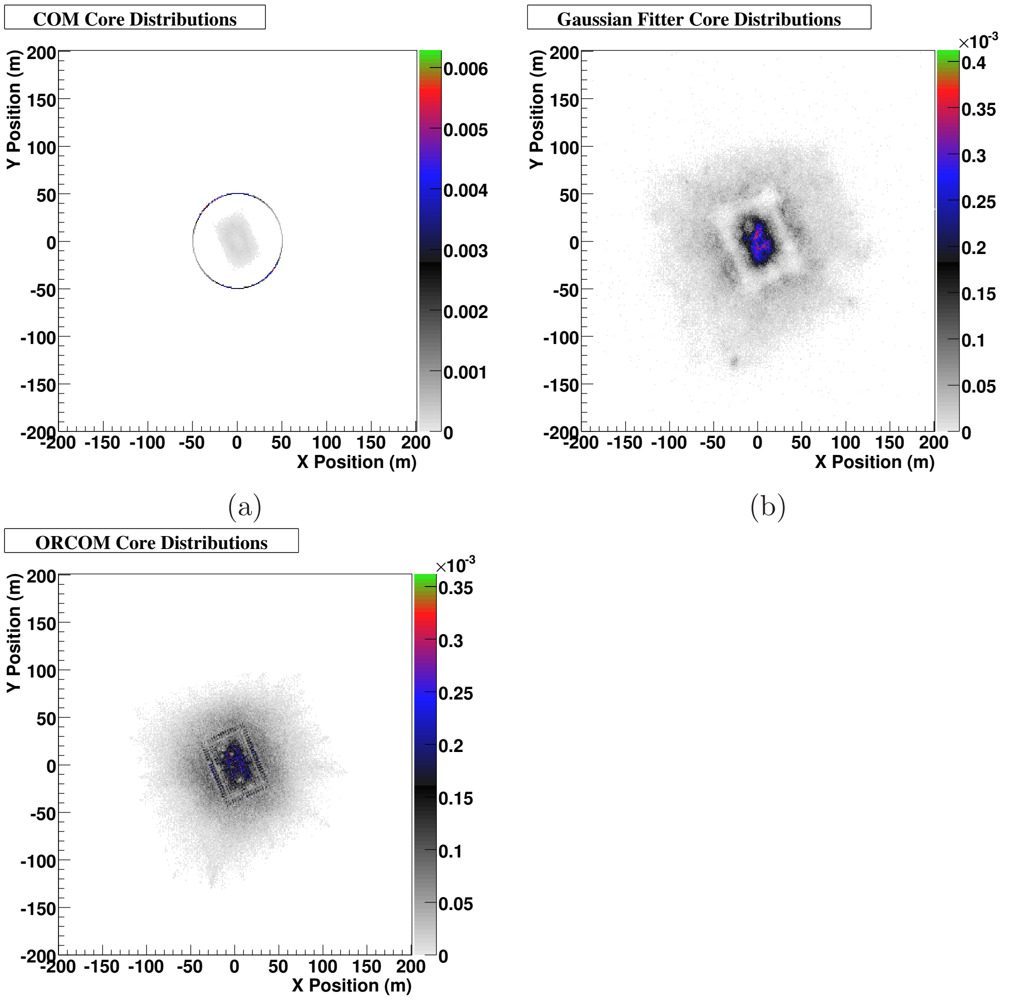

(a) (b)

(c)

Figure V: The reconstructed core distributions from two different stages in Milagro's development. (a) The center of mass (COM) fitter was utilized previous to the installation of the outrigger array, where (b) The outrigger center of mass (ORCOM) fitter and (c) Gaussian core fitter were introduced post outrigger.

X_2 parameter. The optimization of the X_2 cut is determined by searching for the cut which will maximize the detection significance of a γ-ray source. In order to estimate this the quality factor is introduced and is calculated from Monte Carlo data as a function of X_2 cut. The minimum X_2 cut at which the quality factor is reached, is taken as the optimum cut (see Chapter II). This results in the removal of approximately 99% of the cosmic ray events while preserving 40% of the γ-ray events according to Monte Carlo studies.

For the determination of energy spectra the optimum X_2 cut is determined independently for each energy bin under study. For higher energies, where the quality factor increases monotonically with X_2 there exists the further requirement that a minimum of 30% of the γ-ray events be retained for the preservation of a signal that may be present within the data. For high energies, where the event statistics are limited, this restriction becomes important to insure the measurement of a sufficient number of events, such that energy spectra may be reconstructed. The optimum X_2 cuts are then fit to a continuous function and the X_2 cut for the analysis determined from this (see figure VI). In accordance with our requirements a maximum X_2 cut of 4.2 is taken. A minimum X_2 cut of 2.5 is also implemented as a result of the automatic X_2 cut of 2.5 enforced on much of the available reconstructed data.

iv The N_{fit} Cut

N_{fit} is defined as the number of photomultiplier tubes that are utilized in the reconstruction of the angle and core distance of an extensive air shower. The more photomultipliers utilized in a fit the more accurate the reconstruction, giving improved core and angular resolution. For the accurate reconstruction of energies the $N_{\text{fit}} \geq 65$ cut is important as it significantly reduces the number of events with overestimated core distances.

This improvement is the result of an implicit timing cut which is applied once the N_{fit} cut is set. In order for a single photomultiplier tube to be included

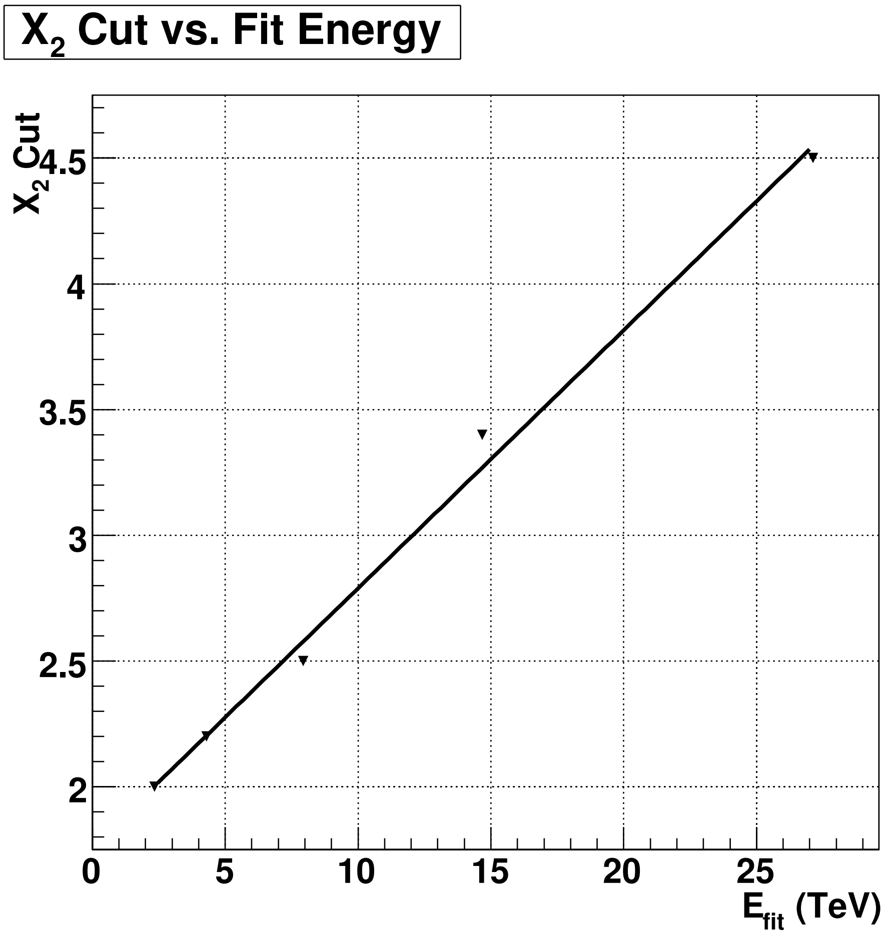

Figure VI: The $X_2(E_{\rm fit})$ function as determined from the Monte Carlo simulation. Each point represents the optimum X_2 cut in each energy bin to which the linear function $X_2(E_{\rm fit})$.

in the reconstruction of an event, the time at which the photomultiplier registers a signal must occur within a time window with a width of 10 ns. Events falling outside this window are not included in the reconstruction. The general logic of this cut is as follows: for an extensive air shower particles form an approximate plane perpendicular to the direction of the shower propagation. This breaks down at larger core distances, and as a result the width of the shower plane thickens. The result is that the distribution of particle arrival times will have a larger rms value. In this way the 10 ns timing window may be used by application of the N_{fit} cut in order to reject distant showers which trigger the milagro detector with grossly underestimated core distances. According to simulation 90% of these trouble events are eliminated with the application of this cut, while retaining 60% of the original data set.

v Bin Size

The bin size refers to the size of the smoothing bin used for the background and foreground maps. In the previous section the details of the determination of source excesses and background estimates for 0.1° bins on the sky was briefly described. These bins are substantially smaller than Milagro's 0.7° angular resolution indicating that the events originating from a point source in the sky, will occupy many of the surrounding bins. In order to account for this effect a smoothing process is carried out, where the 0.1° bins are combined into a larger square bin for the computation of source excess and significances. Under the assumption of a symmetric energy resolution the optimal bin size is given by

$$r_{\mathrm{opt}} = (1.58 + 0.7e^{-0.88N^{0.36}})\sigma \tag{15}$$

with the optimal circular bin size given by r_{opt}, the angular resolution of the detector given as σ and N as the number of background events expected to be contained with a bin of size σ. In the large N limit equation (15) reduces to $r_{\mathrm{opt}} \simeq 1.58\sigma$. A simple

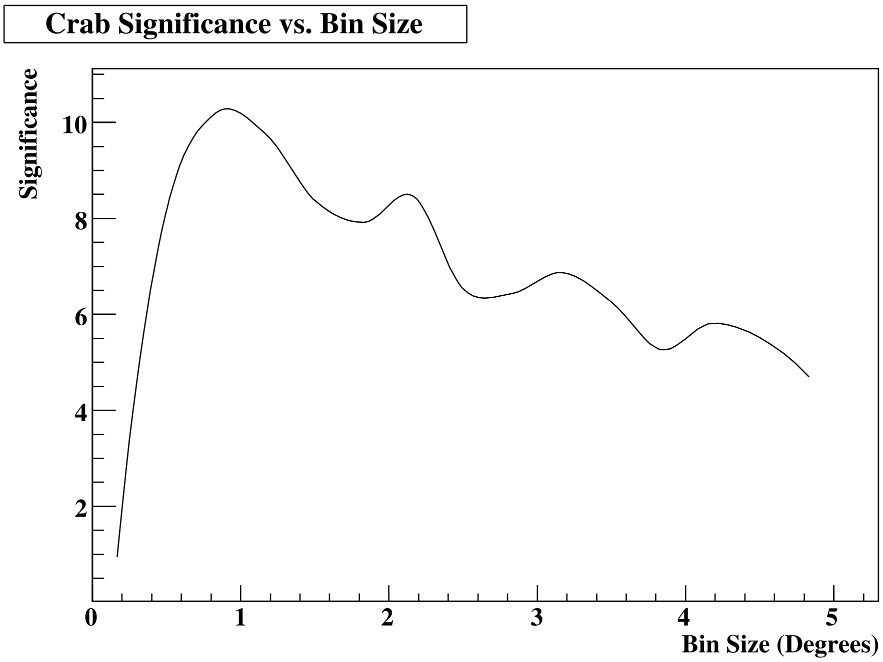

Figure VII: The Significance of the Crab Nebula detection as a function of bin size, as measured from the reconstructed data.

conversion to a square bin with equal area may be preformed giving the same result. In this case the optimum bin size becomes

$$r_{\text{opt}} \rightarrow r'_{\text{opt}} = r_{\text{opt}} \sqrt{\pi \cos(\vartheta)} \tag{16}$$

where r' is the square bin size and ϑ is the declination of the source [15].

IV Sources Detected with Milagro

Using the procedures outlined in this chapter a number of known galactic and extra-galactic γ-ray sources have been detected, such as the Crab Nebula, and Markarian 421. Markarian 501, another active galactic nucleus was detected by the precursor of Milagro, Milagrito, during a strong flare in 1997 [24]. In addition to these sources diffuse emission from the galactic plane in the Cygnus region of the galaxy, defined as $65° \leq l \leq 85°$ and $-2° \leq e \leq 2°$ [8], as well as a further eight unidentified sources have been observed. These have yet to be confirmed by observations of another

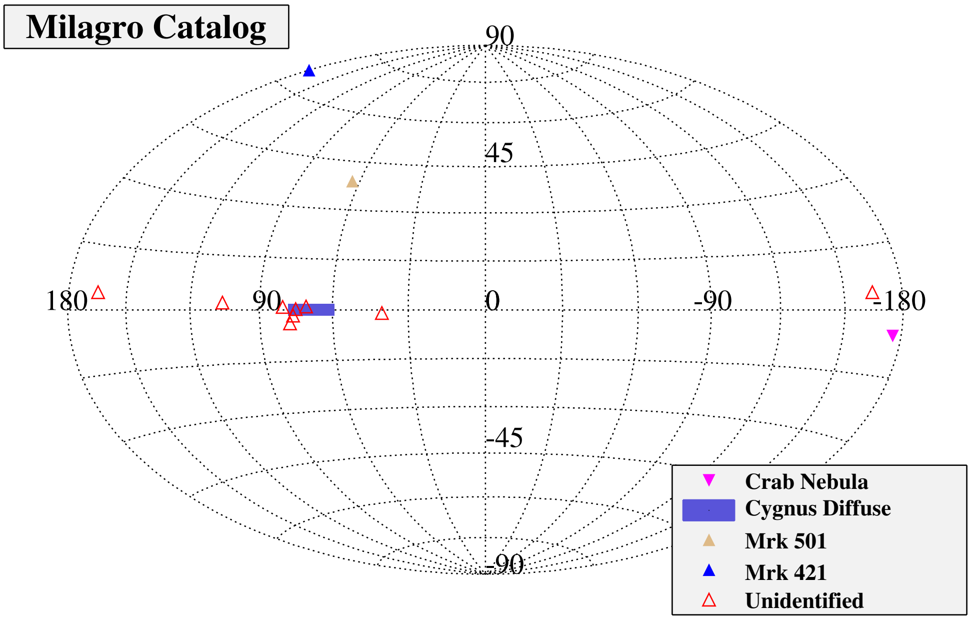

Figure VIII: The Milagro Source Catalog.

experiment, though many of the sources are coincident with unidentified EGRET sources (see figure VIII). One potential source is nearly coincident with the Geminga pulsar which may be a possible source of TeV γ-rays, though this source too has yet to be detected through another method at these energies [6]. There is also evidence that a high energy component from GRB 970417A was detected with the Milagrito detector [25], however none have been definitively observed in Milagro.

These observations were carried out using the entire data set of Milagro, with the exception of the sources detected with milagrito, including data collected previous the installation of the outrigger array. For data collected in the absence of the outrigger array, the limited dynamic range of possible core position makes the confident reconstruction of energies impossible, as the accurate reconstruction of the core is absolutely essential to the proper reconstruction of energies. As discussed in the previous section this limits the amount of data available for spectral analysis to a total of 1349.73 days. This limited data set only allows for a 10.17σ detection of the Crab nebula, in comparison to the $\approx 15\sigma$ detection achieved with the full data set utilizing the A_4 weighting technique. Unfortunately this limits the sources for

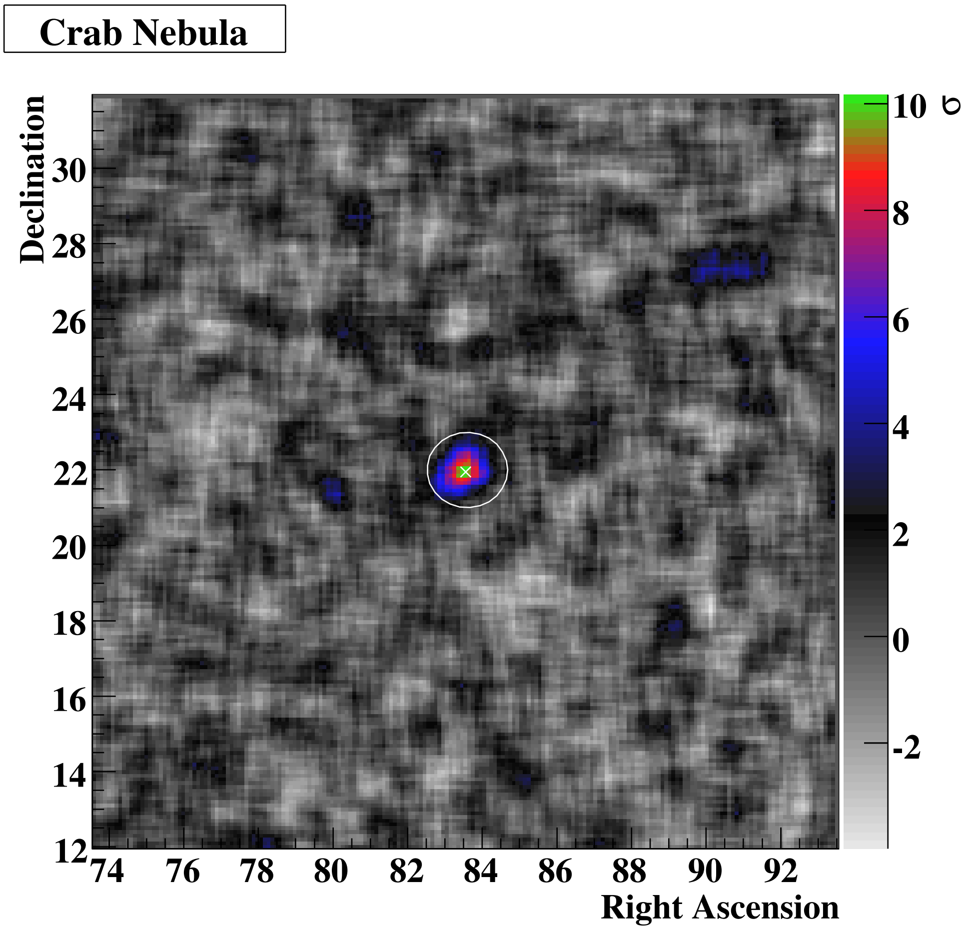

Figure IX: The significance of the Crab Nebula and immediate vicinity thereof, crated using an optimum bin size of 1.0° and a total of 1341.73 days of data available for the reconstruction of spectra.

which an accurate reconstruction of the spectrum may be carried out as well.

After application of this final restriction, the sources which have been observed in Milagro for which spectra may be determined are limited to the Crab nebula, Markarian 421, the diffuse source of γ-rays originating from the Cygnus region of the galaxy, as well as the newly detected source MGRO J2019+37; also known as the Cygnus region "hot" spot. Though the number of sources available for study is currently small, their variety is not. The Crab nebula is a young supernova with a rich history, which has been extensively studied at every accessible wavelength. Markarian 421 is an active galactic nucleus with a relatively small redshift (z=0.031) and represents another very different class of TeV γ-ray source where acceleration of particles is thought to occur in accretion powered jets emanating from a central super-massive black hole. The Cygnus region diffuse emission on the other has two likely sources, namely cosmic ray interaction with molecular gas clouds located in the region, as well as unresolved point sources that are likely to populate the region, of which MGRO J2019+37 may be but one of many. In summary the sources observed with Milagro, though few, provide representative examples of many different types of TeV γ-ray sources, for which spectra may now be measured up to 100 TeV and further insight into their acceleration mechanisms gained.

Chapter IV

The Milagro Energy Reconstruction Algorithm

The development of an energy reconstruction algorithm for the Milagro detector has been my primary preoccupation over the last three years. The ultimate goal of this has been to study the properties of the high energy sources observed by the Milagro detector. As will be discussed in successive chapters the introduction of spectral analysis technique for the Milagro detector provides a means to probe the underlying non-thermal processes responsible for the acceleration of particles to ultra-relativistic energies. This new capability has expanded the role of Milagro from that of a simple survey instrument and all-sky monitor, where sources are observed, the position and absolute flux recorded for later precision study by another instrument, to that of a fully autonomous observatory providing an independent measure of each accessible source's characteristics and behavior.

As noted earlier the raw data for the Milagro detector is discarded due to storage space and cost constraints necessitating the development of an algorithm dependent upon only the quantities available in the reconstructed data set. After careful consideration of detector geometry and detector response to single EAS's it has been determined that a parameter depending upon the reconstructed zenith angle (θ), number of PMT's triggered in the air shower layer ($N_{\rm AS}$), and outrigger layer ($N_{\rm OR}$) correlates well with energy for a fixed reconstructed core distance ($r_{\rm core}$) and small ($\sim 10°$) zenith angle bin. Taking all of these factors into consideration an effective energy estimation algorithm for the Milagro detector has been devised.

I The Energy Parameter and Energy Estimation Algorithm

The Milagro detector itself is an amalgam of a single large planar detector supplemented by many, smaller, spherical detectors. This observation has led to the introduction of a parameter given by

$$\xi = \frac{N_{\rm AS}}{\cos(\theta)} + \langle\omega\rangle\, N_{\rm OR} \tag{1}$$

where $\langle\omega\rangle$ is a constant introduced to compensate for the difference in density of PMT's and triggering efficiency between the air-shower layer and outrigger array. Its value is given as

$$\omega_i = \pi \frac{r_i^2}{r_{\rm AS}^2} \rightarrow \langle\omega\rangle = \pi \frac{\langle r^2 \rangle}{r_{\rm AS}^2} \tag{2}$$

where the distance to the outrigger's nearest neighbor in the array is given by r_i, and the separation distance between each AS photomultiplier is $r_{\rm AS}$. The first half of the expression acts as the "planar" term corresponding to the detector response of the Milagro pond, while the second half represents the weighted response of the outrigger array to a single EAS.

The parameter ξ itself does not constitute a complete energy reconstruction technique as it lacks a dependence on the distance of a EAS's core to the center of the Milagro pond, which is vital to the correlation of detector response with energy. Utilizing only this parameter energy resolutions of approximately 80% are achievable but not sufficient for the reconstruction of source spectra. Restriction of the core distance to a small interval, approximately 30 m for events with the core off the pond and 15 m for events with the core located on the pond, and the determination of the ξ-energy relation within this interval makes possible a more precise estimation of energy with resolutions approaching 50%. Expanding this approach the formulation of a complete energy estimation algorithm with a dependence on $r_{\rm core}$ is possible and may be further improved by the introduction of a number of coarse zenith angle bins.

For the complete energy estimation algorithm each event is sorted into one of six $r_{\rm core}$ bins and one of four θ bins. For each of the 24 independent bins the energy-ξ relation is determined from the Monte Carlo simulation for γ-rays. For a small slice in true energy the median ξ value is determined and stored for the reconstruction of energies (see figure I). In each $r_{\rm core}$-θ bin the median value of ξ and corresponding energy is used to produce a composite function composed of power laws valid over a limited ξ range given by

$$E_{\rm fit} = E_0 \left\{ \frac{\xi}{\xi_0} \right\}^{\ln\left\{\frac{\xi_0}{\xi_1}\right\} \ln\left\{\frac{E_1}{E_0}\right\}} \qquad \xi_0 \leq \xi < \xi_1 \tag{3}$$

where ξ_0 and ξ_1 are the median values of ξ as determined from the parameter distributions at energies E_0 and E_1. With this information the energy estimation algorithm for the Milagro detector is complete and may be used to determine energies on an event-by-event basis.

The energy estimation algorithm for Milagro proceeds as follows for a single event: first the reconstructed core distances and zenith angles are used to determine the proper set of median parameter values for energy reconstruction. Next ξ is calculated for the event and the nearest median parameter values (ξ_0, ξ_1) are determined. From this a reconstructed energy using equation (3) is calculated. Using this technique energy resolutions of approximately 30% are obtainable for energies greater than 10 TeV, using proper cuts (see figure III). Resolutions are obtained through fits to a Gaussian for distribution of the fractional error $(E_{\rm fit} - E)/E$ between -1.0 and 1.0 (see figure II).

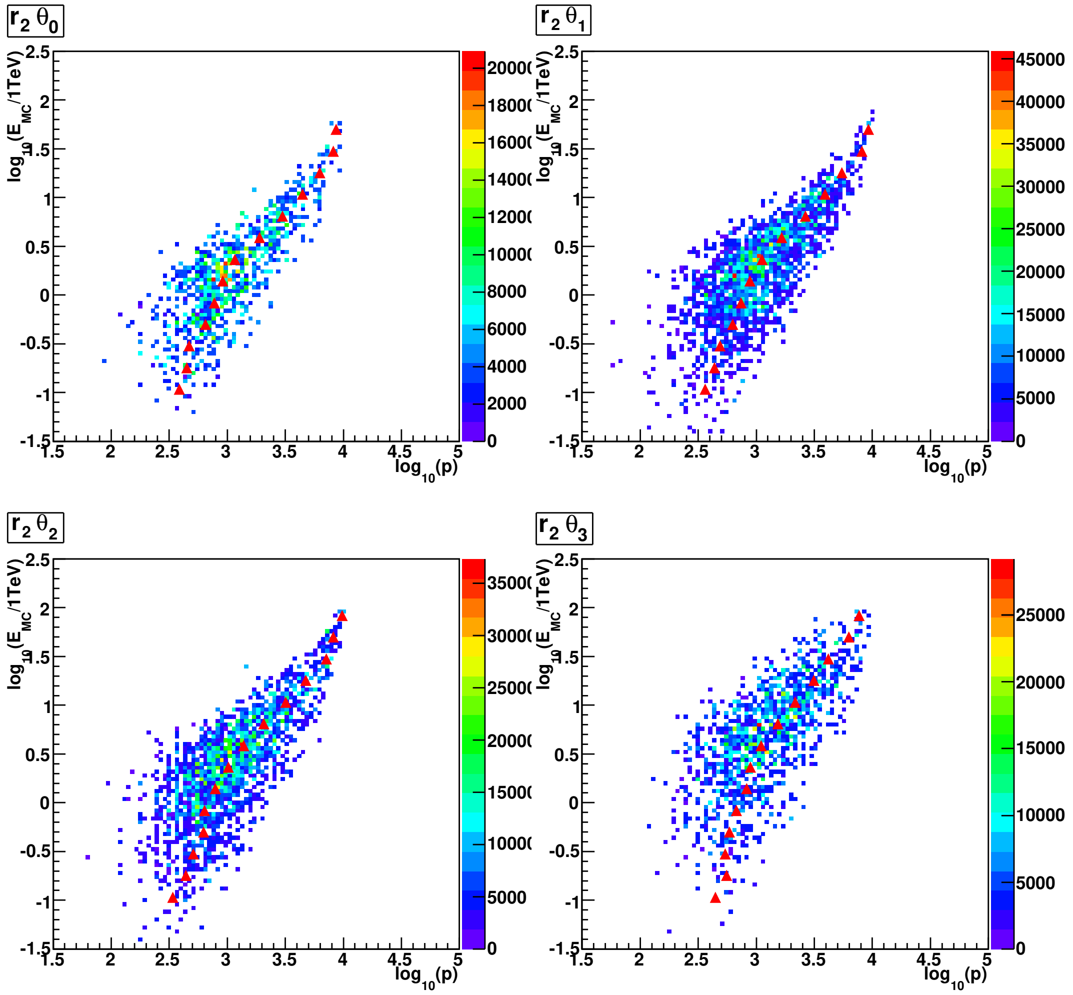

Figure I: The energy-ξ distribution for events with r_{core} between 45 and 60 m. Each of the four distributions represent separate θ-bins (from left to right, top to bottom: 0°-10°, 10°-20°, 20°-30°, and 30°-45°). Each red triangle represents the median ξ value calculated for a slice in true energy.

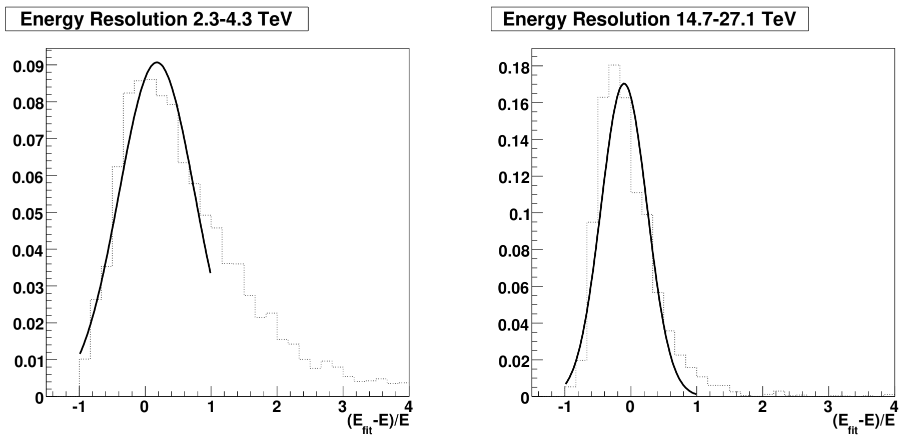

(a) (b)

Figure II: Energy resolution distributions fit to a Gaussian for (a) low energies (between 2.3 and 4.3 TeV) and (b) high energies (between 14.7 and 27.1 TeV).

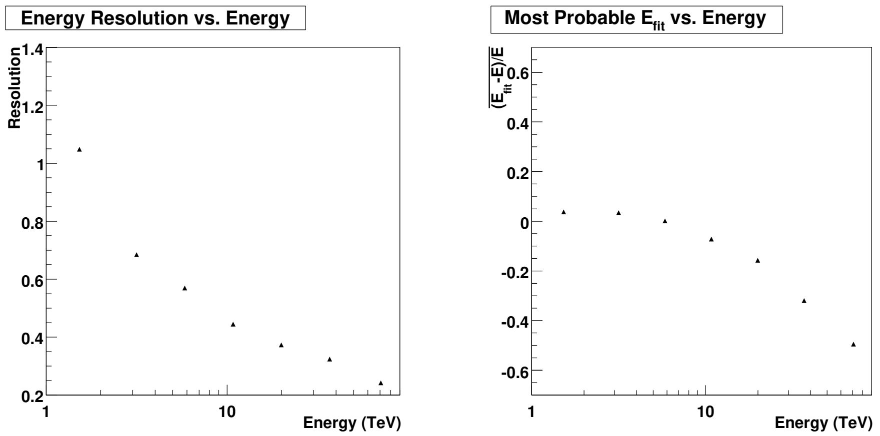

(a) (b)

Figure III: (a) The energy resolutions for Milagro as a function of true energy and the (b) energy bias as a function of true energy as determined from Gaussian fits to the distributions of fractional error $(E_{\rm fit} - E)/E$ (see figure II).

For the energy reconstruction quality cuts must be applied in order to maximize the energy resolution. Taking the standard cuts of $N_{\text{AS}} \geq 80$ and a minimum X_2 cut of 2.5 is insufficient due to the large size of high energy showers some events with primary energies greater than 10 TeV produce. As a result the energies of some events will be underestimated by more than 50% due to an underestimation of r_{core}, fortunately a quality cut of $N_{\text{fit}} \geq 65$ provides a means to combat this difficulty. N_{fit} represents the number of PMT's utilized for the determination of core distance and zenith angle. In order for the PMT to be included in these reconstructions the arrival time of the PMT event must fall within a narrow time window of approximately 10 ns of the mean trigger time. The width of the shower front of an EAS becomes larger with greater distance from the shower core, hence the distribution of the timing pulses broadens with increasing distance from the core providing a rough indication of distance, independent of the core reconstruction algorithm. Enforcement of the N_{fit} cut places a stringent limit on the width of the shower front eliminating 99% of these problematic events. The resulting event-by-event comparison is shown in figure IV. The problem of energy underestimations of approximately 35% above 50 TeV remains due to the limited size of the Milagro detector and outrigger array (see figure IIIb), and there remain at lower energies an asymmetric tail due to events whose energies are overestimated (see figure IIa). In order to properly reconstruct source spectra an algorithm has been devised which takes these effects into account.

II Determination of Source Spectra

The energy estimation algorithm makes possible the accurate estimate of energies in the Milagro detector above 1 TeV, however there remain at energies less than approximately 4 TeV events whose energies are overestimated by a factor of 4 or more. Additionally for events at energies above approximately 30 TeV there still remains a small systematic underestimation of the energies. This necessitates the

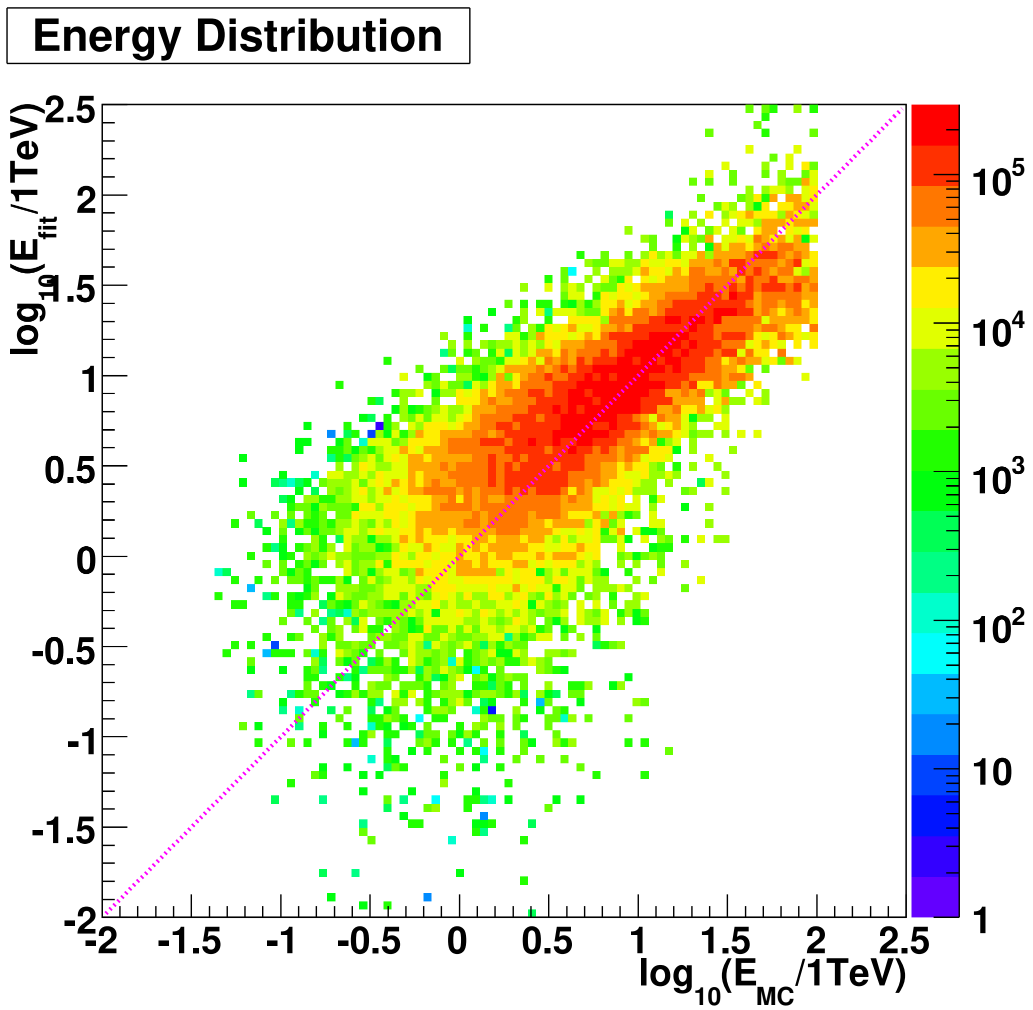

Figure IV: An event-by-event comparison of the true energy and fit energy utilizing the the standard cuts plus the additional cut of $N_{\rm fit} \geq 65$

introduction of a spectral determination algorithm which appropriately compensates for both of these effects. For Milagro, spectral fits are carried out using a forward analysis which incorporates resolution functions calculated from simulated events in order to make accurate determination of spectra. This contrasts sharply with the methods currently used by IACT's for spectral determination which are most familiar to the γ-ray astronomy community.

Spectral fits by HEGRA and HESS are carried out in the following manner: all events are divided into separate fit energy bins. For each energy bin a flux is calculated from the data using

$$\frac{d\phi}{dE}_j = \frac{1}{T\delta E}\left[\sum\frac{1}{A_{\rm eff}^{\rm on}} - \alpha\sum\frac{1}{A_{\rm eff}^{\rm off}}\right] \tag{4}$$

where T is the total integration time, δE the range of the j-th energy bin, α is the ratio of the solid angle for the on- and off-source observation regions, and $A_{\rm eff}^{\rm on}$ and $A_{\rm eff}^{\rm off}$ are the effective areas determined from the reconstructed energy of an on- and off-source event. A correction for deadtime is applied for the flux in each energy bin as well as an additional correction for network outages and faults which impede the storage of some events. The energy for each point is fixed as the center of the energy bin in logarithmic space, given by

$$\langle E\rangle_j = \sqrt{E_j^{(0)}E_j^{(1)}} \tag{5}$$

where $E_j^{(0)}$ and $E_j^{(1)}$ are the upper and lower bounds of the j-th energy bin, then fit to a power law or some other spectral form for all points giving the measurement of the source spectrum. For these fits energy bins with widths three times that of the energy resolution are taken in order to eliminate the effect of event over- and underestimation on neighboring bins, in other words to reduce the number of events wrongly assigned to a particular energy bin. The energy resolution of HEGRA is approximately 10% and nearly constant over the entire energy range making effects due to under- and overestimations for a steeply falling spectrum negligible [10].

In Milagro, where the energy resolution is not constant across the entire range and asymmetric at lower energies, such effects become significant and must be considered in order to properly reconstruct the source spectrum. For this reason the spectral fits are carried out by dividing the data into N fit energy bins within which the number of excess events and corresponding significances calculated. The source spectra are then reconstructed by comparing the number of measured events with the number of expected events for a single source transit. The expected number of events is calculated from the Monte Carlo data though

$$\widetilde{N}_j(\vec{\gamma}) = \int_{0^\circ}^{45^\circ} d\theta \int_{0.1}^{120} dE' \left\{ \epsilon(\theta) f_j(E') \left.\frac{d\phi(\vec{\gamma})}{dE}\right|_{E'} A_{\text{eff}}(E', \theta) \right\} \tag{6}$$

where the integration is carried out over the zenith angle and true energy (E'); $\epsilon(\theta)$ is the exposure of a particular source as a function of the zenith and $\left.\frac{d\phi(\vec{\gamma})}{dE}\right|_{E'}$ is the flux of the assumed spectrum with parameters $\vec{\gamma}$ as a function of energy. The resolution function, defined as

$$f_j(E') = \int_{E_0}^{E_1} dE f(E', E) \tag{7}$$

where E_1 and E_0 are the upper and lower energies of the j-th fit energy bin and $f(E', E)$ is defined as the probability that an event with true energy E' will be reconstructed with an energy between E and $E + dE$, is included to account for any under- and overestimation of energies. A χ^2 minimization process utilizing the MINUIT package is carried out by defining a χ^2 as

$$\chi^2(\vec{\gamma}) = \sum_{i=1}^{N} \left\{ \frac{\widetilde{N}_i(\vec{\gamma}) - N_i}{\sigma_i} \right\}^2 \tag{8}$$

and minimizing as a function of the parameters of the assumed spectrum $(\vec{\gamma})$.

More recent versions of the Milagro analysis have introduced the use of weights for a more precise error analysis. As described earlier each event in a sky map is assigned a weight based upon the number of PMT's utilized in the reconstruction ($N_{\rm fit}$) and X_2. Background estimation, subtraction, and a determination of excess events is carried out yielding a sky map of excess weights and corresponding significances. Equation 6 is modified in order to accommodate the use of the weighted analysis through the introduction of a weight function $w(E', \theta)$

$$\widetilde{W}_j(\vec{\gamma}) = \int_{0^\circ}^{45^\circ} d\theta \int_{0.1}^{120} dE' \left\{ \epsilon(\theta) f_j(E') \left. \frac{d\phi(\vec{\gamma})}{dE} \right|_{E'} A_{\rm eff}(E', \theta) w(E', \theta) \right\} \tag{9}$$

giving the number of expected excess weights for a single transit in each energy bin ($\widetilde{W}_j(\vec{\gamma})$) as a function of the parameters of the input spectrum. In a manner identical to that above a χ^2 minimization is carried out in order to determine the fit spectrum and associated statistical error of the spectral parameters.

In order to test for potential bias or programming errors within the analysis software two tests have been preformed. The first test is based upon the generation of simulated point sources with different spectra using the Monte Carlo data set of γ-rays. These simulated sources are then added to the sky maps generated from the Milagro reconstructed data in order to provide the appropriate background for source significance calculations. Following the procedure outlined above the spectra of the simulated sources are reconstructed and compared with the input spectrum. Agreement within statistical errors with the input spectra serve as a test of the spectral reconstruction software.

As an additional test a measurement of the cosmic ray spectrum was preformed between 1 and 100 TeV using the background triggers from the Milagro detector. A 1.3° bin fixed in celestial coordinates is tracked through a approximately 100 transits taken randomly from the available Milagro data set and the background events measured within the bin summed. The significance computation for this measurement differs from that of the previous measurement as fluctuations in the detector trigger rate are the dominant source of uncertainty for this measurement.

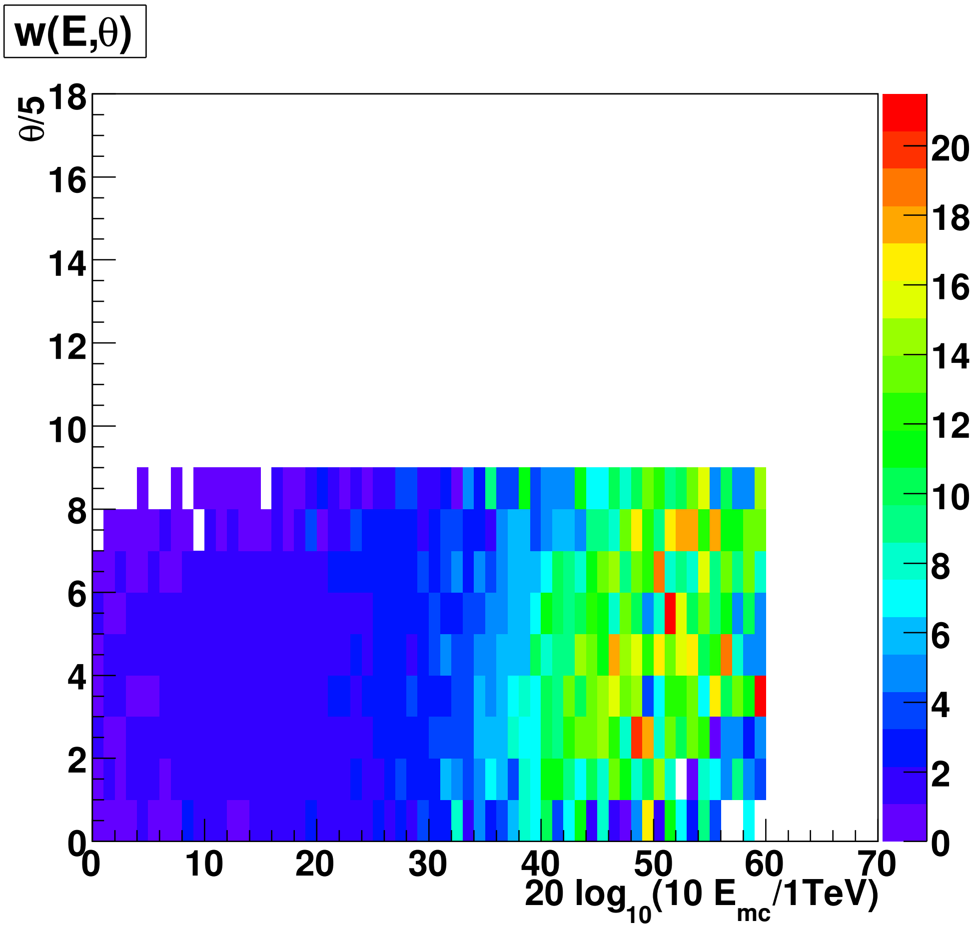

Figure V: The weight function $w(E, \theta)$ calculated from Monte Carlo for the determination of spectra.

Therefore the error of the measurement is taken as

$$\sigma = \frac{1}{N} \sum_{i=1}^{N} \left\{ \frac{n_i - \langle n \rangle}{\langle n \rangle} \right\}^2 \tag{10}$$

in place of the usual significance computation with N as the number of data subsets, n_i is the background rate measured in the i-th subset and $\langle n \rangle$ is the average background rate for the entire data set. This has yielded a measurement for the spectral index of the cosmic ray spectrum of -2.71 ± 0.04, which is in good agreement with the measurements of the JACEE [23] and RUNJOB [45] experiments.

Chapter V

Physical Background of Astrophysical γ-ray Point Sources

Milagro has observed many point sources of astrophysical γ-rays, both galactic and extragalactic. The spectra of these sources may be easily explained through the Fermi acceleration mechanism, though a more detailed understanding of the dynamics of these systems is required in order to determine the exact nature of the standing shock and the surround medium as well as to interpret the measurement of TeV γ-ray spectra. Here a brief review of the different processes affecting high energy acceleration mechanisms of pulsars and AGN's are outlined.

I Pulsar Wind Nebula

Pulsar wind nebula are the oldest class of TeV γ-ray source discovered and have been extensively studied over the entire range of the electromagnetic spectrum. The most famous and well studied of these objects is the Crab nebula, which was first observed by the Whipple collaboration in 1989 at energies in excess of 1 TeV [113]. The history of this object is much more extensive.

i A Brief History of the Crab Nebula and Pulsars

In the summer of 1054 an unusually bright and long lasting "guest star" appeared in the eastern sky. This event was recorded by ancient Chinese astronomers in the *Sung-shih* ("History of the Sung Dynasty") and Japanese astronomers in *Kaitai Sizaki-Shuran* and *Mei Getsuki*. The guest star is reported to have been visible between July 4, 1054 to April 17, 1056 [48]. In the beginning of last century it was determined that this phenomenon was coincident with the position of the Crab nebula at that time [87] and that the guest star of 1054 was in fact the supernova event which gave rise to the nebula itself. The Crab nebula was discovered in 1731 by the English astronomer John Bevis and independently by Charles Messier in the 1750's. Since this time the nebula has been an object of intense study due to its many unique features. The Crab was first detected as a radio source in the middle of the last century [37], and has been observed at every other wavelength since that time. The Crab nebula is the brightest radio, X-ray and γ-ray emitting object in the northern hemisphere, with a flux two orders of magnitude higher than expected from measurements of the IR spectrum. Even previous to these detections there were questions as to the source of the nebula's energy. As early as the 1940's a central star had been identified as a potential source of energy but was apparently only of the 16th magnitude, insufficient for the observed emissions of the entire nebula. Additionally the acceleration of the expansion rate of the nebula (measured at that time to be 10^{-3} cm/s^2) also proved puzzling as the radiation pressure that could be supplied by such a star was insufficient [29]. Measurements taken that year gave $\mathfrak{L} \approx 3 \times 10^4 \mathfrak{L}_\odot$ and $R \approx 2 \times 10^{-2} R_\odot$ which lead to the false identification of this object as a white dwarf that was assumed to have from subsequent to the supernova event in 1054 [90]. In the following decade it was suggested that much of the optical emission within the nebula could be the result of synchrotron radiation, should relativistic particles be injected into the source with energies between approximately 10 GeV and 1 TeV was in agreement with spectra measured by Dombrovskii in 1954

[102]. The source of the electron acceleration of course remained enigmatic until the relatively recent discovery of a new class of objects, now known as pulsars.

During the 1960's advances in radio astronomy made possible the first observations of what were originally termed LGM's (little green men); the term originating from the periodic pulses originating from unidentified point sources. The first detections were made by Hewish and Bell in 1967 with the first observation of CP 1919, and later observations of additional sources with periods of $P_{\mathrm{CP}\ 1919} = 1.3372795 \pm 2 \times 10^{-6}$ s, $P_{\mathrm{CP}\ 0834} = 1.27379 \pm 8 \times 10^{-5}$ s, $P_{\mathrm{CP}\ 1133} = 1.1880 \pm 4 \times 10^{-4}$ s, and $P_{\mathrm{CP}\ 0950} = 0.253071 \pm 8 \times 10^{-6}$ s [67, 68]. In the beginning the observation of an optical companion proved difficult due to the small size of the source leading to much speculation as to the source of these radio pulses. It was soon realized that these pulses likely originated from rapidly rotating magnetized neutron stars. Neutron stars had been proposed as an end state of stellar evolution by Baade and Zwicky as early as 1934 [30], however observational evidence for this assertion was scarce at the time. A simple model of a pulsar with a dipole magnetic field was introduced by Julian and Goldreich in 1969 after the suggestion that pulsars, as they came to be known, were responsible for the radio pulses and the potential source of energy at the center of the Crab nebula [95, 96, 57]. This argument was further bolstered through the discovery of NP 0532 at the center of the Crab nebula [105], the subsequent identification of optical emission possessing an identical pulsation period [40] and the observation that nearly all of the optical emission is emitted within these pulses [82]. The Julian-Goldreich model consists of a single rotating neutron star with a dipole magnetic field aligned with the axis of rotation. Under the assumption that the interior of the neutron star is a good conductor the Lorenz invariant $\vec{E} \cdot \vec{B}$ vanishes in the interior of the neutron star. On the surface however,

$$\vec{E} \cdot \vec{B} = -\left\{ \frac{\Omega R^8}{c r^7} \right\} B_0^2 \cos^2(\theta) \tag{1}$$

with Ω as the angular frequency with which the pulsar rotates, B as the magnetic field strength. $\vec{E} \cdot \vec{B} \neq 0$ would not allow for a state of equilibrium, should the neutron star be surrounded by a vacuum. It was concluded by Julian and Goldreich that a pulsar must be surrounded by a co-rotating magnetosphere. Outside of the light cylinder, where co-rotation of particles becomes impossible due to relativistic effects, charge is lifted off the surface of the neutron star by the electric field, forming a wind that flows away from the pulsar and collides with material from the surrounding supernova remnant or interstellar medium. This charge manifests itself in the form of both electrons at higher latitudes and protons at lower latitudes, such that the pulsar itself does not accumulate any charge [58]. The acceleration of charges along the open field lines give rise to the observed radio and optical pulses. In the general case, where the dipole moment in not aligned with the rotational axis of the neutron star (see figure I), the emissions are focused into a narrow beam (with an opening angle of less than $10°$) which remains aligned with the dipole moment. Thorough this mechanism the pulsar emits photons in a fashion similar to a lighthouse, where we observe the beam only while it is oriented toward us. The origin of the emission is currently thought to be the coherent acceleration along the dipole moment (of the pulsar) of charge "sheets" oriented perpendicular to direction of acceleration which result in the creation of radio, and in the case of younger pulsars, X-Ray and optical beams. The dominant source of charge is a electron-positron plasma that is created through a synchrotron cascade. As an electron is accelerated along the curved magnetic field line synchrotron photons are emitted, which in the presence of the strong magnetic field produce electron-positron pairs that undergo the same process generating additional pairs providing the charge in the sheets. For protons accelerated from the surface of the star this effect does occur, but further away from the surface of the neutron star, generating the same electron-positron plasma [106].

The generation of radiation and acceleration of particles are all completely powered by the rotational energy of the pulsar. As a result the pulsar slows gradually as energy is extracted through these processes. As an illustration of the evolution

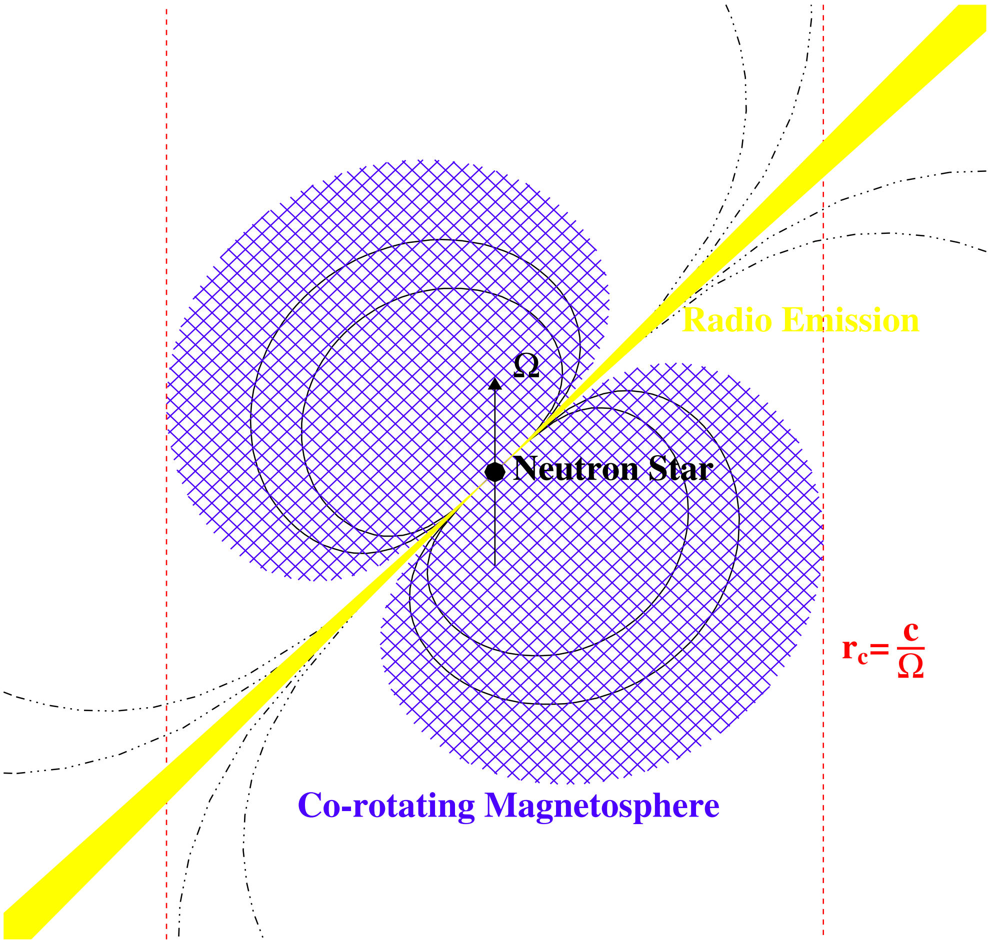

Figure I: Schematic of a magnetized pulsar rotating with angular velocity $\vec{\Omega}$. The solid lines represent closed $\vec{B}$ field lines while the dashed represent open $\vec{B}$ field lines.

of pulsars, three specific examples are displayed in figures I and II. Subsequent to the outbreak of a supernova a pulsar is created as the star collapses in on itself. During this event the pulsar is "spun up" due to conservation of angular momentum, and a high strength magnetic field $B \sim 10^{14}$ Gauss is created due to conservation of magnetic flux. As the pulsar ages the period lengthens and the magnetic field decays causing the rate of change of the period to decrease simultaneously. An order of magnitude estimate for the age of a pulsar may be made, by assuming all of the energy lost is due to magnetic dipole radiation of an oblique rotator. Based on this assumption the angular velocity and rotational kinetic energy may be expressed as

$$\Omega = \Omega_0 \sqrt{1 + \frac{2t}{\tau}}^{-1} \tag{2}$$

$$\dot{E} = \frac{2E}{\tau} \tag{3}$$

with Ω as the current angular velocity and E the rotational kinetic energy of the pulsar. The characteristic time $\tau' = \tau/2$ may be expressed as $\tau = \Omega/\dot{\Omega}$ which gives an order of magnitude estimate for the age of a pulsar [60]. Application of this estimate for the population of known pulsars is displayed in figure IV. Figures IV, II, and III gives a good overview of the evolution of pulsars including three well known examples, the Crab nebula ($\tau' = 1237$ yr), Vela ($\tau' = 11289$ yr), and Geminga ($\tau' = 342535$ yr). A better age estimate for these systems may be obtained for a pulsar by considering evolution for the general case where $\dot{\Omega} = -k\Omega^n$, with n representing the breaking index and k is some proportionality constant. The age estimates from τ' are based upon the special case for a breaking index of $n = 3$, equivalent for energy loss purely as a result of dipole radiation, and are likely to overestimate the pulsar age. Currently only 5 breaking indices, with values ranging between $n = 1.4 \pm 0.2$ for the Vela pulsar [83] and $n = 2.91 \pm 0.5$ for PSR J1119-6127 [38], have been measured with confidence [55].

With the discovery of additional pulsars it has been recognized that two distinct pulsar populations exist, millisecond pulsars and canonical pulsars (see figures

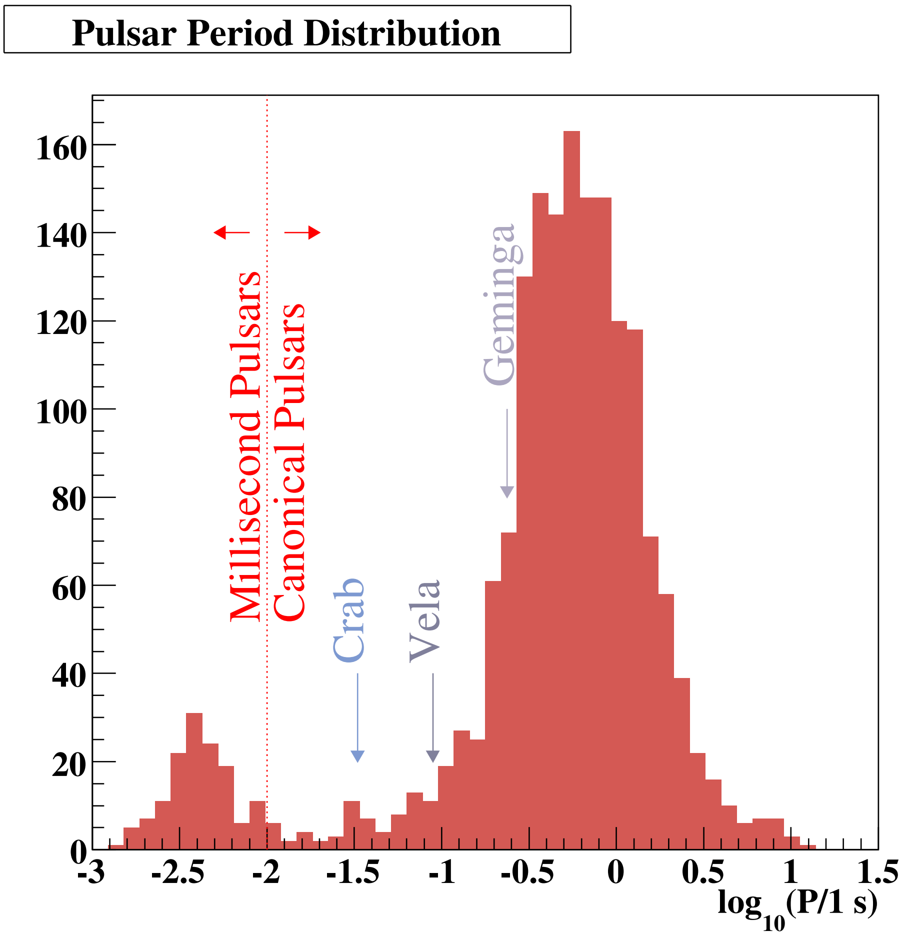

Figure II: Distribution of pulsar periods. Here two populations of pulsars, canonical and millisecond, are clearly visible (data from [84]).

II). Currently canonical pulsars are believed to be younger due to their detection within supernova remnants such as the Crab nebula, Vela, and Geminga. As the pulsars age their magnetic field decays causing a reduction in their luminosity. For pulsars with a binary companion coherent accretion of material onto the pulsar may cause the pulsar to gain a large amount angular momentum. As the angular velocity of the pulsar increases, so does the luminosity, allowing some of these pulsars to become visible again in the form of millisecond pulsars. The vast majority of these objects are found in binary systems (see figure III) lending credence to this argument. Though some of these pulsars do emit radiation in X-rays the vast majority are radio pulsars. Only relatively young pulsars emit photons in the MeV to TeV

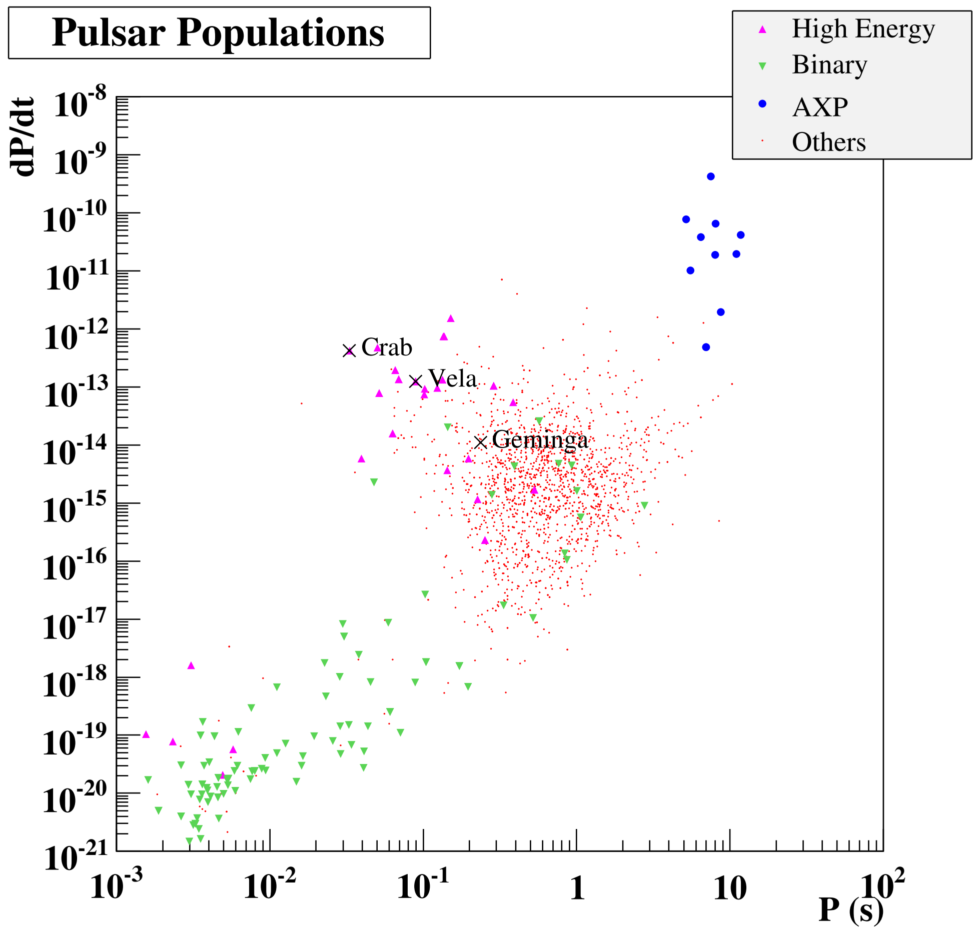

Figure III: Various pulsar populations and the distribution of periods vs. the change in period over time (raw pulsar data from [84]). AXP's are anomalous X-ray pulsars, which are now assumed to be magnetars, and high energy pulsars are those emitting pulsed emission above 1 MeV.

ranges, as these emissions occur not as a direct result of the pulsar, but because of the effects within material surrounding the pulsar. Studies at TeV energies give us insight the early stages of pulsar evolution providing insight into the development of these objects, as well as their effects on the surrounding universe. One of the most important effects under study is the potential acceleration of protons and heavy nuclei within such objects which may possibly contribute to the cosmic ray background.

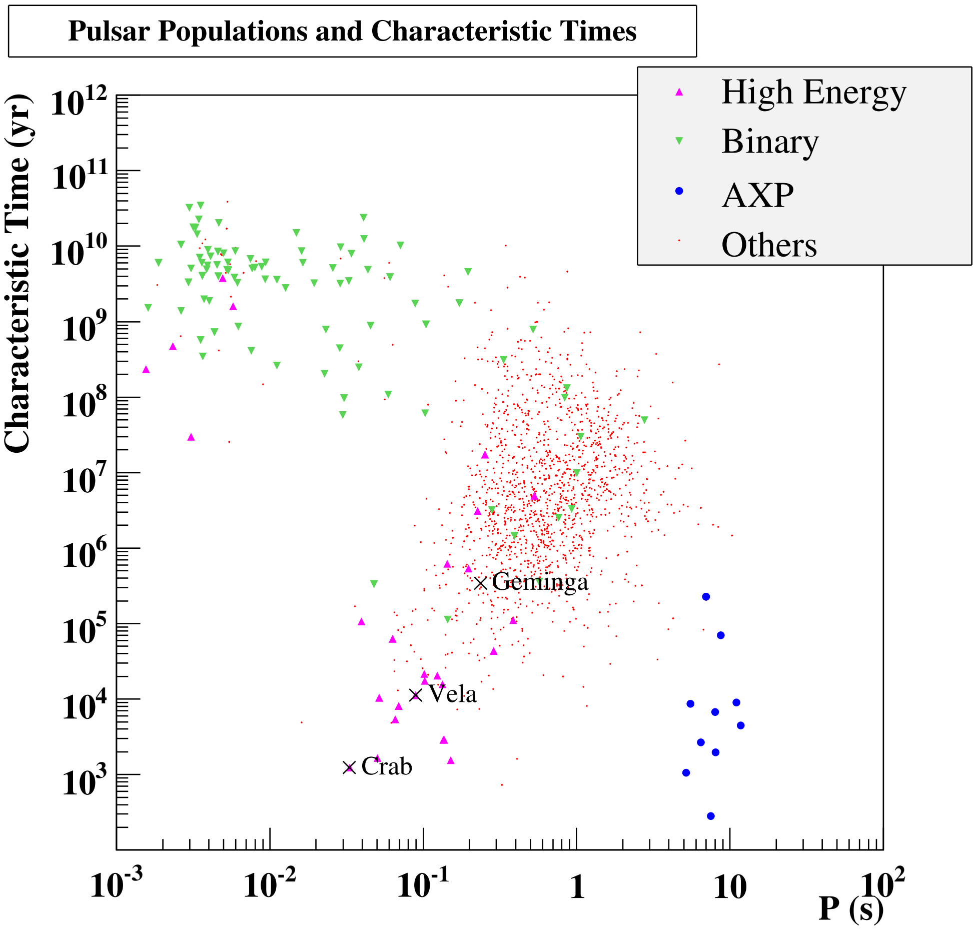

Figure IV: Various pulsar populations and an order of magnitude age estimate based on energy loss of a magnetic dipole radiator (raw pulsar data from [84]).

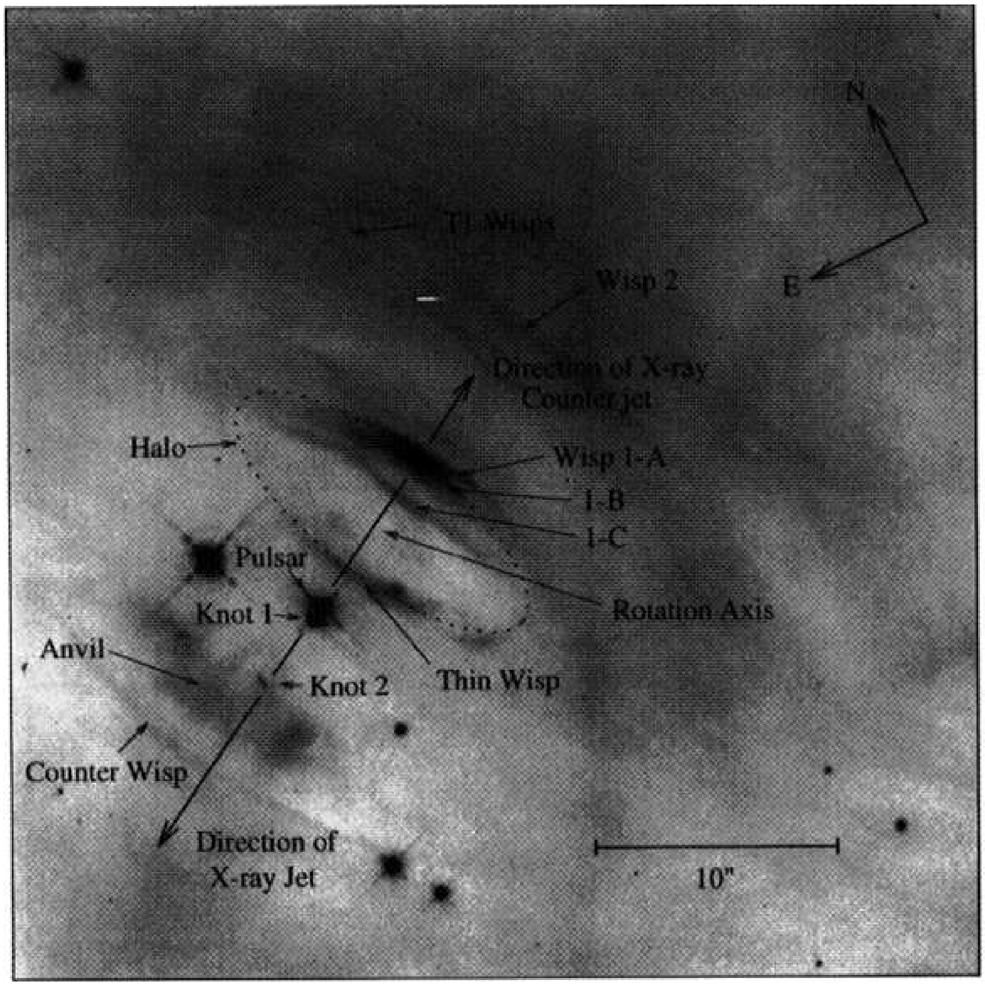

Figure V: A view of the Crab Nebula X-Rays. The torus is clearly visible as are the the various observed structures (from [66]).

ii Observed structure of the Crab Nebula

The Crab nebula is now one of the most studied astrophysical objects in history, and the observations of its properties are extensive covering all accessible energies in the electromagnetic spectrum. A summary of these observations serve as the basis for our understanding of the TeV γ-ray emission which are observed with Milagro and other ground based γ-ray observatories.

The Crab nebula is what is commonly referred to as a "filled center" supernova remnant or plerion, which stands in sharp contrast the more common shell type supernova remnants which have been widely observed. In the optical wavelengths the crab nebula appears as a mass of filaments which is approximately the shape of an ellipse. Spectral observations of these filaments have revealed that they are rich in helium as well as carbon, oxygen, and other heavier elements. The filaments have a typical electron density of 1300 cm^{-3} with values ranging between 550 up to 3500 cm^{-3}, with electron temperatures between 11000 to 18300 K [53]. It has been recently theorized that the presence of the filaments are likely caused through a Rayleigh-Taylor instability which manifests itself though the mixing inward falling material, composed primarily of helium, with the outward flowing and less dense plasma [36].

In high resolution X-ray observations of the crab an entirely different structure appears. In the place of the oblate spheroid a torus with two jets expelling material on opposite sides of the central pulsar approximately perpendicular to the torus are clearly visible. Observations of variability in the optical through X-ray regimes have also produced spectacular views of structure and changes within that structure a distance of approximately 1500 AU distant from the pulsar. These structures are currently though to be a MHD shock formed as the result of wind generated by the pulsar interacting with the surrounding plasma (see figure V) [66].

iii Magnetohydrodynamic (MHD) Model of the Crab Nebula

These effects occur due to the presence of a magnetohydrodynamic shock which is a direct cause of the radiation emitted from the pulsar. This effect was first outlined by Rees and Gunn in 1974, when they examined the interaction of the pulsar wind with the surrounding supernova remnant for the case of the Crab nebula. It was noted that energy would be extracted from the pulsar in three forms the first being the emission of electromagnetic radiation in the form of a 30 Hz wave, the second being the stream of particles escaping the pulsar, and the a toroidal magnetic field which arises as a result of the particle wind. The total energy accumulates in a cavity within the supernova remnant which expands with a velocity $\dot{R}_n \ll c$. At a characteristic distance from the pulsar, where the ram pressure balances the total pressure within the supernova remnant, a shock will form, or

$$\frac{\mathfrak{L}}{4\pi R_s^2} \sim \frac{3\mathfrak{L}T}{4\pi R_n^3} \tag{4}$$

with T as the total age of the nebula, and $\mathfrak{L}$ the luminosity of the pulsar. Assuming constant $\mathfrak{L}$ and growth $\dot{R}_n$ of the supernova remnant over its lifetime, the distance of the shock may be estimated as

$$\frac{R_s}{R_n} = \sqrt{\frac{\dot{R}_n}{3c}} \tag{5}$$

which give a value of approximately 0.07 for the crab nebula. It is important to note that a MHD shock of this form would provide a site capable of accelerating particles through the Fermi mechanism to TeV energies. The absence of the 30 Hz wave in observations also led the Rees and Gunn to the conclusion that it is absorbed at or near R_s and the energy transfered to relativistic electrons [98].

An extension of this model was introduced by Kennel and Coroniti in 1984 which gives a full MHD solution for the nebular flow, completely describing the confinement of the pulsar wind and describing the formation of the MHD shock at R_s. $\mathfrak{L}_{\mathrm{mag}}$, $\mathfrak{L}_{\mathrm{par}}$. The model requires a few basic and important assumptions: firstly the filaments within the crab nebula are assumed to have a negligible effect on the propagation of the plasma thorough the nebula. This first assumption is supported by radio observations, where no significant change in the spectrum was observed in the vicinity of the filaments. The second assumption is that the nebula behaves adiabatically after the shock, which may only be taken as an approximation as the nebula also loses energy though synchrotron emission. The third assumption is that the crab may be modeled as a sphere, which is at best a gross approximation, but necessary for the determination of an analytic solution.

The result is a full MHD model, which describes the transport of particles and EM energy in terms of a single parameter $\sigma = \mathfrak{L}_{\mathrm{mag}}/\mathfrak{L}_{\mathrm{particle}}$, which was originally

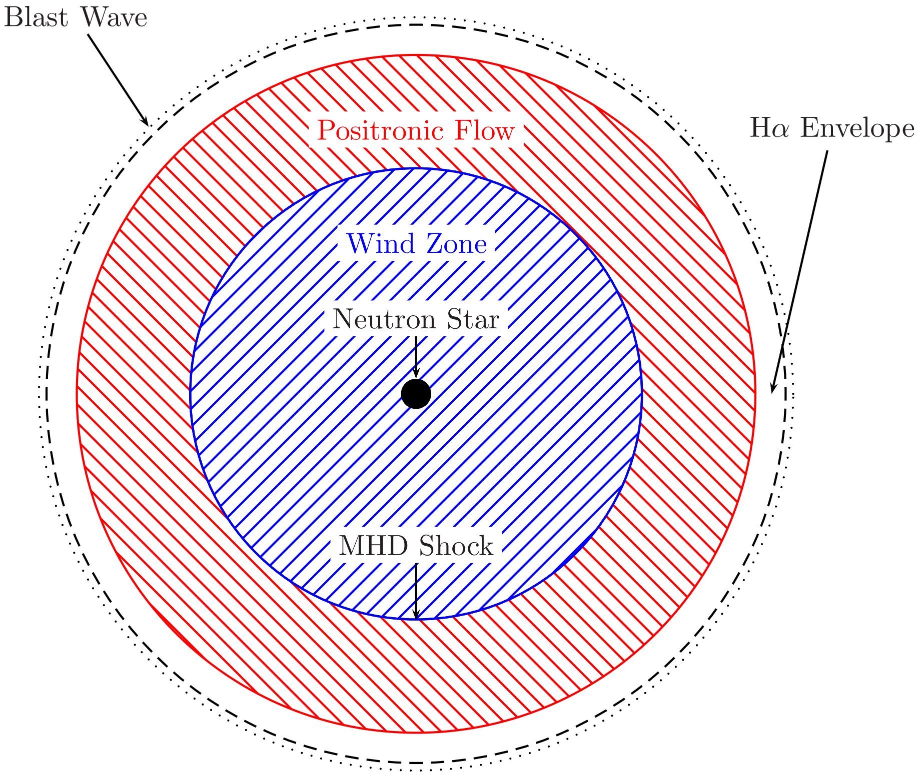

Figure VI: A schematic of the Kennel-Coroniti MHD model of a pulsar with a logarithmic distance scale. At the center the rotating, magnetized neutron star drives a electron-positron pair plasma to a distance $R_s \approx 0.1$ pc, where a relativistic shock forms. The Post-shock plasma flow comprises the remaining "traditional" nebula and terminates at a distance of $R_n \approx 2$ pc. The Hα envelope is located at a distance of approximately 8 pc.

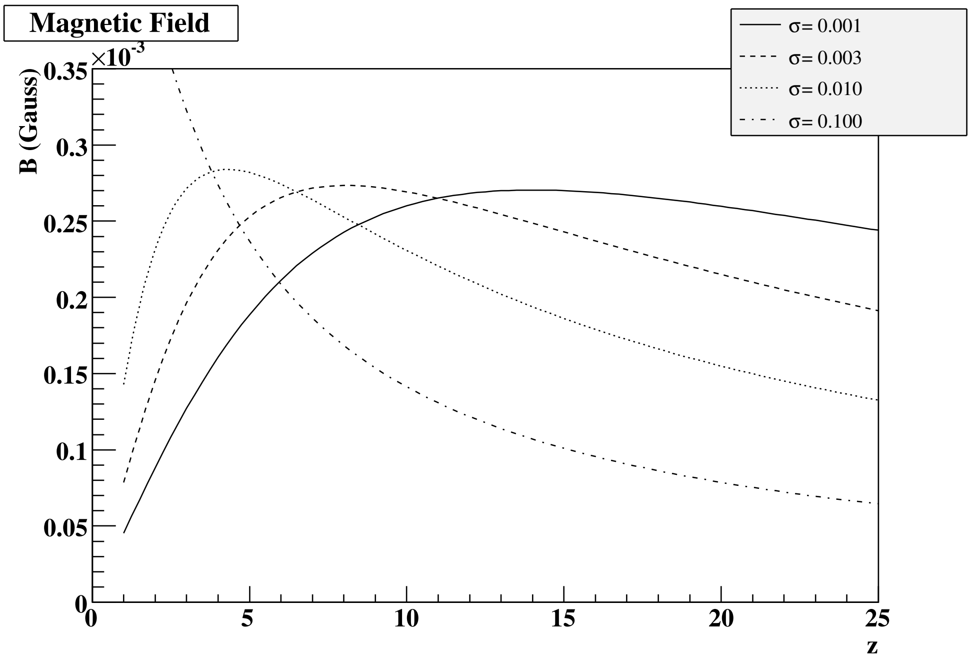

Figure VII: Post shock magnetic field strength for different values of the parameter σ calculated from the MHD solutions from [74] in the $\sigma \lesssim 0.1$ approximation, with the parameter $z = r/R_s$, $\mathfrak{L} = 5 \times 10^{38}$ erg s^{-1} and $R_s = 3 \times 10^{17}$ cm.

introduced in [98]. As the wind flows outward through the magnetic field of the pulsar synchrotron photons are emitted in a characteristic power laws spectrum, which may be used to determine the parameter of this model. The best fit to the measured synchrotron spectrum for the crab nebula yields the following parameters values

$$\sigma = 0.003$$

$$u_1 = 3 \times 10^6 \text{ cm s}^{-1}$$

$$\mathfrak{L} = 5 \times 10^{38} \text{ ergs s}^{-1}$$

$$R_s = 3 \times 10^{17} \text{ cm}$$

where u_1 is the upstream wind velocity and $\mathfrak{L}$ is the total luminosity of the pulsar. The shock distance from the pulsar is also consistent with the observation of an area of low luminosity surrounding the pulsar, as would be expected from a region with a relativistic outflow [75].

iv SSC Model of the Crab Nebula

With the launch of the Compton γ-ray observatory observation and simultaneous observation with ground based ACT's, it became apparent that the high energy spectrum of the crab nebular contains a synchrotron peak and a higher energy peak. A natural explanation which had been introduced previously is the synchrotron self Compton model which was introduced by Gould in 1965. The original flux calculations, however, proved to be approximately a factor of 3 to an order of magnitude too large. This model was revisited in detail in the context of the Kennel-Coroniti model, by Harding and DeJager [43]. After the discovery of TeV emission from the crab [113] and observations of the crab from 0.1 MeV up to $\approx 10^4$ MeV the SSC model once again appeared a promising candidate for the explanation of the double peaked spectrum at energies in excess of 1 MeV.

The essentials of the model presented in [43] are as follows: As the electrons are transported outward as a positronic wind, the high strength magnetic field present in the nebula induces the creation of synchrotron photons up to a characteristic cutoff value determined by the strength of the nebular magnetic field. The energy spectrum of the synchrotron component is dominated by the energy spectrum of the injected electrons. At the shock a potential drop provide electrons an acceleration site where the maximum obtainable energy is given by

$$E_{\rm max} \approx eV_{\rm s} \approx eB_sR_s \tag{6}$$

which for our optimum parameter of $\sigma = 0.003$ gives $E_{\rm max} \approx 5 \times 10^{15}$ eV. This population of high energy electrons interact with seed photons, taken here to consist only of the synchrotron photons, via inverse Compton scattering producing a population of high energy (10 MeV $\rightarrow$ 100 TeV) γ-rays. In the Klein-Nishina limit this maximum electron energy approximately equals the maximum obtainable photon

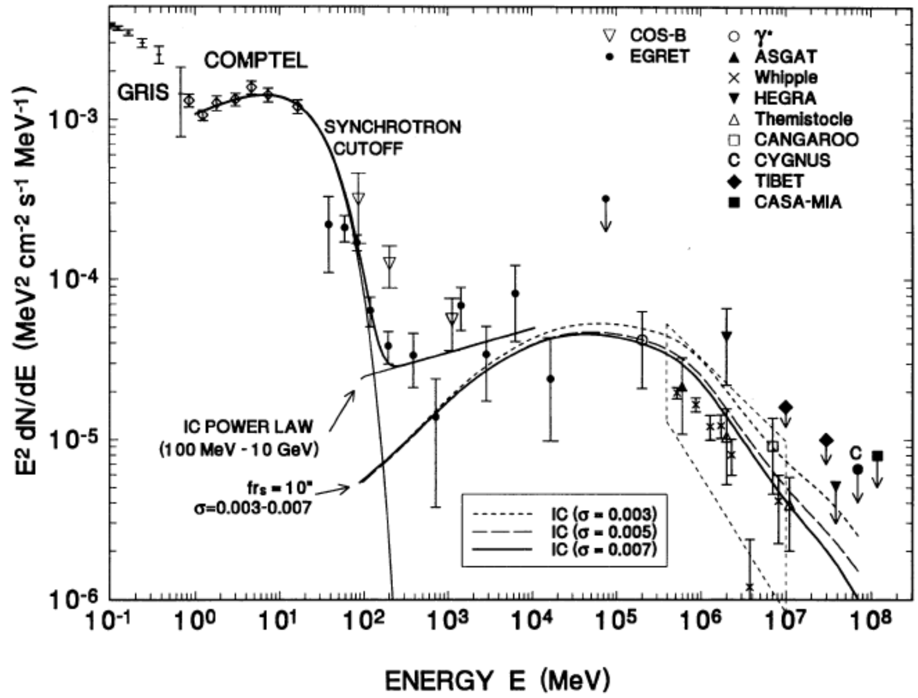

Figure VIII: Measured spectra of the Crab nebula from CGRO instruments and Whipple, as well as the SSC predictions for different values of σ (from [44]).

energy.

Phenomenologically the resultant form of the spectrum follows

$$I_{\text{sync}} + I_{\text{IC}} = K_{\text{sync}} \left\{ \frac{E}{3.5 \text{ MeV}} \right\}^{\gamma_{\text{sync}}} e^{-E/E_0} + K_{\text{IC}} \left\{ \frac{E}{1000 \text{ MeV}} \right\}^{\gamma_{\text{IC}}} \tag{7}$$

where a 5 parameter fit carried out for Comptel data in combination with data from IACT's produced the result pictured in figure VIII as of 1996. In the context this model the average magnetic field strength may be inferred from the measured flux of TeV photons though $I_{\text{IC}} \propto (\bar{B}E)^{-\delta}$ where $\bar{B} = \bar{B}_{\perp}/0.785$ and E is the γ-ray energy. The measurements of ACT's have given values of the average nebular magnetic field strength in the regime of $(2.6 \pm 0.5) \times 10^{-4}$ G, which are consistent with a value of $\sigma = 0.003$.

The IC spectrum of the crab nebula at high energies has been shown to obey either a power law or a power law with an exponential cutoff at energies between 1

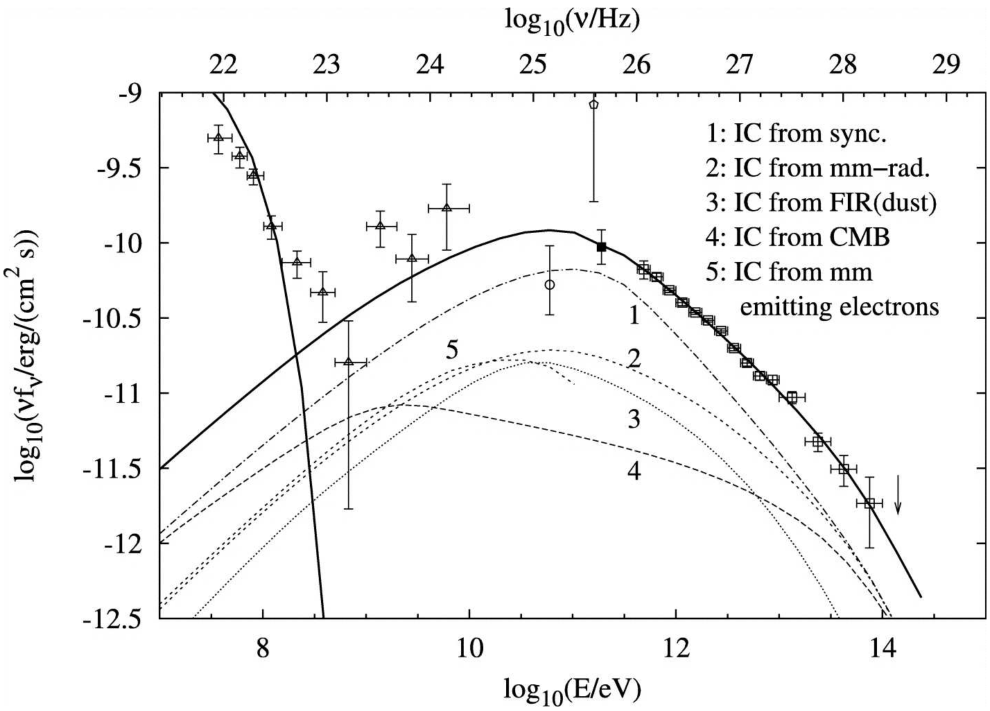

Figure IX: The modified SSC model decomposed into its individual components. At high energies contributions non-synchrotron photons become the dominant seed maintaining the power law up to energies of 100 TeV (from [10]). Superimposed on the model are fluxes measured from HEGRA and EGRET at sub-TeV energies.

and 100 TeV. Measurements carried out by the collaboration HEGRA showed only a slight indication of a cutoff [10] with CANGAROO [109] showing no indication of a cutoff in the IC spectrum above 10 TeV, in contravention to the expectation that such a cutoff would be observed. A probable explanation put forth in [10] is the presence of additional seed photons originating from other sources, such as the infrared background as well as far infrared photons originating from dust in the vicinity of the crab pulsar (see figure IX). Minimization of $\bar{B}$ with the model presented in [10] yielded an optimum value of $(1.616 \pm 0.8) \times 10^{-4}$ G, which is consistent with values obtained with the older model and measurements from [44].

An important question to which we seek answers is: what fraction of ions are accelerated in pulsar wind nebula such as the crab nebula, on the basis that such objects represent a potential source of cosmic rays. A potential alternate mechanism for acceleration of ions does exists in the form of resonant scattering of positrons by cyclotron waves originating from ions located in the downstream region of the pulsar wind, where the resultant particle spectrum has been shown to obey a power law [22]. Such a mechanism would be indistinguishable from the leptonic SSC model with one important exception, the expected cutoff energy due to synchrotron losses for protons is significantly higher, implying the presence of a cutoff would only be detected at energies in excess of 100 TeV. If this is the correct scenario, then young supernova remnants such as the crab nebula could well be important cosmic ray accelerators.

II Active Galactic Nuclei

Active Galactic Nuclei (AGN's) are the second class of TeV γ-ray source discovered, the first of which was Markarian 421 observed by Whipple in the early 1990's (see [97]). Currently AGN's are broadly defined as galactic centers which emit in one or more wavelengths more energy than would otherwise be expected from stellar sources within the vicinity of the Galactic center. More precisely The nucleus of a galaxy is generally classified as active, for the case the one or more of the following criteria are met [111]:

- A high luminosity region located in the core of the galaxy in great contrast with the surrounding regions of the galaxy.
- Jets which may be detected at any wavelength originating from the core of the galaxy.
- Contains a spectrum of non-thermal origin.
- Has a spectrum containing emission lines of non-stellar origin.
- Short term variability on the order of days to years.

Due to the nature of the definition, the term AGN encompasses a wide variety of objects, including BL Lacertae objects, with which we are primarily concerned. In spite of this broad definition the vast majority (95%) of galaxies detected in the universe do not exhibit any of these behaviors. Due to the scope of the definition and plethora of sources contained therein many of these objects have been previously observed and assigned historical classification, and as a result many fall into sub-classifications based upon the idiosyncrasies of their individual spectra.

Although the variety of AGN's is vast it is currently believed the all are powered by the accretion of matter onto a supper-massive black hole, with a mass ranging from 10^7 $M_\odot$ to 10^{10} $M_\odot$ located at the center of galaxies. This type of emissions mechanism was first suggested by Salpeter in 1964 [100] as a potential source of strong emission. This assertion is further supported by the rapid variability of many of these sources across the entire observable spectrum, as the characteristic size of a source may be estimated by $L \propto t$ where L is the length scale of the source and t is the time scale of the variability.

Currently AGN's may be broadly separated into two categories radio-loud and radio-quiet; the majority of which belong to the latter with a space density exceeding that of their loud counterparts by a factor of $\approx$ 10. In spite of the significant difference in the properties of their spectra in the radio range, the spectra at higher energies (infrared though X-ray) show remarkable similarities [114]. One may infer that both of these types of objects share a common emissions engine, where changes in the morphology and matter distribution in the vicinity of the source are likely the cause of the observed discrepancies in the lower energy spectra.

These two categories may be further divided into sub-categories depending upon the presence of emissions lines within their spectra. One such categorization is shown in table I. Here again in the radio-loud regime, there exist the same similarities in spectra outside of the radio range which prompted the introduction of a number of different unification schemes. Expanding upon the idea the current models for AGN's consist of a super-massive black hole with a mass of 10^7-$10^{10} M_\odot$ surrounded by an accretion disk, it becomes clear that the properties observed are highly dependent upon the orientation of the source with respect to the observer,

Observed Properties	Type		Components
	Radio Quiet Version (In Spiral Galaxies)	Radio Loud Version (In Elliptical Galaxies)	
Narrow high excitation forbidden lines, IR-opt-UV-X continuum, Low polarization, Variability	Type 1 Seyfert, QSO	Broad Line Radio Galaxy	central engine, +BLR, +NLR
Narrow high excitation forbidden & permitted lines, Non-stellar continuum, no variability	Type 2 Seyfert	Narrow line radio galaxy	NLR + weak or different hidden engine?
Narrow low excitation lines, no variability	LINER	LINER	NLR
Strong Continuum, no lines or weak lines, high polarization, fast and dramatic variability	Exist?	BL Lac objects or blazars	Unobscured central engine, or jet

Table I: Listing of AGN properties and their respective designations (adapted from [79] or more simply the properties observed while viewing an AGN jet from the side are very different from those observed when the jet is oriented toward the observer [110].

For an AGN, where the jet is not oriented toward the observer the material in the accretion disk, as well as the surrounding galaxy obscures the sources and simultaneously gives rise to line emission. Conversely an AGN with the jet oriented toward the observer will give rise to continuum radiation, characteristic of synchrotron radiation and inverse Compton scattering that is expected to take place within such relativistic outflows of material. In reference to table I the angle between the line of sight and the jet decreases as one moves further down the table. These arguments provide a good basis for unification within the "radio" groups but do not provide a grand unification for these models. A grand unification scheme for these two "radio" groups is however an active area of research with the differences in the host galaxies as the natural focus of this effort. One idea focuses on the possibility that the progenitors of radio-loud AGN's are galaxies which undergo mergers where the central black holes eventually coalesce, leaving an extremely massive rapidly spinning blacking hole at the center of the galaxy [114]. It is this rapidly spinning black hole, from which energy is extracted through the Blandford-Znajek mechanism (see [33]), which gives rise to the radio loud jets. This mechanism can best be described in analogy to the pulsar model, where angular momentum is extracted from the pulsar through electromagnetic interactions via a strong magnetic field. In this case, however, the magnetic field originates from an accretion disk surrounding the black hole. For the galaxies, that have not undergone a merger the available angular momentum within the black hole would remain a factor of two or more smaller resulting in a significantly weaker radio emissions and jets. There do exist other potential explanations for the difference between radio quiet and radio loud AGN's however those are beyond the scope of our discussion.

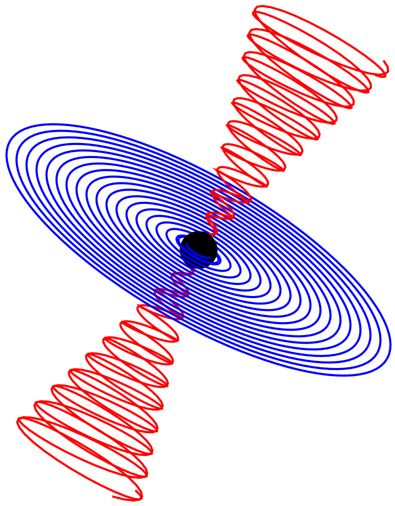

Figure X: Schematic of the Current AGN paradigm. A super-massive black hole is surrounded by an accretion disk (shown in blue) with a relativistic jet of material expelled approximately perpendicular to the plane of the accretion disk. Surrounding the accretion disk is a torus of dust and gas (not pictured).

i Blazars

Markarian 421 and Markarian 501, which are the only confirmed extragalactic objects observed by Milagro, are BL Lacertae objects a subclass of objects known as a blazar. Blazars are characterized by continuum radiation with a high degree of polarization, as well as rapid variability across the entire electromagnetic spectrum. The distinguishing feature of BL Lacertae objects are the complete absence of emissions lines in the optical range. Markarian 421 is the lowest red shift object of this type with $z = 0.030$ and has been found to nearly constantly radiating TeV photons at some level, while Markarian 501 appear to turn on and off for long periods of time.

The jets within the blazars and other AGN's have been determined to have an extremely high bulk Lorentz factors of $\Gamma \simeq 10$. The evidence for this comes in many forms, including the observation of TeV γ-rays which would otherwise interact with the non-relativistic jet material making the emissions region opaque to high energy photons. Blazars with a jet oriented away from the observer's line of sight (radio loud galaxies) also have been observed with radio lobes expanding with superluminal velocities, consistent with the expected observations for relativistic outflows [56] and the general model of AGN's (see figure X). It is important to note that all VHE bright AGN's have been identified as BL Lac objects.

Blazars provide us the unique opportunity to observe the properties of and processes occurring within the jets. In particular the determination of the types of particles accelerated within the jet are chief among the questions to which we seek answers. To that end detailed spectra across the entire EM spectrum have been measured from blazars in their various high and low states. From these measurements it has been determined that blazars obey a wide variety of spectra, however these appear very similar to the spectra expected from the Synchrotron Self Compton (SSC) model described in the previous section for pulsars, having both a peak in the X-rays and γ-rays the locations of which appear to have a strong dependence on the radio luminosity and is correlated via a broken power law given by

$$\nu_{\text{peak, sync}} \propto L_{5\text{ GHz}}^{-\eta} \begin{cases} \eta = 0.6 & \log(L_{5\text{ GHz}}) < 42.5 \\ \eta = 1.8 & \log(L_{5\text{ GHz}}) > 42.5 \end{cases} \tag{8}$$

The ratio of the frequency at which the γ-ray and X-ray peaks occur is assumed to be constant, as is the ratio of the and that the peak radio and γ-ray luminosities (see equations (9) and (10)).

$$\frac{\nu_{\text{peak, }\gamma}}{\nu_{\text{peak, sync}}} \simeq 5 \times 10^{8} \tag{9}$$

$$\frac{\nu_{\gamma} L_{\text{peak, }\gamma}}{\nu_{5\text{ GHz}} L_{5\text{ GHz}}} \simeq 3 \times 10^{3} \tag{10}$$

These results fit well to the observed spectra in both states and show that blazars and flat spectrum radio quasars obey a limited continuum of possible spectra [54]. An updated analysis modified this picture somewhat in order to match additional data gathered from a larger sample of AGN's as well as the inclusion of harder X-

Ray spectra. Discrepancies in the new data set were corrected by setting the ratio of the luminosities for the radio and γ-ray peaks to one for $L_{5\ \mathrm{GHz}} < 10^{43}$ erg s^{-1}, and by changing the indices in equation (8) to $\eta_{L<42.5} = 0.4$ and $\eta_{L>42.5} = 1.2$. For luminosities $L_{5\ \mathrm{GHz}} < 10^{43}$ erg s^{-1} the synchrotron and γ-ray peaks are taken to have identical luminosities [47]. It is important to note that many observations upon which this model is firmly based were not carried out simultaneously and a certain amount of caution must be taken. The general interpretation of this empirical model is that the regularity of the spectra must be the result of an underlying physical process. For a deeper understanding however one must look to other models.

ii Leptonic vs. Hadronic acceleration Models

Since the discovery of TeV emission from blazars, there have been a wide variety of emissions models proposed. The first general category, are based on a synchrotron self Compton model, quite similar to that of pulsar wind nebula and a natural starting point considering the similarities between the observed spectra for these objects. Many models with various assumptions about the morphology of the emissions region, distribution of shocks within the jets, among many other factors have been considered. In general the SSC model is nearly identical to that of the pulsar wind nebulae, excepting that the configuration of the emissions region is different, here electron-positions undergo synchrotron losses due to the local magnetic field, the photon then interacts vi IC scattering gaining energy (see for example [86]). One picture considers a number of temporary shocks within the jet occurring occurring sporadically. One the shock forms electrons are accelerated giving enhanced photon flux at X-Ray and TeV energies, consistent with the high degree of correlation observed between X-Ray and γ-ray flares.

The other class of model are those involving the acceleration of hadrons and other heavy ions within the jets, each predicting the emission of TeV photons through directly accelerated protons, and others thorough proton induced cascades within the jets themselves where $p + \gamma \rightarrow \pi + X$ (see for example [85]). The requirement for this type of model is that the bulk of the jet's energy in the form of relativistic protons, where interactions with surrounding gas provide a population of electrons-positrons via $\pi^{\pm,0}$ decay that mimic the SSC spectrum. The primary difference in the observed spectral features are predicted to occur at TeV energies, where again a cutoff energy is expected above that for the standard SSC models Should proton acceleration take place within AGN's jets, it is predicted that acceleration of protons to energies in excess of 10^{20} eV would be possible making these an ideal candidate for the origin of the ultra high energy cosmic rays, and for some of the potential point sources [63] and anisotropy observed above 10^{18} eV [62] by the AGASA collaboration.

Both of these models exhibit similar spectra, making their differentiation difficult however the spectra predicted by hadronic models extends to energies of up to 20 TeV where leptonic models exhibit cutoffs in the low TeV to sub-GeV energy ranges. Differentiation of spectra is however made more difficult due to gamma ray attenuation that is expected to occur in the presence of the extragalactic background light. Though some direct measurements have been preformed [32] the spectrum of the EBL is largely unknown and may quite possibly reduce the observed γ-ray flux at high energies, creating artificial cutoffs.

Chapter VI

Results of the Milagro Spectral Measurements

Using the technique outlined in the previous chapter, the measurement of spectra for diffuse and point sources has been possible. The requirement that outriggers be utilized for the reconstruction of core positions for the reconstruction of spectra is most restrictive and limits the number of sources that may be analyzed with these routines. The sources for which spectral measurements have been preformed are, Crab pulsar wind nebula, the active galactic nucleus Markarian 421, an unidentified extended source located in the Cygnus region of our Galaxy, and diffuse emission from the Cygnus region. There exist additional sources that have been detected with high confidence which are not reported here. The following is an outline of the results and physical consequences.

I Galactic Sources

The majority of sources observed with Milagro are galactic sources, which reside in the galactic plane (see the Milagro source catalog). Of these sources those for which a spectral determination are the Crab nebula, the cygnus region hot spot (MGRO J2019+37) and the diffuse TeV emission originating from the cygnus region of the

Milky Way.

i The Crab Nebula

Following the procedure outlined in the chapter on spectral determination and energy estimation, fits to two spectral forms have been carried out for the crab nebula

$$j(E) = I_0 \left\{ \frac{E}{10\ \text{TeV}} \right\}^{\gamma} \tag{1}$$

$$j_c(E) = I_0 \left\{ \frac{E}{10\ \text{TeV}} \right\}^{\gamma} e^{-E/E_c} \tag{2}$$

a power law (1) and a power law with an exponential cutoff (2). The normalization of the power law to 10 TeV is implemented in place of the usual value 1 TeV utilized by other groups, in order to reduce the correlation of the fit parameters.

The fit to a simple power law yields

$$\gamma = -3.11$$

$$I_0 = 5.88 \times 10^{-10}\ \text{TeV}^{-1}\text{s}^{-1}\text{m}^{-2}$$

$$\chi^2(\text{dof}) = 4.8427(6)$$

for the central fit values with the error contour for this fit given in figure Ib. Included in figure Ia are the calculated fluxes and fit spectrum with the results of IACT's plotted for comparison. The power law fit from Milagro is consistent with the results of the IACT's above 5 TeV. The fit to a power law with an exponential cutoff yields a $\chi^2(\text{dof}) = 2.92(5)$. Application of an F-test shows that the Milagro data by itself neither requires nor rules out the presence of a cutoff above 10 TeV.

The results for the Crab nebula are consistent with both leptonic and hadronic acceleration models within the Crab plerion, as the main distinguishing feature between these effects would be the presence of an exponential cutoff in the inverse Compton spectrum below 50 TeV. Recent results from the HESS [11] collaboration fit a cutoff at $14.3 \pm 2.1_{\text{stat}}$ TeV, however previous results from the Cangaroo [109]

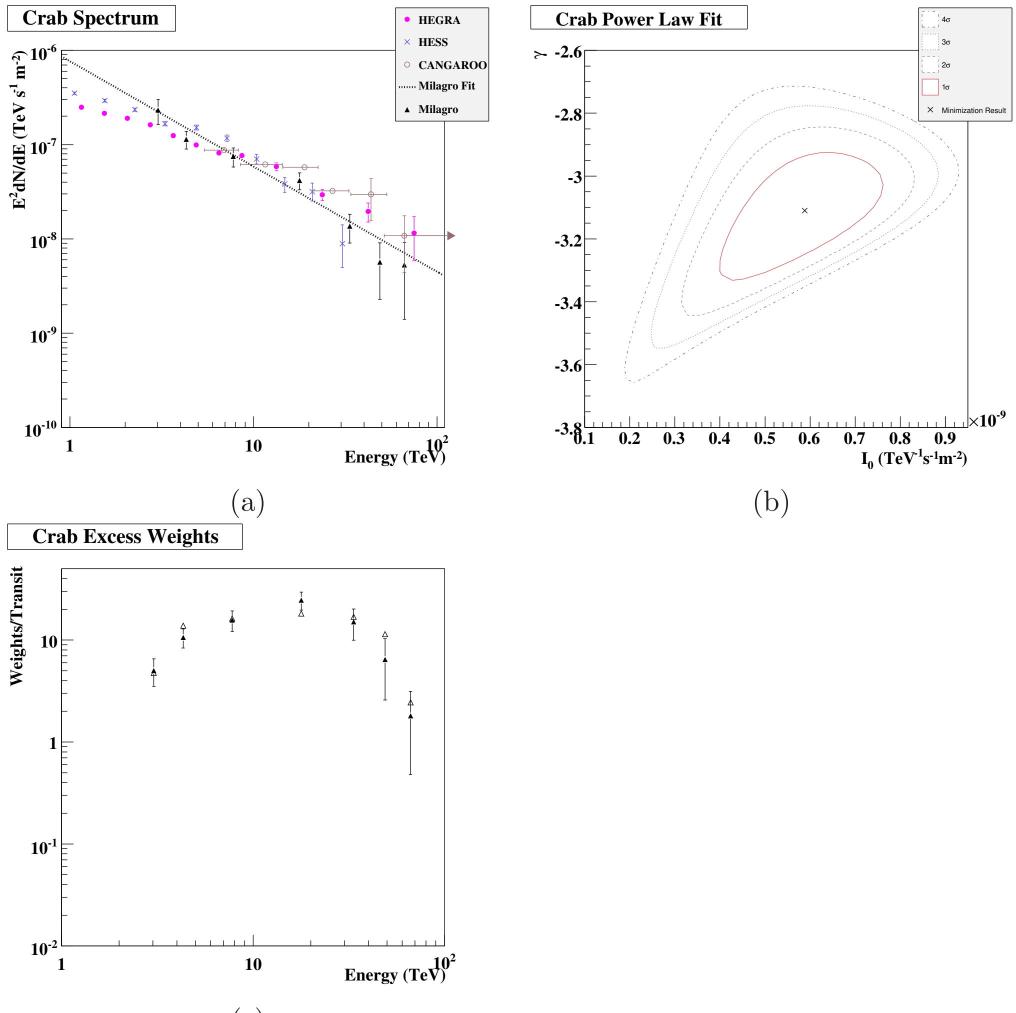

(a) (b) (c)

Figure I: (a) Milagro Power law fit to the Crab spectrum from 1 to 100 TeV, compared with the results of other experiments and (b) the associated fit error contour. (c) Also included are the measured excess weights (solid triangles) used in the computation of this fit, with the expected excess weights determined for the optimum spectrum.

and HEGRA [10] experiments have shown little or no indication for such a cutoff. Due to the large systematic error ($\approx 20\%$) associated with all of these experiments the results remain consistent and are unable to definitively rule out either model, or a combination of both. Definitive confirmation of either model will likely only be solved with the detection of a neutrino signal by ICECUBE due to $p\gamma \rightarrow \pi \rightarrow \nu l$ interactions within the crab nebula (implying the acceleration of a large number of hadrons) or the lack thereof (confirming the absence of accelerated hadrons) or substantial improvement in the systematics of ground based γ-ray detection methods.

ii MGRO J2019+37 (Cygnus Region Hot Spot)

MGRO J2019+37 is the second most luminous source detected by the Milagro detector, and is located at a declination of $36.83 \pm 0.08_{\text{stat}} \pm 0.25_{\text{sys}}$ and a right ascension of $304.83 \pm 0.14_{\text{stat}} \pm 0.3_{\text{sys}}$.

As this source has been shown to be slightly extended, the spectrum in not measured using the optimal bin size of $1.1°$. Instead a square bin size of $3° \times 3°$ (see figure II has been used for the standard determination of excess events. Aside from this modification the fit procedure is identical to that of the other sources.

As before a fit to a simple power law has been preformed yielding

$$\gamma = -2.69$$

$$I_0 = 2.5 \times 10^{-10}\ \text{TeV}^{-1}\text{s}^{-1}\text{m}^{-2}$$

$$\chi^2(\text{dof}) = 7.7(5)$$

Once again a fit to an exponential cutoff yields a $\chi^2(\text{dof}) = 4.77(4)$ value insufficient for the confirmation or exclusion of a power law fit.

The power law fit for this hot spot is flatter than that of the diffuse source (discussed in the next section) however it cannot be ruled out that the spectra are different for one another due to the large statistical uncertainty in the measurement of the diffuse γ-ray spectrum

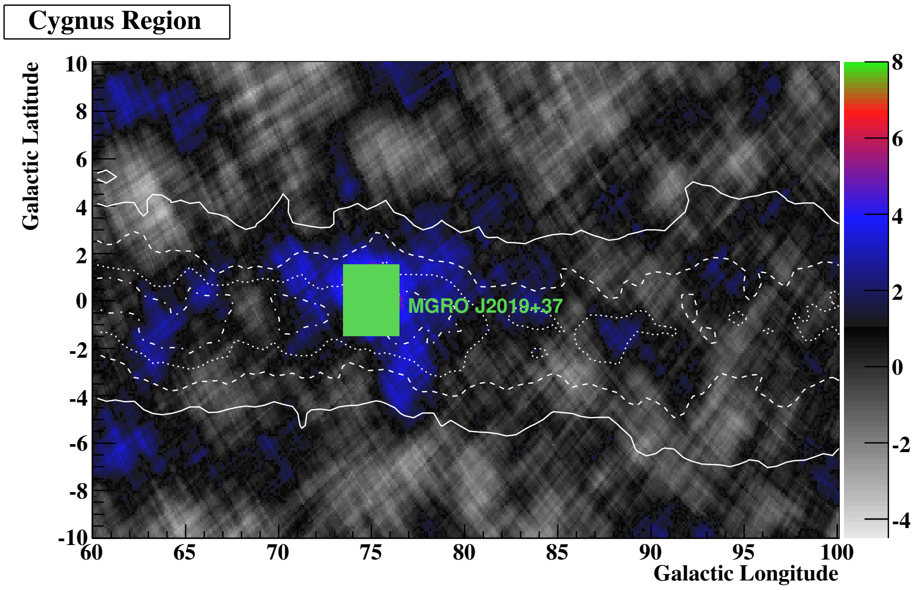

Figure II: The 3° × 3° bin defined as MGRO J2019+37 in this analysis. Included are the contours for the measured column density of HI from the LAB survey [72].

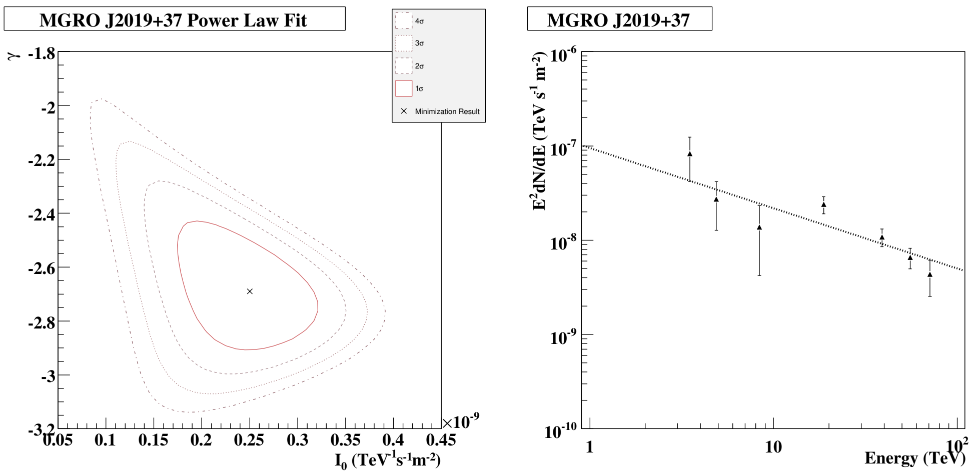

(a) (b)

Figure III: (a) The error contour (b) and fit spectrum for the power law fit to MGRO J2019+37.

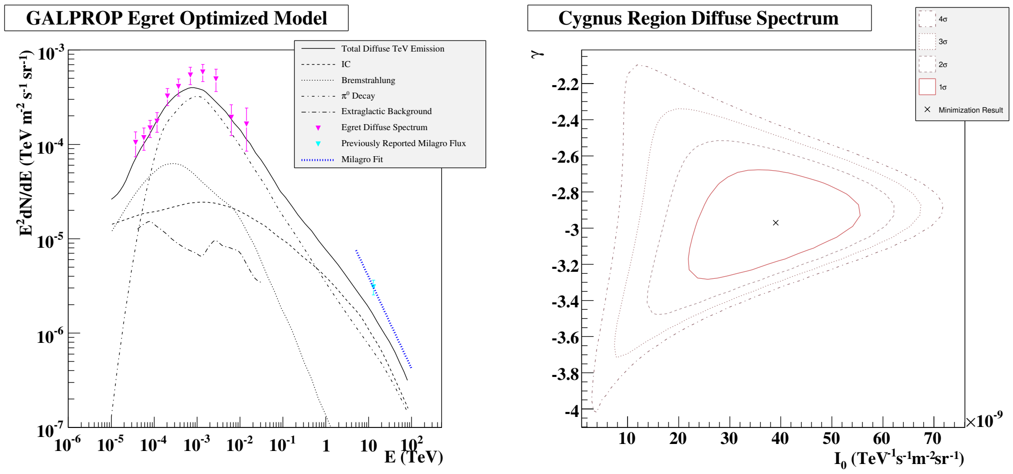

(a) (b)

Figure IV: (a) The power law fit to the diffuse emission from the cygnus region with the theoretical spectrum from GALPROP and the fluxes as measured with EGRET [8]. In (b) error contour for the fit is provided.

iii Diffuse Emission from the Cygnus Region

One of the exciting prospects for an all sky instrument such as Milagro is the study of Diffuse sources. Milagro is the first instrument to detect diffuse TeV emission outside of the galactic center region, providing the opportunity to study cosmic ray interactions.

Within the Cygnus region one extended point source has been discovered, labeled MGRO J2019+37, which is excluded from the fit by removing the $3^\circ \times 3^\circ$ bin used for the measurement of its spectrum (see previous section). The remainder of the Cygnus region defined in galactic coordinates as $-2^\circ \leq e \leq 2^\circ$ and $65^\circ \leq l \leq 85^\circ$ where a background estimate is preformed as usual.

Because the source extends over a wide range of declinations an average value for the on-source, off-souce exposure ($\langle\alpha\rangle$) ration is used in the significance computation. This approximation is valid as the value of α changes by no more than 1% over the entire declination range of the extended source.

The observed TeV spectrum in this region fits well with a power law with parameters

$$\gamma = -2.97$$

$$I_0 = 3.9 \times 10^{-8}\ \mathrm{TeV}^{-1}\mathrm{s}^{-2}\mathrm{m}^{-2}\mathrm{sr}^{-1}$$

The GALPROP model, with which our results here are compared, is a numerical simulation of cosmic ray interaction and propagation which uses the local column density of measured gas to predict diffuse γ-ray flux through cosmic ray interactions (see [8] and references therein for details). The theoretical γ-ray spectrum for the Cygnus region is based upon the assumption that the cosmic ray composition and spectrum in the Cygnus region agree with local measurements.

The Model agrees with our measured spectrum for the region, though it should be noted that the statistical error for this measurement is very large (see figure IVb).

During the course of its observations only 2 extragalactic sources have been observed by Milagro and its precursor Milagrito: Markarian 421 and Markarian 501, both of which are active galactic nuclei at redshifts lower than 0.05. For the available data set a spectrum has been reconstructed for Markarian 421.

II Extragalactic Source

i Markarian 421

As with the Crab Nebula measurement a fit to an power law and power law with an exponential cutoff have been preformed, using a bin size of 1.1° as with the crab nebula. The fit to the power law gives yields

$$\gamma = -3.35$$

$$I_0 = 1.7 \times 10^{-10}\ \mathrm{TeV}^{-1}\mathrm{s}^{-1}\mathrm{m}^{-2}$$

$$\chi^2(\mathrm{dof}) = 7.62(4)$$

where the error contours for this fit are found in figure V. Here again a fit to an power law with an exponential cutoff was preformed with a $\chi^2(\text{dof}) = 2.62(4)$. Once again it has been determined that the Milagro result can neither exclude nor confirm the existance of a cutoff within this spectrum. No measurable signal was observed above an energy of approximately 20 TeV strongly indicating the presence of a cutoff.

The Milagro fit to the spectrum agrees well with previous measurements carried out using ACT's, however a direct comparison of any measurement must be considered carefully as the measurements were not preformed simultaneously and the source is known to be highly variable across the entire EM spectrum. This aside the general behavior of the spectrum and the lack of a definitive signal above 20 TeV are expected for this object in the context of leptonic models, although a cutoff may also be present for hadronic models. Unfortunately this is not a definitive indicator of the composition of the accelerated particles due to the possible effect of extragalactic background light absorption which is expected to make the universe outside our galaxy opaque to γ rays with energies in excess of approximately 10 TeV.

As with the Crab nebula definitive confirmation of either acceleration model must wait for confirmation from ν telescopes currently under construction, or in the planning stages.

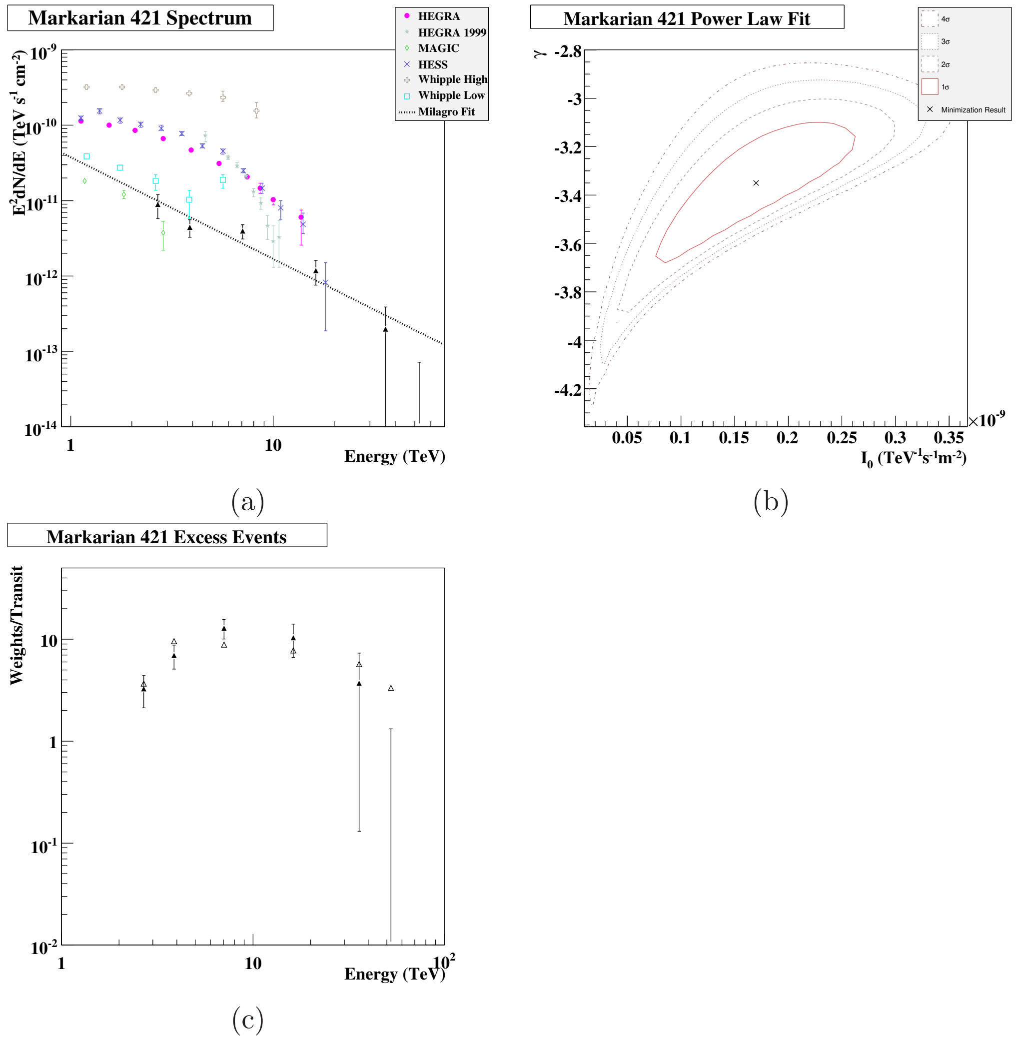

Figure V: (a) Milagro Power law fit to the Markarian 421 spectrum from 1 to 20 TeV, compared with the results of other experiments (from [14]) and (b) the associated fit error contour. Shown in (c) are the excess weights measured from Mrk 421 as a function of energy (solid triangles), and excess weights expected from the fit spectrum (open triangles).

Chapter VII

Concluding Remarks

The measurement of TeV γ-ray spectra for the various sources observed by Milagro have proven to be consistent with observations made with IACT's for the Crab Nebula as well as Mrk 421. The exclusion or confirmation of hadronic or leptonic acceleration within these sources cannot be definitively determined with the Milagro results, or that of the IACT's, and we look to the upcoming results from new km^2 neutrino detectors, ICECUBE in particular, for these answers.

Measurements of the spectra for the cygnus region and cygnus region hot spot (MGRO J2019+37) have also been carried out. The fit to the diffuse spectrum is consistent with the results of cosmic ray propagation models though the statistical significance of the measurement is too low to rule out the possibility of additional point sources within the region.

The introduction of this technique has shown spectral measurement using a water Cherenkov array is possible and that a next generation instrument such as HAWC (High Altitude Water Cherenkov Telescope) which is currently being proposed, will have the capability of measuring spectra independent of the measurements carried out by competing experiments.

Bibliography

[1] Archival Data from Goddard Space Flight Center. *HEASARC website*. http://heasarc.gsfc.nasa.gov.

[2] COS-B Factsheet. *ESA Website*. http://sci.esa.int/science-e/www/object/index.cfm?fobjectid=31449.

[3] HESS Source Catalog. *HESS Collaboration Website*. http://www.mpi-hd.mpg.de/hfm/HESS/public/HESS_catalog.htm.

[4] ICRR Tibet AS Gamma Experiment Website. http://www.icrr.u-tokyo.ac.jp/em/index-j.html.

[5] The Third EGRET Catalog of High-Energy Gamma-Ray Sources. *Astrophys. J. Suppl.*, 123:79, 1999.

[6] A. A. Abdo et al. TeV Gamma-Ray Sources from a Survey of the Galactic Plane with Milagro. 705, 2007. 0705.0707.

[7] A.A. Abdo. A_4, Milagro's New γ-Hadron Separation Variable and Spectral Index Estimator. 2006. Internal Memo.

[8] A.A. Abdo et al. Discovery of TeV Gamma-Ray Emission from the Cygnus Region of the Galaxy. *Astrophys. Letters*, 2007:L33–L36, 2007.

[9] F. Aharonian et al. Calibration of Cameras of the HESS detector. *Astroparticle Physics*, 22:109, 2004.

[10] F. Aharonian et al. The Crab Nebula and Pulsar Between 500 GeV and 80 TeV: Observations with the HEGRA Stereoscopic Air Cherenkov Telescopes. *Astrophys. J.*, 614:897–913, 2004.

[11] F. Aharonian et al. Observations of the Crab nebula with HESS (astro-ph/0607333). *Astrophys. J.*, 2006. To appear in ApJ.

[12] H. Aharonian et al. Discovery of very-high-energy γ-rays from the Galactic Centre Ridge. *Nature*, 439:695–698, February 2006.

[13] H. Aharonian et al. The H.E.S.S. Survey of the Inner Galaxy in Very High Energy Gamma Rays. *Astrophys. J.*, 636:777, 2006.

[14] J. Albert. Observations of Mkn 421 with the MAGIC Telescope. *ArXiv Astrophysics e-prints*, 2006. astro-ph/0603478.

[15] D. E. Alexandreas. Point source search techniques in ultra high energy gamma ray astronomy. *Nuclear Instruments and Methods*, 328:570, 1993.

[16] M. Amenomori et al. Search for Steady Emission of 10 TeV Gamma Rays from the Crab Nebula, Cygnus X-3, and Hercules X-1 using the Tibet Air Shower Array. *Phys. Rev.*, 69:2468, 1992.

[17] M. Amenomori et al. Observation of Multi-TeV Gamma Rays from the Crab Nebula using the Tibet Air Shower Array. *Astrophys. J.*, 525:L93, 1999.

[18] M. Amenomori et al. Detection of TeV Gamma Rays from Mrk 501 at High Flaring State of Activity in 1997 with the Tibet Air Shower Array. In B.L. Dingus, M.H. Salamon, and D.B. Kieda, editors, *American Institute of Physics Conference Series*, page 139, 2000.

[19] M. Amenomori et al. Performance of the Tibet-III Air-Shower Array. In *International Cosmic Ray Conference*, page 573, 2001.

[20] M. Amenomori et al. A Northern Sky Survey for Steady Tera-Electron Volt Gamma-Ray Point Sources Using the Tibet Air Shower Array. *Astrophys. J.*, 633:1005, 2005.

[21] Carl D. Anderson. The Positive Electron. *Phys. Rev.*, 43(6):491, March 1933.

[22] J. Arons. Relativistic Shocks and the Excitation of the Crab Nebula. In A. S. Fruchter, M. Tavani, and D. C. Backer, editors, *Millisecond Pulsars. A Decade of Surprise*, volume 72 of *Astronomical Society of the Pacific Conference Series*, page 257, 1995.

[23] K. Asakimori et al. Cosmic-Ray Proton and Helium Spectra: Results from the JACEE Experiment. *Astrophys. J.*, 502:278–283, 1998.

[24] R. Atkins et al. TeV Observations of Markarian 501 with the Milagrito Water Cerenkov Detector. *Astrophys. J.*, 525:L25, 1999.

[25] R. Atkins et al. Evidence for TeV Emission from GRB 970417A. *Astrophys. J. Lett.*, 533:L119, 2000.

[26] R.W. Atkins et al. Observation of TeV gamma rays from the Crab nebula with Milagro using a new background rejection technique. *Astrophys. J.*, 595:803, 2003.

[27] R.W. Atkins et al. TeV gamma-ray survey of the northern hemisphere sky using the Milagro observatory. *Astrophys. J.*, 608:680, 2004.

[28] R.W. Atkins et al. Evidence for TeV gamma-ray emission from the galactic plane. *Physical Review Letters*, 95:251103, 2005.

[29] W. Baade. The Crab Nebula. *Astrophys. J.*, 96:188, 1942.

[30] W. Baade and F. Zwicky. Supernovae and Cosmic Rays. *Phys. Rev.*, 45:138, 1934.

[31] D. Berley et al. Status of the Expansion of the CYGNUS Array at Los Alamos. In *International Cosmic Ray Conference*, page 301, 1990.

[32] R.A. Bernstein et al. The First Detections of the Extragalactic Background Light at 3000, 5500, and 8000 Å. I. Results. *Astrophys. J.*, 571:56, 2002.

[33] R. D. Blandford and R. L. Znajek. Electromagnetic extraction of energy from Kerr black holes. *Mon. Not. Roy. Astron. Soc.*, 179:433, 1977.

[34] E. Blaufuss. VME Trigger Card Manual. 2002. Internal Memo.

[35] E. Blaufuss. Milagro DAQ Help Page. 2004. Internal Memo.

[36] J. M. Blondin, R. A. Chevalier, and D. M. Frierson. Pulsar Wind Nebulae in Evolved Supernova Remnants. *Astrophys. J.*, 563:806, 2001.

[37] J. G. Bolton and G. J. Stanley. The Position and Probable Identification of the Source of the Galactic Radio-Frequency Radiation Taurus-A. *Australian Journal of Scientific Research A Physical Sciences*, 2:139, 1949.

[38] F. Camilo, V. M. Kaspi, A. G. Lyne, R. N. Manchester, J. F. Bell, N. D'Amico, N. P. F. McKay, and F. Crawford. Discovery of Two High Magnetic Field Radio Pulsars. *Astrophys. J.*, 541:367, 2000.

[39] M. L. Cherry, E. L. Chupp, P. P. Dunphy, D. J. Forrest, and J. M. Ryan. Statistical Evaluation of Gamma-Ray Line Observations. *Astrophys. J.*, 242:1257, 1980.

[40] W. J. Cocke, M. J. Disney, and Taylor D. J. Discovery of Optical Signals from Pulsar NP 0532. *Nature*, 221:525, 1969.

[41] D. Coyne and M. Schneider. First Results on Milagro Water Attenuation Using Measurements from the Upgraded TUBE. *Internal Memo*, 8 2002.

[42] A. Daum et al. First results on the performance of the HEGRA IACT array. *Astroparticle Physics*, 8:1, 1997.

[43] O. C. De Jager and A. K. Harding. The expected high-energy to ultra-high-energy gamma-ray spectrum of the Crab Nebula. *Astrophys. J.*, page 161, 1992.

[44] O.C. De Jager et al. Gamma-Ray Observations of the Crab Nebula: A Study of the Synchro-Compton Spectrum. *Astrophys. J.*, 457:253D–266D, January 1996.

[45] V.A. Debrina et al. Cosmic-Ray Spectra and Composition in the Energy Range of 10-1000 TeV per Particle Obtained by the RUNJOB Experiment. *Astrophys. J.*, 628:L41–L44, 2005.

[46] Tyce DeYoung. Simple Corefitting with Outriggers. 2003. Internal Memo.

[47] D. Donato, G. Ghisellini, G. Tagliaferri, and G. Fossati. Hard X-ray properties of blazars. *Astronomy and Astrophysics*, 275:739, 2001.

[48] Duyvendak, J. J. L. Further Data Bearing on the Identification of the Crab Nebula with the Supernova of 1054 A.D. Part I. The Ancient Oriental Chronicles. *"Publications of the Astronomical Society of the Pacific"*, 54:91, 1942.

[49] M. Errando et al. Observation of Extragalactic Sources of Very High Energy γ-rays with the MAGIC Telescope. *ArXiv Astrophysics e-prints*, 2007. astro-ph/0701202.

[50] J.A. Esposito et al. In-Flight Calibration of EGRET on the Compton Gamma-Ray Observatory. *Astrophys. J.*, 123:203, 1999.

[51] G.G. Fazio et al. Detection of High-Energy Gamma Rays from the Crab Nebula. *Astrophys. J.*, 175:L117, 1972.

[52] E. Fermi. On the Origin of the Cosmic Radiation. *Phys. Rev.*, 75:1169, 1949.

[53] R. A. Fesen and R. P. Kirshner. The Crab Nebula. I - Spectrophotometry of the filaments. *Astrophys. J.*, 258:1, 1982.

[54] M. G. Fossati et al. A unifying view of the spectral energy distributions of blazars. *Mon. Not. Roy. Astron. Soc.*, 299:433, 1998.

[55] B. M. Gaensler and P. O. Slane. The Evolution and Structure of Pulsar Wind Nebula. *Annual Review of Astronomy and Astrophysics*, 44(1):17, 2006.

[56] P. G. Ghisellini, P. Padovani, A. Celotti, and L. Maraschi. Relativistic bulk motion in active galactic nuclei. *Astrophys. J.*, 407:65, 1993.

[57] T. Gold. Rotating Neutron Stars as Origin of Pulsating Radio Sources. *Nature*, 218:731, 1968.

[58] P. Goldreich and W. H. Julian. Pulsar Electrodynamics. *Astrophys. J.*, 157:869, 1969.

[59] K. Greisen. End to the Cosmic-Ray Spectrum? *Physical Review Letters*, 16(17):748, 1966.

[60] J. E. Gunn and J. P. Ostriker. Magnetic Dipole Radiation from Pulsars. *Nature*, 221:454.

[61] R.C. Hartman et al. Galactic Plane Gamma-radiation. *Astrophys. J.*, 230:597, 6 1979.

[62] Hayashida et al. The anisotropy of cosmic ray arrival directions above 10^{18} eV. *Astroparticle Physics*, 10:303, 1999.

[63] N. Hayashida et al. Possible clustering of the most energetic cosmic rays within a limited space angle observed by the Akeno Giant Shower Array. *Phys. Rev.*, 77:1000, 1996.

[64] D. Heck et al. Report FZKA 6019. *Forschungszentrum Karlsruhe.* http://www-ik.fzk.de/corsika/physics-description/corsika_phys.html.

[65] W. Heitler. *Quantum theory of radiation.* International Series of Monographs on Physics, Oxford: Clarendon, 1954, 3rd ed., 1954.

[66] J. J Hester et al. WFPC2 Studies of the Crab Nebula. I. HST and ROSAT Imaging of the Synchrotron Nebula. *Astrophys. J.*, 448:240, 1995.

[67] A. Hewish et al. Observation of a rapidly pulsating radio source. *Nature*, 217:709, 1968.

[68] A. Hewish et al. Observations of some further Pulsed Radio Sources. *Nature*, 218:126, 1968.

[69] A.M. Hillas. Cherenkov light images of EAS produced by primary gamma. In F.C. Jones, editor, *International Cosmic Ray Conference*, page 445, 1985.

[70] J. Holder et al. The first VERITAS telescope. *Astroparticle Physics*, 25:391–401, 2006.

[71] H. Hu et al. A Northern Sky Survey for both TeV Cosmic-Ray Anisotropy and TeV γ-ray Sources using the Tibet Air Shower Array. *Nuclear Physics B Proceedings Supplements*, 151:121, 2006.

[72] Kalberla et al. The Leiden/Argentine/Bonn (LAB) Survey of Galactic HI. Final data release of the combined LDS and IAR surveys with improved stray-radiation corrections. *Astronomy and Astrophysics*, 440:775, 2005.

[73] G. Kanbach et al. The project EGRET (Energetic Gamma-Ray Experiment Telescope) on NASA's Gamma-Ray Observatory (GRO). *Space Science Reviews*, 49:69, 1988.

[74] C. F. Kennel and F. V. Coroniti. Confinement of the Crab pulsar's Wind by its Supernova Remnant. *Astrophys. J.*, 283:694, 1984.

[75] C. F. Kennel and F. V. Coroniti. Magnetohydrodynamic model of the Crab nebula radiation. *Astrophys. J.*, 283:710, 1984.

[76] Ray W. Klebesadel et al. Observations of Gamma-Ray Bursts of Cosmic Origin. *Astrophys. J.*, 182:L85, 1973.

[77] W. Kraushaar et al. Explorer XI Experiment on Cosmic Gamma Rays. *Astrophys. J.*, 141(3):845, 1965.

[78] C.M.G. Lattes et al. Processses Involving Charged Mesons. *Nature*, 159:694, 1947.

[79] A. Lawrence. Classification of active galaxies and the prospect of a unified phenomenology. 99:309, 1987.

[80] T. P. Li and Y. Q. Ma. Analysis Methods for Results in Gamma-ray Astronomy. *Astrophys. J.*, 272:317, 1983.

[81] E. Lorenz. Status of the 17 m MAGIC Telescope. *New Astronomy Review*, 48:339, 2004.

[82] R. Lynds, S. P. Maran, and D. E. Trumbo. Optical Identification and Observations of the Pulsar NP 0532. *Astrophys. J. Lett.*, 155:L121, 1969.

[83] A. G. Lyne, R. S. Pritchard, F. Graham-Smith, and F. Camilo. Very low braking index for the Vela pulsar. *Nature*, 381:497, 1996.

[84] R. N. Manchester, G. B. Hobbs, A. Teoh, and M. Hobbs. The ATNF Pulsar Catalogue. *The Astronomical Journal*, 129:1993, 2005.

[85] K Mannheim. The Proton Blazar. *Astronomy and Astrophysics*, 269:67, 1993.

[86] L. Maraschi. A Jet Model for the gamma ray emitting blazar 3C 279. *Astrophys. J.*, 397:5, 1992.

[87] N. U. Mayall and J. H. Oort. Further Data Bearing on the Identification of the Crab Nebula with the Supernova of 1054 A.D. Part II. The Astronomical Aspects. *"Publications of the Astronomical Society of the Pacific"*, 54:95, 1942.

[88] P.F. Michelson. Instrumentation for the Gamma-ray Large Area Space Telescope (GLAST) mission. In J.E. Truemper and H.D. Tananbaum, editors, *X-Ray and Gamma-Ray Telescopes and Instruments for Astronomy*, page 1144, March 2003.

[89] R.A. Millikan. Award of the Nobel Prize in Physics to Victor F. Hess and Carl D. Anderson. *The Scientific Monthly*, 44:94, 1937.

[90] R. Minkowski. The Crab Nebula. *Astrophys. J.*, 96:199, 1942.

[91] M. Mori et al. Cangaroo-II and Cangaroo-III. *ArXiv Astrophysics e-prints*, 2001. astro-ph/0106347.

[92] NASA/ESA, The Hubble Key Project Team, and The High-Z Supernova Search Team. 1994.

[93] Seth H. Neddermeyer and Carl D. Anderson. Note on the nature of cosmic-ray particles. *Phys. Rev.*, 51:884, 1937.

[94] K. Nishijima et al. Status of the CANGAROO-III Project. In *International Cosmic Ray Conference*, page 327, 2005.

[95] F. Pacini. Energy Emission from a Neutron Star. *Nature*, 216:567, 1967.

[96] F. Pacini. Rotating Neutron Stars, Pulsars, and Supernova Remnants. *Nature*, 219:145, 1968.

[97] M. Punch et al. Detection of TeV Photons from the Active Galaxy Markarian 421.

[98] M. J. Rees and J. E. Gunn. The Origin of the Magnetic Field and Relativistic Particles in the Crab Nebula. *Mon. Not. Roy. Astron. Soc.*, 167:1–12, 1974.

[99] B. Rossi and Greisen K. Cosmic-ray theory. *Review of Modern Physics*, 13:241, 1941.

[100] E. E. Salpeter. Accretion of Interstellar Matter by Massive Objects. *Astrophys. J.*, 140:796, 1964.

[101] M. Schneider. 3 2004. Collaboration meeting presentation on pond water quality presented at LANL.

[102] I. S. Shklovskii. On the Nature of Optical Emission from the Crab Nebula. *Soviet Astronomy*, 1:690, 1957.

[103] A. J. Smith. Private communication.

[104] R. Sreekumar et al. EGRET Observations of the Extragalactic Gamma-Ray Emmision. *Astrophys. J.*, 494:523.

[105] D. H. Staelin and E. C. Reifstein. Pulsating radio sources near the Crab Nebula. *Science*, 162:1481, 1968.

[106] P. A. Sturrock. A Model of Pulsars. *Astrophys. J.*, 164:529, 1971.

[107] W. T. Sullivan, III. *Classics in Radio Astronomy.* 1982.

[108] B.N. Swanenburg et al. Second COS B Catalog of High-Energy Gamma-Ray Sources. *Astrophys. J.*, 243:L69–L73, 1 1981.

[109] T. Tanomori et al. Detection of Gamma Rays of Up to 50 TeV From the Crab Nebula. *Astrophys. J.*, 492:L33–L36, 1998.

[110] M. C. Urry and P. Padovani. Unified Schemes for Radio-Loud Active Galactic Nuclei. *Publications of the Astronomical Society of the Pacific*, 107:803, 1995.

[111] H. H. Voigt. *Abriss der Astronomie.* Biographisisches Institut and F.A. Brockhaus AG, 5 edition, 1991.

[112] T.C. Weekes et al. A Search for Discrete Sources of Cosmic Gamma Rays of Energy 10^{11}-10^{12} eV. *Astrophys. J.*, 174:165, 1972.

[113] T.C. Weekes et al. Observation of TeV Gamma Rays from the Crab Nebula Using the Atmospheric Cherenkov Imaging Technique. *Astrophys. J.*, 342:379, 1989.

[114] A. S. Wilson and E. J. M. Colbert. The Differences between radio-loud and radio-quiet active galaxies. *Astrophys. J.*, 438:62, 1995.

[115] Fu-Yuan Zhao et al. The Guest Star of AD185 must have been a Supernova. *Chin. J. Astron. Astrophys*, 6(5):635, 2006.